# Organized Layer Overturning in Mesoscale Convective Systems over the Western Pacific Warm Pool

David B. Mechem

A dissertation submitted in partial fulfillment of the
requirements for the degree of

Doctor of Philosophy

University of Washington

2003

Program Authorized to Offer Degree: Department of Atmospheric Sciences

ProQuest Information and Learning Company
300 North Zeeb Road
P.O. Box 1346
Ann Arbor, MI 48106-1346

In presenting this dissertation in partial fulfillment of the requirements for the Doctoral degree at the University of Washington, I agree that the Library shall make its copies freely available for inspection. I further agree that extensive copying of the dissertation is allowable only for scholarly purposes, consistent with "fair use" as prescribed in the U. S. Copyright Law. Requests for copying or reproduction of this dissertation may be referred to Bell and Howell Information and Learning, 300 North Zeeb Road, Ann Arbor, MI 48106-1346, to whom the author has granted "the right to reproduce and sell (a) copies of the manuscript in microform and/or (b) printed copies of the manuscript made from microform."

Signature 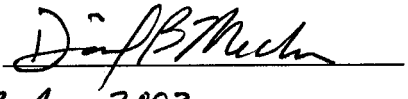

Date 7 Aug 2003

University of Washington
Graduate School

This is to certify that I have examined this copy of a doctoral dissertation by

David B. Mechem

and have found that it is complete and satisfactory in all respects,
and that any and all revisions required by the final
examining committee have been made.

Co-Chairs of Supervisory Committee:

Robert A. Houze, Jr.

Shuyi S. Chen

Reading Committee:

Robert A. Houze, Jr.

Shuyi S. Chen

Christopher S. Bretherton

Date: 7 August 2003

University of Washington

Abstract

Organized Layer Overturning in Mesoscale Convective Systems over the Western Pacific Warm Pool

David B. Mechem

Co-Chairs of the Supervisory Committee:
Professor Shuyi S. Chen and Professor Robert A. Houze, Jr.
Department of Atmospheric Sciences

This study employs a high resolution numerical cloud model to investigate overturning of the tropical environment by mesoscale convective systems (MCSs) occurring over the westerly onset and strong westerly regions of the large scale Kelvin-Rossby wave pattern during the Tropical Ocean Global Atmosphere Coupled Ocean Atmosphere Response Experiment (TOGA COARE). Two aspects of deep convective overturning are addressed: a tendency for some low-level inflows to be layer-like in structure and momentum transport processes by organized regions of stratiform precipitation.

Airborne Doppler radar data show that organized deep convective systems over the western tropical Pacific warm pool are often accompanied by layers of ascending inflow ~0.5-4 km in depth, deeper than that described by current theory in which only boundary layer air is thought to rise significantly in buoyant, parcel-like updrafts. Trajectory analysis of convection simulated over the strong westerly region of the large-scale Kelvin-Rossby pattern demonstrates the existence deep inflow layers. In the westerly onset simulation, the parcel model prevails, with only the air in the lower part of the inflow actually rising in the deep convective updrafts. Increasing the relative humidity of the low and midlevel environmental air brings about the layer inflow mode. Proposed moistening

mechanisms are inflow layers passing through tropical stratiform precipitation and mixing in the vertical by cumulus of moderate depth.

Extensive regions of organized mesoscale stratiform descent act to transport downward midlevel momentum at low levels, easterlies over the westerly onset region and westerlies over the strong westerly region. In the westerly onset simulation, the convective and stratiform regions compete, with the convective attempting to accelerate the westerly momentum via pressure gradient and the stratiform attempting to increase the easterly momentum through downward vertical transport. Over the strong westerly region, both convective and stratiform components act to increase the low-level westerlies. Results imply MCSs in each flow regime may exert an influence on the large scale wave structure, negative or neutral during the westerly onset phase and positive during the strong westerly phase.

# TABLE OF CONTENTS

# LIST OF FIGURES

# LIST OF TABLES

# Acknowledgements

Simply listing the names of those who helped me finally attain this feat over the past ten years seems utterly insufficient, but each played an important role. These contributions seem particularly significant, given my past four and a half years were spent in Oklahoma, away from frequent personal interaction typically ideal for research projects to flourish. Co-advisors Shuyi Chen and Bob Houze provided willing and patient guidance over my course of study. Shuyi has in quantity one of the most underappreciated qualities in science: exuberance. Bob exhibits an ability to organize a thought process that appears at the moment like coalescing order from chaos yet seems so simple and logical after-the-fact. Chris Bretherton served on my reading committee and has been an inspiration in my new area of research.

I wish to acknowledge the heroic patience of my colleagues and supervisors at the University of Oklahoma, especially Brian Fiedler, Yefim Kogan, and Peter Lamb. I would like to thank Carl Hane for his comments on the contents of Chapter 5. Thanks to Bill Beasley for our chats.

I wish to express gratitude to Jona Stutler for her support and Darwin Hostetter for his patronage.

To my dear wife and daughters, you have kept me sane, balanced, and generally cheerful throughout this whole process.

# Chapter 1

# Introduction

Convective overturning, the process by which the atmosphere attempts to remove thermodynamic instability through conversion of potential energy into kinetic, spans a wide range of depths and horizontal scales. Deep convective overturning in the tropics is frequently manifested by large, long lasting mesoscale convective systems (MCSs). Populations of MCSs compose superconvective systems (Chen et al. 1996), whose occurrence is closely linked to the large scale propagating Kelvin-Rossby wave pattern which constitutes the intraseasonal oscillation (ISO). Observational evidence suggests that the existence of organized, layered updrafts and downdrafts as shown by radar data determines the character of the overturning and its associated thermodynamic properties, and through momentum transport can affect the large scale flow properties (Kingsmill and Houze 1999b; Houze et al. 2000). That these organized ascending and descending inflows cover large areas as indicated by satellite and radar data points to their significance. This chapter will introduce discussion on the ubiquity of these MCS inflows and their influence on the overturning of the tropical atmosphere.

## 1.1 Modes of convective organization

An overall theme of this study is how the issue of mesoscale organization modulates the behavior of MCS inflows. Orlanski (1975) provides a basic classification of the degree of mesoscale organization, with meso-$\alpha$ scale defined to be between 200 and 2000 km in the horizontal with a time scale >6 hours. Meso-$\beta$ scale is defined as a horizontal scale between 25 and 250 km with a timescale <6 h. Finally, meso-$\gamma$ scale is defined to lie between 2 km and 25 km with a timescale on the order of 1 h.

The smallest and most basic convective element is the single cell (Byers and Braham 1949). The single cell consists of a buoyant updraft which rises rapidly through the troposphere and produces large amounts of liquid water and ice. The liquid and ice begin to fall through the updraft, creating a downdraft in place of the initial updraft. This downdraft is cooled significantly by evaporation of hydrometeors, and upon reaching the sur-

face, the downdraft spreads out horizontally. The strong downdraft effectively damps the updraft, leading to a storm life cycle of 30-50 min (Weisman and Klemp 1986).

The multicell storm (Byers and Braham 1949; Houze 1993) may be thought of as a grouping of single cells in different stages of development. Vigorous young cells are characterized by a strong updraft, in which hydrometeors are rapidly growing. Mature cells simultaneously contain both an updraft and a downdraft, the latter the result of hydrometeor drag and evaporation. By the decaying phase of the cell, only the downdraft and its embedded precipitation are present. Often, the gust fronts from each individual cell combine to form a large cold pool, along which new convection may develop. Growth of new cells often occurs on a preferred flank of the storm where each individual cell moves with the mean wind, but because of this continuous redevelopment, the composite storm may not move with the mean wind. Certain conditions of wind shear (vertical shear of the horizontal wind to be specific) produce favorable environments for multicellular convective storms.

Maddox (1980) referred to MCSs as "circular type" and "linear type," with the following distinction:

> It is hypothesized that the circular cloud shield of MCCs† indicates that convectively driven, mesoscale circulations are predominant. This is in contrast to severe, prefrontal squall lines whose "line" structure is imposed and modulated by larger-scale features.

Studies of squall lines published since this paper show that squall line evolution need not be modulated by large scale features but may result from the interaction between the cold pool and the ambient environmental shear (Rotunno et al. 1988). Furthermore, particularly in the tropics, the line of demarcation between squall lines and MCSs is not always

---

†. A mesoscale convective complex (MCC) is a special type of MCS defined by Maddox (1980) as a cloud shield with continuously low IR temperature $\leq$-32 °C of size $\geq$100000 km$^2$. An interior cold cloud region must be present with temperature $\leq$-52 °C and area $\geq$50000 km$^2$. These size and temperature definitions must be met for a period of $\geq$6 hours, and the aspect ratio of the system must be $\geq$ 0.7 at time of maximum extent.

clear, since squall lines with large regions of trailing stratiform precipitation can appear qualitatively similar to MCSs in satellite imagery.

In the context of satellite-observed cloud patterns, Chen et al. (1996) describe a "supercluster" (Nakazawa 1988) as a broad region of cloudiness which propagates to the east. Individual MCSs may be embedded in the supercluster and propagate toward the west. The size and duration of this variability, several thousand kilometers and lasting at least two days (Mapes and Houze 1993), lie in the boundary between mesoscale and larger scales, and hence these features presumably play a significant role in transferring energy upscale. Chen et al. (1996) introduce a related category, the "superconvective system," defined as a group of spatially and temporally associated cold cloud tops that exceed a total area of 90000 $km^2$. Because no minimum duration is imposed on the superconvective system, it can be considered a superset of the supercluster.

## 1.2 Convective organization over the tropical western Pacific

Much of the equatorial tropical oceanic environment is close to conditionally neutral. Tropical oceanic convection is generally driven by the warm, moist air supplied from fluxes across the atmosphere-ocean interface, and the lack of a strong capping inversion alleviates the need for a substantial lifting mechanism.

Although not strongly forced by midlatitude standards, tropical convection is strongly modulated by large scale equatorially trapped wave disturbances. Variability in warm pool convection is driven largely by the tropical intraseasonal oscillation (ISO) (Chen et al. 1996). Documented by Madden Julian (1971, 1972), the ISO is best described as an eastward propagating Kelvin-Rossby wave pattern, with cyclonic gyres located on either side of a symmetric Kelvin mode. This is the Gill (1980) paradigm of the ISO and provides a description of the surface wind pattern which includes a "strong westerly region," of the wave between the Rossby gyres and a "westerly onset region," located west of the transition from low level easterlies to westerlies.

Many mechanisms have been proposed to explain the large scale Kelvin-Rossby wave pattern associated with the ISO. Wave-CISK (Yamasaki 1969; Lindzen 1974), wind

induced surface heat exchange (WISHE; Emanuel 1987), radiative-convective instability (Hu and Randall 1994), and frictional destabilization (Wang 1988; Moskowitz and Bretherton 2000) are a few. The mechanisms proposed in these theories are quite sensitive to the particulars of the convective parameterization scheme and hence do not treat explicitly the effects of convection. The ISO is a convectively-coupled wave structure: the deep convection may be viewed as a forcing mechanism for the wave structure *and* a response to the wave forcing. Assuming a heating distribution will produce a reasonable wave pattern (Gill 1980), and specifying the wave pattern results in a convective response (located too far east, however) associated with low level convergence.

The period of low level westerlies in the ISO is associated with enhanced convective activity. This "active phase" of the ISO most often originates in the Indian ocean and propagates eastward, weakening as it passes Indonesia and Malaysia but strengthening as it passes over the warm pool (Chen et al. 1996). Figure 1.1 shows three successive ISO events traversing the TOGA COARE (Tropical Ocean Global Atmosphere Coupled Ocean Atmosphere Response Experiment; Webster and Lucas 1992) large scale array (LSA) and the intensive flux array (IFA) during the intensive observation period (IOP). Regions of anomalous bulk cold cloudiness index represent enhanced convective activity associated with the active phase of the wave. The phase speed of the waves, indicated by the slope of the ISO tracks in the figure, is different for each event and can vary along the propagation path. The suppressed regions propagate eastward in a manner similar to the active regions, an unsurprising result given that they are part of the same wave disturbance. Occasional westward moving intrusions into the suppressed regions correspond to tropical cyclones.

Thermodynamic differences between phases of the ISO are present in the atmosphere and upper ocean and may be accentuated by the degree of mesoscale organization during the active phase of the ISO. The TAO buoy located in the IFA shows that the SST variations over the TOGA COARE period lagged significantly convective activity. The active phase of the ISO corresponded to a decrease in SST, likely resulting from the attenuation of insolation by organized convective events and enhanced overturning of the oce-

anic mixed layer by the strong westerlies, recharging the surface layer with fresh water (Chen et al. 1996). Convective available potential energy (CAPE), a bulk property of thermodynamic instability, also varied over the course of the IOP. CAPE was ~500 J $kg^{-1}$ greater during the suppressed phase than in the active phase, with a few cases of extreme (~1000 J $kg^{-1}$) increases with time (Brown 1994).

In a satellite climatology of cloudiness over the warm pool region, Mapes and Houze (1993) analyzed regions where IR radiative temperature was <208 K and <235 K. They showed that for cloud tops colder than 208 K, 50% of cloud clusters were smaller than 300 $km^2$, but 50% of the 208 K cloud tops occurred in contiguous regions of area $>2\times10^4$ $km^2$, while the corresponding area for 235 K cloud tops was $>10^5$ $km^2$. This indicates the importance of the large, long lasting superconvective systems and suggests that they may be of vital importance in linking mesoscale processes to the large scale flow. The largest clusters† existed only during the active phase of the ISO and were present inside the IFA region on only ~10% of the COARE IOP days (Chen et al. 1996).

Individual cloud clusters composing the eastward propagating anomalous convective region move westward as an organized disturbance with a period of ~2 days. These westward propagating disturbances have a structure more coherent than the transient MCSs which delineate the disturbance, indicating that the disturbance may represent some form of wave pattern (Chen et al. 1996). The authors invoke a dispersion relation derived by Matsuno (1966) to postulate that an equatorially trapped inertio-gravity wave with a period of ~2 days might precondition the tropical atmosphere and thereby enhance its potential to support organized convection.

## 1.3 Layered inflows in TOGA COARE MCSs

Kingsmill and Houze (1999b) classify airborne Doppler radar observations of TOGA COARE convection as shallow, deep-narrow, and deep-broad. Figure 1.2a shows results of aircraft soundings which reveal the difference in boundary layer CAPE between the three classifications, the shallow category having the least CAPE, and the deep-broad

†. class 4 systems, with area >92800 $km^2$ or >~300 km (Mapes and Houze 1993; Chen et al. 1996).

having the greatest. Variations in low level moisture are responsible for the CAPE stratification between the three classes, as also evidenced by the differences in level of free convection (LFC; Figure 1.2b). The deep-broad convection, corresponding to organized MCSs, has the greatest boundary layer moisture and hence the largest CAPE and the lowest LFC (given similar amounts of convective inhibition).

Airborne dual Doppler radar data (Kingsmill and Houze 1999a) from TOGA COARE show that MCSs have inflow layers which are not composed merely of boundary layer air but rather are typically ~0.5-4 km in depth. Bryan and Fritsch (2000) have called attention to layer lifting in midlatitude MCSs, while Zipser et al. (1981) and Jorgensen et al. (1991) have observed inflows greater than the boundary layer depth in tropical convection. Figure 1.2b shows that parcels initially above 500 m would require significantly more forcing to reach their LFC compared to parcels originating in the boundary layer.

The existence of layer lifting in large MCSs over the warm pool appears paradoxical since equivalent potential temperature ($\theta_e$) and the relative humidity of the ambient environment decrease with height in this layer. For this reason it was previously thought that the air in the upper part of the inflow layer sinks and only the boundary layer air in the lower part of the inflow layer actually rises in the deep convective updrafts. Betts (1976) and Zipser (1977) advocated the concept of a "crossover zone" in the leading portion of an isolated tropical Atlantic squall line. Two-dimensional projections of trajectories of the sinking air from the upper part of the inflow layer cross over the two-dimensional projections of trajectories of the air rising from the lower part of the boundary layer. A spectrum of mixing is implied in which the parcels from low levels tend to become buoyant cores, while air parcels in the upper part of the inflow layer which entrain the smallest amount of high $\theta_e$ air while passing through the crossover zone sink to the surface, with the thermodynamic assistance of evaporation of cloud droplets (Zipser 1977). Redelsperger and Lafore's (1988) simulations of a tropical west African squall line supported the crossover zone idea. The showed that two distinctly different air masses cross each other between 1.5 km and 5 km in height, and that this crossing occurred at the convective scale and involved similar sized pockets of high and low $\theta_e$.

Several potential candidates exist in the literature to resolve the paradox of parcel versus layer lifting. Kingsmill and Houze (1999b) suggest that a deep layer of inflow might be destabilized by passing through a regions of precipitation, and that if the layer became saturated it would be rendered conditionally neutral (i.e. near zero moist static stability), enabling the entire layer to rise upon being lifted by the cold pool. Because the $\theta_e$ lapse rate indicates potential instability, as it is lifted the layer would undergo a process of convective overturning. This reasoning is attractive, since the authors show that the depth and breadth of convection during TOGA COARE was correlated with low and middle level relative humidity; therefore, the relative humidity can be thought of as a proxy for the degree of convective organization, with the most organized systems having the moistest inflows. This study will demonstrate that low- and mid-level relative humidity is strongly correlated with layer lifting and will suggest possible moistening mechanisms.

Organized mesoscale ascent (Zipser et al. 1981) is another candidate for destabilizing a deep layer and producing inflow with a layered character. Forced ascent of a potentially unstable layer will eventually result in convective overturning. Recently, Bryan and Fritsch (2000) show that slab (i.e. layer) midlatitude MCS inflows undergo mesoscale ascent and become "moist absolutely unstable," a static stability condition of $\gamma_s > \Gamma_s$, where $\gamma_s$ is the saturated lapse rate and $\Gamma_s$ is the moist adiabatic lapse rate. The authors argue that a moist absolutely unstable layer can maintain itself under continuous ascent because of the rate imbalance between the generation of thermodynamic instability and its dissipation. In this condition, the tendency to realize the instability as cellular overturning is suppressed, since saturated mesoscale ascent actually warms the middle and upper troposphere, and the convective overturning of the inflow layer tends to be manifested as a more gradual process, while the layer maintains its deep, coherent structure for a longer period of time.

## 1.4 Momentum transport processes in MCSs

Observational and modeling studies have shown that tropical deep convection can significantly modify the character of the large-scale momentum field. Schneider and

Lindzen (1976) argued that eddy momentum transport may be parameterized as the product of the updraft mass transport and the difference between in-cloud and ambient environmental momentum. This scheme has the restrictive assumption that the fractional coverage of the updrafts be much less than unity.

Studies using datasets of greater spatial and temporal duration show that MCSs can bring about a significant mean convective momentum transport (CMT) signal. Carr and Bretherton (2001a) calculated a zonal residual term from global NCEP and ECMWF reanalyses and found a slight preponderance for downgradient transport and a smoothing of the environmental shear over the four month period of TOGA COARE (November 1992 - February 1993). Momentum flux profiles computed from dual-Doppler aircraft radar observations show a four-month mean convective momentum transport characterized by the upward transport of easterly momentum by strong convective updrafts (Carr and Bretherton 2001b). Momentum flux is downgradient below the four-month mean westerly jet structure and countergradient above, with little contribution by convective downdrafts and stratiform regions. Mapes and Wu (2000) used a residual methodology to recover convective eddy momentum tendencies in long cloud resolving model simulations. They found that the CMT profile to be largely out of phase with the zonal wind profile, causing local extrema in the momentum profile (i.e. jets) to descend.

Most previous studies addressing the transport and generation of momentum by convection have assumed some sort of two-dimensional framework, where momentum fluxes are decomposed into orientations normal and parallel to a leading convective line. In a seminal observational study, LeMone (1983) concluded that organized MCSs do not transport momentum according to simple mixing theory but found momentum to be generated in the 10-20 km wide convective region, with little contribution from the precipitating stratiform area. Negative line-normal fluxes in the convective region of a squall line implied an increase in the environmental wind shear, while the line-parallel flux was largely down the mean gradient. Momentum flux was significantly influenced by the convectively generated pressure field, which accelerated horizontally air ascending into the convective line. The pressure field was nearly hydrostatic, with a pressure minimum

located over the rear of the convective line. A study of a number of cases showed that the momentum flux in 7 out of 9 tropical convective lines implied an increase in the front-to-rear momentum at heights above 4 km (LeMone et al. 1984).

Moncrieff (1992) used a three-branch dynamical model to investigate momentum flux for an idealized two dimensional convective line circulation and found it able to represent countergradient momentum flux reported in observational studies. LeMone and Moncrieff (1994) applied this dynamical model to ten previously studied MCSs and found that it produced a profile of line-normal momentum flux generally consistent with the observations. The best match between model and observations occurred under conditions of moderate instability and when the MCS contained little stratiform precipitation.

Yang and Houze (1996) demonstrated that the momentum budget over the stratiform region of a two dimensional simulated squall line can be considerably different from that over the narrow convective zone and that no particular forcing term in either region dominates how the entire MCS influences the large-scale momentum profile. In a simulation of an asymmetric tropical western Pacific squall line that included a large region of stratiform precipitation, Trier et al. (1998) found a countergradient transport of zonal momentum at mid-levels in the convective region but a more complicated behavior over the stratiform region. The authors noted that in most cases system-averaged accelerations were smaller than the individual forcing terms and that the MCS influence on the vertical shear was vastly complicated by the existence of a low-level ($z = 2$ km) westerly jet rather than the simple monotonic shear previous studies considered. They showed that the term most responsible for modifying the environmental momentum at low levels is the vertical flux divergence. Using data from a 2D cloud resolving model, Zhang and Wu (2003) emphasized momentum transport by strong cumulus updrafts and a perturbation pressure field that acts to suppress momentum transport over the westerly onset region and enhance transport in the strong westerlies.

Previous studies have explored cumulonimbus momentum transport as a function of the large scale environmental shear profile, but the role of mesoscale organization has been largely neglected. Large, long-lasting mesoscale convective systems (MCSs) are

composed of regions of vigorous convection and more expansive areas of stratiform precipitation. Moncrieff and Klinker (1997) proposed a hierarchy of interactive scales (cumulonimbus, mesoscale convective system, and supercluster) and demonstrated the importance of mesoscale organization by showing significant differences between momentum tendencies at the cumulonimbus and MCS scales. Their results indicated an important scale dependence that may emerge when convection becomes highly organized. Houze et al. (2000) demonstrated that the momentum transport features present in the Doppler radar data are strongly associated with large regions of stratiform precipitation and a significant degree of mesoscale organization. They hypothesized a mechanism based on a limited set of observations to explain how the degree of mesoscale organization influences MCS momentum transport.

Houze et al. (2000) found that MCSs occurring under different flow regimes produce different momentum transport characteristics. In the westerly onset region of the Kelvin-Rossby (KR) wave structure, located just to the west of the changeover of the low level easterlies to westerlies, MCSs transported *easterly* momentum *downward.* In the region of the wave structure characterized by the strongest low level westerlies (strong westerly region), *westerly* momentum was transported *downward.* The authors surmised that the upscale momentum feedback was negative in the westerly onset region, attempting to damp or resist the onset of low level westerlies in the propagating KR wave structure, and positive in the strong westerly region, acting to help accelerate the westerlies. Tung and Yanai (2002) paint a complementary picture, where lower tropospheric momentum transport is downgradient 60-65% of the time, except during the strong westerly phase where it is countergradient and helps to maintain the mean shear. Houze et al. (2000) furthermore argued that the addition of easterly momentum at low levels in the westerly onset region implied enhanced convergence on the western side of existing convection, favoring new cellular development in a direction opposite to the propagation direction of the KR wave pattern. Downward transport of momentum by MCSs over the strong westerly region implied additional low level convergence on the east side of exist-

ing convection, in the direction of wave propagation, as further evidence of positive feedback.

These studies illustrate the complicated interdependence of momentum flux on the dynamic and thermodynamic character of the MCS system. The perturbation pressure field responsible for accelerating the MCS inflows is nearly hydrostatic and thus is determined by the distribution of diabatic heating in the convective region, which is ultimately dictated by the instability. The interaction between ambient shear and buoyancy acceleration determines the tilt of the updraft, which along with the accelerated inflows has a strong effect on the sign of the momentum flux. Past studies have predominantly concentrated on the generation and transport of momentum by the active convective region, while the role that broad regions of organized stratiform precipitation plays has not been fully addressed. It is fair to say that despite a history of comprehensive observational and theoretical studies, the issue of MCS momentum flux has been largely impermeable to a synthesis of the body of work into a simple conceptual model, particularly in situations characterized by a high degree of mesoscale organization.

## 1.5 Scientific objectives

### 1.5.1 The nature of MCS inflow

Since tropical deep convection is an important element of the ocean-atmosphere climate system (Webster 1994), a correct understanding of convection is prerequisite to its accurate portrayal in global climate models (GCMs). Most cumulus parameterization schemes in current use are based on entraining plume or bubble models with parcel theory underpinnings, with the atmospheric boundary layer being the focus of this perspective. The $\theta_e$ of these parcels is modified by surface fluxes across the ocean-atmosphere interface, and parcels of high $\theta_e$ ascend until decelerated by entrainment or a stable layer. Downdrafts of lower $\theta_e$ descend into the boundary layer where the air may be modified by surface fluxes. This view is consistent with the crossover idea.

The overall validity of a parameterization based on the assumption of parcels rising out of and sinking into the boundary layer depends further upon the extent to which

the subgrid scale is in statistical equilibrium with the resolved system (Emanuel 1994). The notion of statistical equilibrium rests upon the idea that the temporal scale of the small-scale processes is significantly smaller than that of the resolved scale such that there is a separation of scale between the two. When mesoscale convective systems reach horizontal scales of hundreds of kilometers and take on extensive stratiform components (Zipser 1969, 1977; Maddox 1980; Nakazawa 1988; Chen et al. 1996; Kingsmill and Houze 1999a, 1999b; Houze et al. 2000), the failure of the scale separation assumption becomes possible, if not likely.

In this dissertation, I will argue that the parcel view of convection (expressed by Betts 1976, Zipser 1977, and Redelsperger and Lafore 1988) is most applicable when a dry mid-level layer is present, while layer lifting better describes the nature of inflow when the mid-levels are moistened. The parcel view would be more applicable to the early stages of an MCS, while layer lifting (Kingsmill and Houze; Bryan and Fritsch 2000) better describes the later, more mature stages of the system when an extensive region of stratiform cloud and precipitation is likely present. To make the case, I will use model calculations to trace air parcels into and through convection such as were observed over the tropical warm pool in TOGA COARE.

### 1.5.2 Character of tropical MCS momentum transport

This study seeks to examine convective-large-scale interaction in the tropical atmosphere by examining model results of MCSs occurring under two different flow regimes in the context of feedback onto the large scale KR wave structure. This study applies to model data the phenomenological approach taken by Houze et al. (2000). In contrast to previous studies that apply the method of residuals to obtain bulk momentum effects, here I calculate and analyze the spatial structure of the momentum forcing sources in simulated MCSs to infer an upscale influence of organized deep convective systems on the propagation of the KR wave structure. Of particular interest is how the transport of zonal momentum, both environmental and system-generated, by organized mesoscale circulations, influences the establishment of the strong low level westerlies over the onset and strong westerly regions of the KR structure. Previous studies have investigated

momentum processes in relation to the environmental flow. The dissertation will examine MCS momentum transports in the context of mesoscale organization, which is itself modulated by the environmental flow.

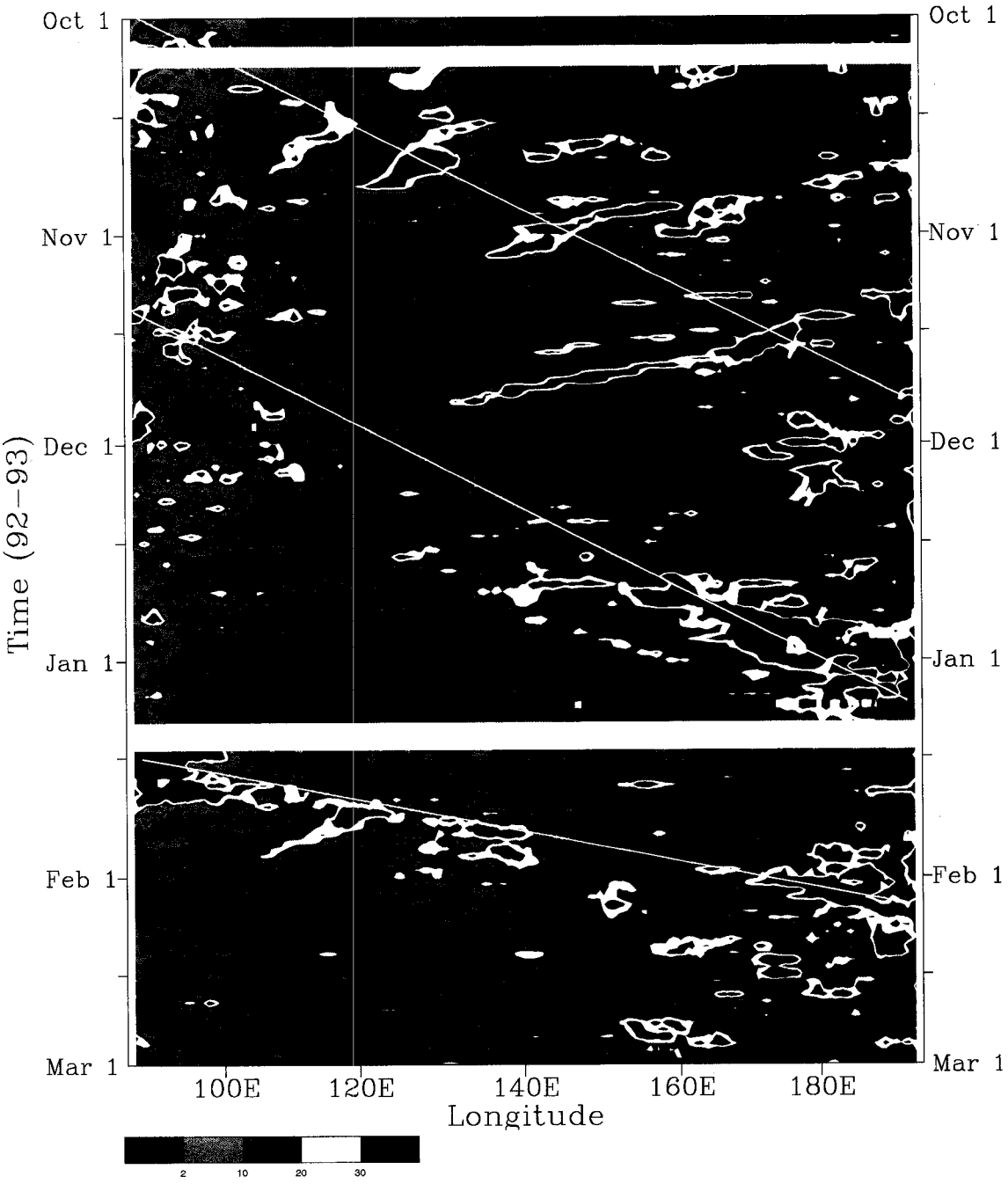


Figure 1.1. Time-longitude plot of a $PHC_{235}$ the meridional summation of the number of analysis grid boxes between 20 °S and 20 °N whose fractional time coverage of cloud with IR brightness temperature colder than 235K is >25%. (Adapted from Chen et al. 1996).

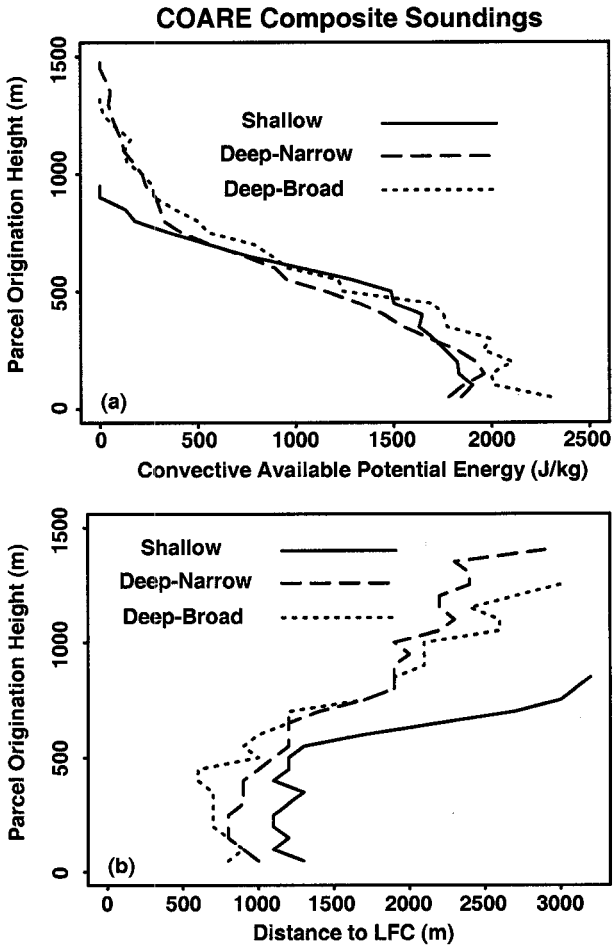


Figure 1.2. (a) Convective available potential energy (CAPE), (b) distance to the level of free convection (LFC) as a function of origination height for the three types of composite soundings. (Adapted from Kingsmill and Houze 1999b).

# Chapter 2

# Methodology

A typical methodology for a numerical experiment with a cloud model involves choosing or creating a model appropriate for the type of phenomenon being studied and the scale of interest. Initial conditions are typically horizontally homogeneous, based on a single sounding or a composite of soundings thought to be representative of the atmospheric conditions before convection has taken place. Often the sounding used is potentially unstable, so some initial perturbation must be applied for convection to occur. The initialization may be a cold pool or heat sink (Redelsperger and Lafore 1988, Thorpe et al. 1982, Yang and Houze 1995), a positively buoyant warm bubble (Klemp and Wilhelmson 1978a), a gentle, large scale ascent applied throughout the domain, or a combination of the last two (Tao and Simpson 1989).

Unfortunately, the initial condition of horizontal homogeneity combined with a simple perturbation often neglects many complicated initiation mechanisms found in nature. Horizontal variabilities such as cold pool intersections, storm-scale convergence, or differential surface heating are crudely mimicked or are absent altogether, causing some researchers to disregard the early stages of the storm and concentrate their main study on the mature and dissipating stages of the simulated convection. When using horizontally homogeneous initial conditions, zones of convergence or small local perturbations of low level $\theta_e$, so crucial to the development of a convective storm, may be absent. The difficulty in triggering convection is borne out by the creative and sometimes bizarre initiation schemes that have been conceived for previous studies.

The question of which initiation method should be used broaches the topic of sensitivity. Specifically, given a horizontally homogeneous initial condition, how sensitive is the solution (i.e. the resulting convection) to the initial perturbation? Intuition suggests that the resulting convection is sensitive to the choice of perturbation type or orientation, but this assertion is difficult to prove conclusively. This difficult question is one that could entail a complete study on its own and will not be discussed further; instead, this

dissertation takes an approach to the problem that overcomes the constraint of initial horizontal homogeneity.

## 2.1 Two model approach

### 2.1.1 Overview

Output fields from a mesoscale model initialize the cloud model. This approach overcomes the constraint of initial horizontal homogeneity often intrinsic to cloud model simulations but sacrifices the simplicity of a single sounding experiment. The number of degrees of freedom of the system (and consequently, its parameter space) is vastly increased to the point that hypothesis tests are difficult to formulate and test via a null hypothesis. For this reason, the plausibility of hypotheses is emphasized rather than outright proof.

This method has two disadvantages when compared to adding an additional high resolution mesh to the MM5. First, instead of linearly interpolating the provided hourly boundary values, the fine mesh of an MM5 would be provided boundary information every time the coarse mesh is updated. Since grid spacing ratios between coarse and fine mesh are 3:1, a new boundary value would be provided every three integrations of the fine mesh. The second disadvantage is that the method used in this study provides for only a one-way interaction between grids, so information may transfer only downscale. The addition of a higher resolution mesh in the MM5 would have allowed for a two-way interaction and thus a direct addressing of upscale feedback on the large scale flow field.

The method of initializing ARPS with previous MM5 runs as described offered us the distinct advantage of using an ice-phase microphysics package more sophisticated than that available in the MM5 at the time and provides for running sensitivity experiments at low computational expense relative to a full MM5 run.

### 2.1.2 Cloud model architecture

The numerical cloud model used in this study is the Advanced Regional Prediction System (ARPS ver 4.2.3a) (Xue et al. 1995). ARPS is fully compressible and formulated in a generalized terrain-following coordinate system. To resolve accurately the character-

istically thin tropical (COARE) boundary layer cold pools, it uses grid stretching in the vertical. Vertical grid spacing ranges from 200 m at the surface to 1000 m aloft. The vertical grid is similar to that of the MM5 used to provide boundary and initial conditions.

A 1.5-order turbulent kinetic energy-based closure scheme parameterizes subgrid scale processes. A prognostic equation for the turbulent kinetic energy equation (TKE) is solved, and the TKE is related to the turbulent mixing coefficients $K_h$ and $K_m$. A rigid top boundary condition is used in combination with a zone of Rayleigh damping to minimize reflection of internal gravity waves.

Radiative effects and surface fluxes of heat, moisture, and momentum are neglected. The rationale for ignoring surface fluxes arises from the conclusions of Trier et al. (1996) that the only added benefits of including these fluxes are slightly improved structure and evolution of certain characteristics of the system. Although in that case a squall line was the object of study, I assume that these results generalize to less organized convection. Radiative effects are ignored in view of the relatively short duration of the simulation. Surface fluxes and radiative effects arise indirectly, through the boundary conditions, since the parent MM5 simulation contains these effects.

### 2.1.3 Initial and boundary conditions

Chen (1997) performed mesoscale model simulations with the PSU/NCAR MM5 mesoscale model (Grell et al. 1994) over the Western Pacific warm pool region for several consecutive days in middle and late December 1992. The mesoscale model runs were in a nested grid configuration. A subset of the high resolution (15 km) grid as initial and boundary conditions for cloud model simulations carried out on a grid of 2 km horizontal resolution are employed. The vertical resolution is similar in both models. The technique used here is in principle quite similar to the approach used successfully in the Mesoscale Alpine Project (MAP), where the Swiss mesoscale model initialized with the European Centre for Medium-Range Weather Forecasts (ECMWF) analysis fields supplied the initial and lateral boundary conditions for the high-resolution Canadian MC2 for real-time forecasts during MAP (Bougeault et al. 2001). In this study, the MM5 is initialized with a mesoscale analysis field that uses the ECMWF global analysis and additional TOGA

COARE soundings and surface observations. The quality of the MM5 simulations is limited by the ECMWF analysis fields and the relative coarseness of the TOGA COARE soundings.

The available input data from the mesoscale model consist of three wind components, temperature, pressure, water vapor, rain water, cloud water, and cloud ice. The last two quantities, by definition, have zero terminal fall speed. An ARPS external data preprocessor ingests the MM5 fields and interpolates them onto the ARPS grid. A single application of a 9-point filter smoothes the data. The MM5 fields were already reasonably smooth, so they did not require multiple applications of the filter. The vertical velocity is diagnosed from the horizontal wind components of the MM5 via the anelastic continuity equation. The MM5 uses an ice-phase parameterization that allows snow and ice but not mixed phase hydrometeors. Because of significant differences in microphysical parameterization scheme, ARPS did not use the MM5 hydrometeor fields. Although neglecting these fields possibly delays the development of convection, the ARPS hydrometeor fields quickly adjust to the circulation imposed upon them by the mesoscale model. A schematic of the initialization process is shown in Figure 2.1.

A relaxation boundary condition in ARPS (Davies 1983) forces the lateral boundaries, using the hourly mesoscale model data. In this scheme, forcing terms of the form

$$\frac{\partial}{\partial t}\bar{\rho}\phi = -K_b\bar{\rho}(\phi - \phi_e),$$

linearly interpolated between two times where boundary value data are available, are added to the right hand side of the prognostic equations. The relaxation coefficient $K_b$ is maximum at the boundary and decreases to 1/5 of this value at the inner edge of the zone, which gently but firmly forces the boundary solution towards the external value (Xue et al. 1995).

Because of widely different scales, microphysical parameterizations, and other model details, there is no reason to believe that the ARPS simulation will evolve exactly like the MM5 run which supplies the boundary conditions. Additional computational mixing is added in the boundary zone to control possible noise introduced by the inconsis-

tency between the interior (model) and exterior (forced boundary) solutions. This mixing is a second order diffusion term which acts on the difference field between the internal and external (boundary) solution.

## 2.2 Importance of the microphysical parameterization

The microphysical parameterization is critical for achieving the objectives of this study, since the emergence of mesoscale organization is necessarily accompanied by the development of mesoscale stratiform precipitating clouds. The parameterization must be tuned to represent reasonably this part of an MCS.

### 2.2.1 Rationale

After applying a steady-state cloud model to a GATE squall line case, Rutledge (1986) postulated that the condensate produced at mid-to-upper levels by mesoscale ascent is largely responsible for the large horizontal extent of stratiform precipitation. Using the same model with high-resolution Doppler-derived winds sampled from a mid-latitude squall line as input, Rutledge and Houze (1987) found that vapor deposition in the mesoscale ascent region was responsible for 80% of the stratiform precipitation. Fovell and Ogura (1988), McCumber et al. (1991) and Yang and Houze (1995) used cloud models to arrive at similar conclusions. McCumber et al. (1991) found that the inclusion of ice-phase processes enhances the agreement between the simulated convection and certain observed features, notably the amount of stratiform precipitation and the intensity of the radar bright band near the melting level.

The long-used LFO scheme (Lin et al. 1983), modified to better represent warm pool microphysical processes, is employed in this study. The fact that mesoscale convective systems contain both a strong convective region and a stratiform region presents difficulty for most ice phase microphysical parameterization schemes (McCumber et al. 1991). Appropriate adjustment of parameters can make the snow category represent aggregate snowflakes or small graupel. The hail category can represent either true hail, graupel, or aggregate snowflakes. As discussed in more detail below, the snow category is tuned to have properties characteristic of ice crystals or unrimed or lightly rimed aggregates. The

hail category is tuned to have some of the qualities of rimed aggregates, particularly their fallspeed. The rationale is that this field will act graupel-like in the convective region of a mesoscale convective system and more aggregate-like in the stratiform region of the same system. In this dissertation the term graupel/aggregates refers to this hydrometeor category. In the convective regions of mesoscale convective systems, this field grows rapidly, mainly by accretion of cloud water. In the stratiform region, where less cloud water is present, this quantity grows by aggregation of snow (specifically autoconversion (aggregation) of snow to form graupel and by the subsequent accretion of additional snow and cloud ice in the parameterization).

### 2.2.2 Tuning the model microphysics

Of course, the tuning does not perfectly capture the characteristics of both graupel and aggregates. It is possible that, since the fall speeds are less than what characterizes typical graupel (see discussion below), the residence time of the species in a vigorous convective updraft will be unrealistically long, and therefore, too much cloud water would be depleted. In the stratiform region, depositional growth of this category is neglected, although it does act on the snow particles which eventually become aggregates.

Parameters of the LFO model can be tuned to produce aggregates, graupel or hail, the primary difference being the magnitude of the hydrometeor fall speed, and this tuning can lead to accurate portrayal of the hydrometeor distribution in a convective updraft, where hail or graupel growth processes (riming and accretion) are active. Vapor-grown particles, aggregates, and lightly rimed particles, formed and initially grown in a convective region, need to make their way into the stratiform region where they can continue to take on mass by vapor deposition. Over-representation of the graupel and hail needed for realistic convective cells diminishes the possibility for growth of a robust precipitating mesoscale stratiform cloud layer. Optimization of choices of model parameters leads to the best combination of convective cells and stratiform cloud deck, probably with neither being completely realistic. This is the nature of bulk microphysical parameterization.

Originally designed to simulate a midlatitude continental high plains thunderstorm, the LFO scheme is probably best suited to storms which contain a significant

amount of hail. Over tropical oceans very little if any hail is present, so clearly the LFO parameterization must be modified to produce a realistic precipitation pattern. What is desired is a selection of parameters that enables the parameterization scheme to produce both small graupel and vapor-grown snow. Therefore, I modify the fall speeds, particle-size-distribution parameters, and hydrometeor density. The fallspeed is the most critical of these parameters. The LFO scheme contains two precipitating ice fields, snow and hail, and a cloud ice field, which has zero fall speed. To compute the terminal velocity of rain and snow, a relation of the form $u = aD^b$ is assumed, where $u$ is terminal velocity, $D$ is precipitating particle diameter, and $a$ and $b$ are empirically derived constants. The rain water, snow and hail fields have an assumed inverse exponential, Marshall-Palmer size distribution, from which mass-weighted mean terminal velocities can be derived. As such, the terminal velocities are dependent only upon hydrometeor mixing ratio. LFO terminal velocities for snow, rain, and hail are shown in Figure 2.2a.

For tropical convection, McCumber et al. (1991) suggested using the Rutledge and Hobbs (1984, hereafter RH84) scheme or, because of the similarity of the two schemes, using the RH84 parameters† into the LFO scheme. An extension of this approach is that developed by Potter (1991) and used by Yang and Houze (1995). This method makes use of Locatelli and Hobbs's (1974) empirical fall speed relations for various types of solid precipitation particles. Their category "graupellike snow of hexagonal type" is used for the LFO snow field, and "hexagonal graupel" is used for the LFO graupel/aggregate field. As discussed in Potter (1991), the particle diameter used in the derivation of the fall-speed relations represents the diameter of the melted particle, and for consistency the densities of the ice substances must be changed to the density of liquid water. Figure 2.2b shows the fall speeds for the precipitating hydrometeors represented by this scheme.

Following Braun and Houze (1994) the microphysical scheme is modified to omit the density correction term in the snow fall speed equation. They argue that there is no experimental evidence to support the inclusion of this term, and that using it gives unreal-

†. Here, "parameters" refer to the hydrometeor densities, intercept parameters of the hydrometeor distributions, and the empirical constants found in the fall speed relations.

istically large snow fall speeds at upper levels in comparison to fall speeds derived from Doppler radar extended velocity-azimuth display analysis (Rutledge et al. 1988; Biggerstaff and Houze 1993). The graupel/aggregate production terms were also slightly changed. The hail fall speed relation in LFO had a drag-coefficient form. Since a graupel/aggregate category has replaced the hail category, the drag coefficient form is dropped, allowing use of a fall speed relation of the form $u = aD^b$. Appendix A details the specific changes made.

### 2.2.3 Aggregation and melting in the stratiform region

Having tuned the ice hydrometeor categories to let "snow" be "graupel-like snow of hexagonal type" snow is assumed to be composed of individual ice crystals, which may have grown partially by riming. Having tuned the "hail" category to represent "hexagonal graupel" this category is termed aggregate/graupel hydrometeors, and it is more graupel-like in the convective region and more aggregate-like in the stratiform region. The behavior of this species in the stratiform region is thus in accord with observations and studies previously mentioned which show that vapor grown particles and aggregates predominate in this region. In the LFO scheme the snow can aggregate to form ice by a process of autoconversion. The parameterization allows the snow particles to aggregate with each other. The aggregated mass is sent to the aggregate/graupel category. One purpose of this tuning of the microphysical scheme was to represent more accurately the ice-phase microphysics in the stratiform regions of mesoscale convective systems. The aggregated snow mass sent to the aggregate/graupel category in the model falls through the 0 °C level and melts to form a strong melting layer similar to those seen on radar in the stratiform regions of mesoscale convective systems (Leary and Houze 1979).

## 2.3 Trajectory analysis methodology

One purpose of this study is to diagnose the nature of the inflow of air into convective systems, so parcel or particle paths are desired. These paths are obtained by calculating trajectories from 2-minute model output wind fields using the method of Doty and Perkey (1993), detailed in Appendix B. Preliminary work on this project demonstrated

that, idealized thermodynamic conservation properties notwithstanding, trajectories were a poor proxy of "parcel" path. Conservative thermodynamic variables were usually *not*, the notable exception being tracers passing through deep, strong convective updrafts. Elsewhere, turbulent mixing was dominant, quickly and systematically destroying the identity of an erstwhile parcel. Diabatic processes were also significant (e.g. passing through a melting layer) in violating the assumptions of simple parcel theory.

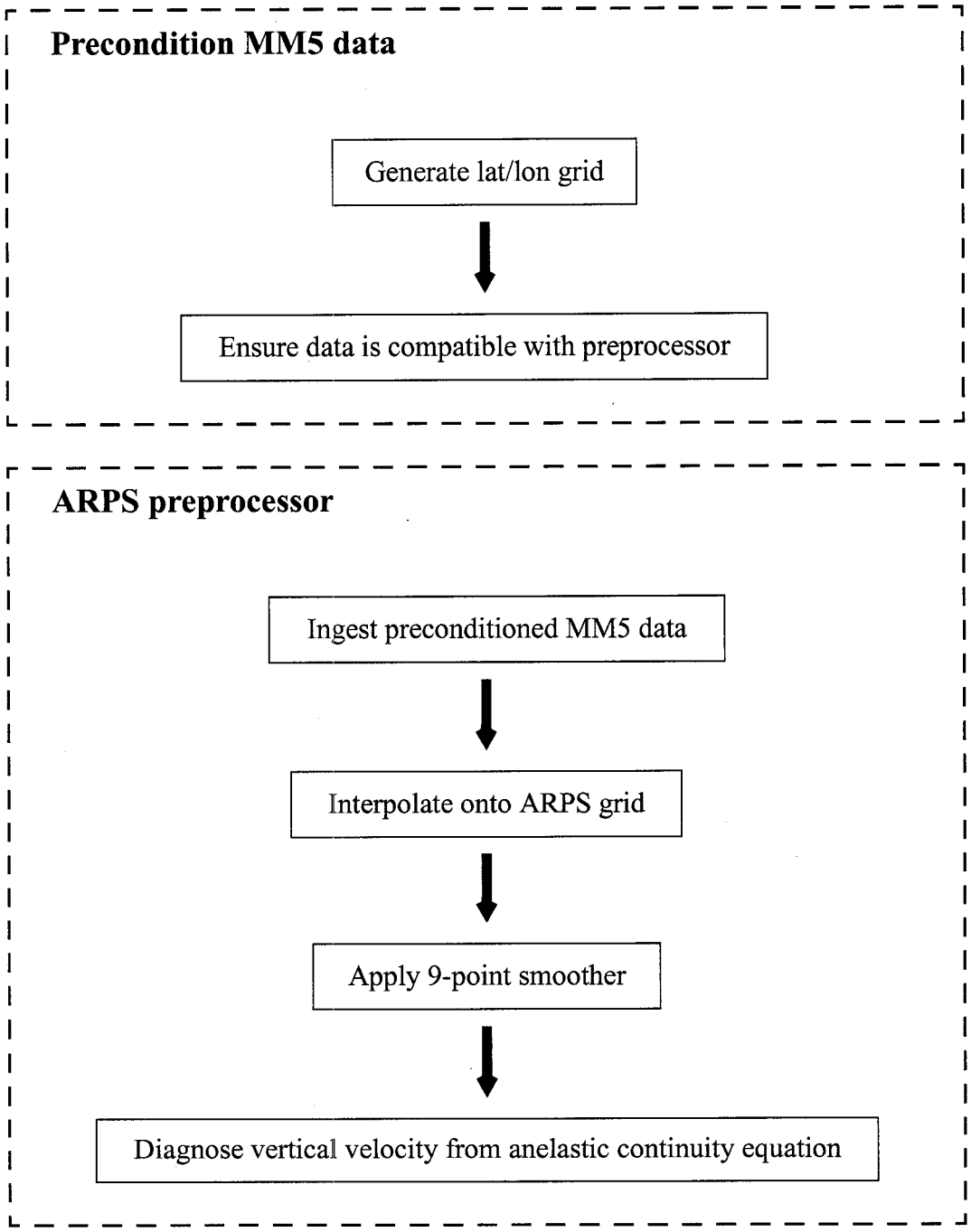


Figure 2.1. A flowchart describing the processes involved in enabling ARPS to use MM5 output data. Modules enclosed by the dotted lines comprise a particular software package.

(a)

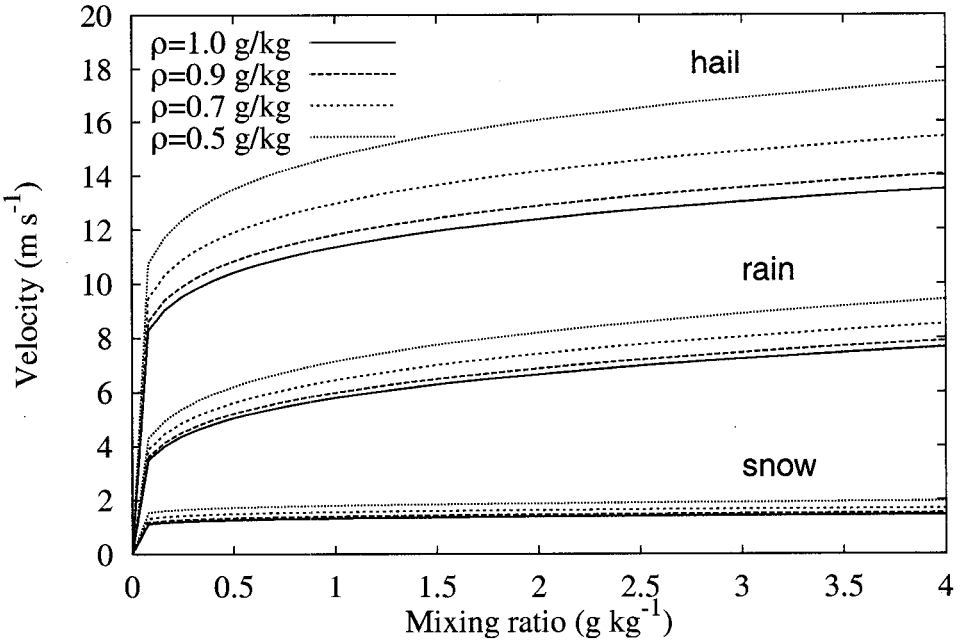


(b)

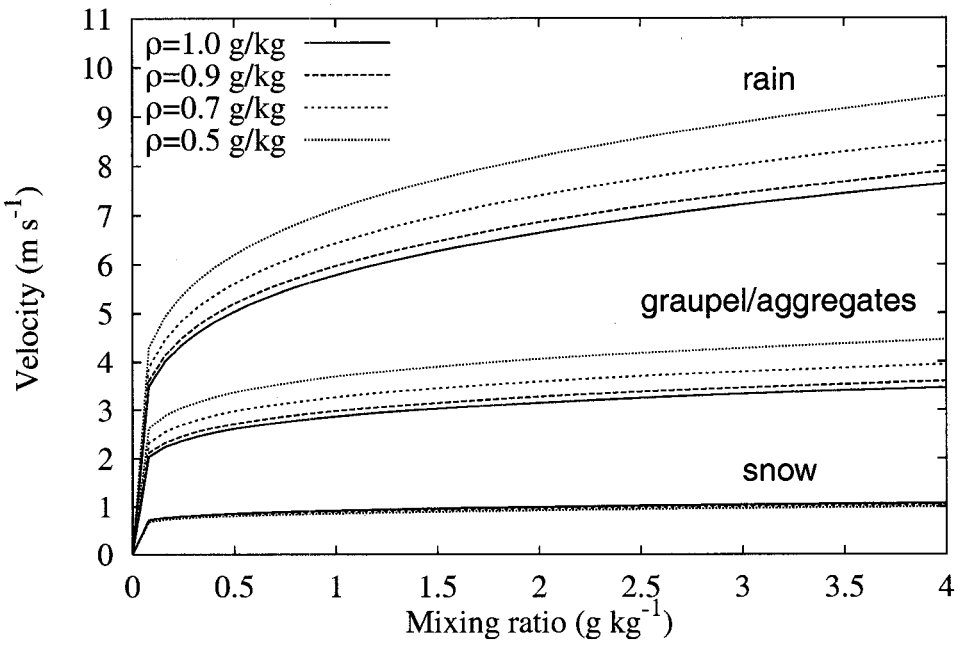


Figure 2.2. Terminal fall speeds for (a) snow, rain and hail in the LFO scheme and (b) snow, graupel/aggregates, and rain in the Potter scheme. Dependence on altitude is shown by calculating fall speeds with four different values of ambient air density

# Chapter 3

# Layer Inflow over the Strong Westerly Region

## 3.1 Environmental conditions of the 23 December case

Chen et al. (1996) and Godfrey et al. (1998) have described the general atmospheric and convective conditions over the western Pacific warm pool during TOGA COARE (November 1992-February 1993). Two cycles of the Madden and Julian (1971, 1972) intraseasonal oscillation (ISO) affected the warm pool region during TOGA COARE. Each ISO cycle culminated over the TOGA COARE region in a large-scale Kelvin-Rossby wave pattern with cyclonic gyres on either side of the equator, low-level westerly winds (called westerly wind "bursts") and extensive convective activity over the TOGA COARE region (Harrison and Giese 1991; Young et al. 1995; Lin and Johnson 1996; Chen et al. 1996; Houze et al. 2000). The focus is on December 1992, when some of the most widespread and intense convection of TOGA COARE occurred over the warm pool in association with the onset and peak of a strong westerly wind burst.

The western Pacific warm pool region in late December of TOGA COARE was characterized by the strong westerly regime of the Kelvin-Rossby wave. This regime was the most convectively active of TOGA COARE (Chen et al. 1996). It was characterized by "super cluster" conditions (Nakazawa 1988; Mapes and Houze 1993; Chen et al. 1996), with densely packed large MCSs within the region of strong low-level westerly winds (e.g. Figure 3.1). This period was dominated by the presence of simultaneous mesoscale convective systems, often with stratiform regions ~500,000-1,000,000 $km^2$ in horizontal dimensions described as "super convective systems" by Chen et al (1996). The extensive and long lasting regions of stratiform precipitation observed during this time period imply a high degree of mesoscale organization that provided ample opportunity to moisten layers of air that could eventually become MCS inflow. The MM5 was initialized at 1200 UTC on 23 December 1992. The coarse-grid version of the MM5 was run over the TOGA COARE Large Scale Array (LSA) under the strong westerly regime to provide initial and boundary conditions for ARPS. Figure 3.2a shows this region and the low-level strong

westerly conditions prevailing at this time. Approximately six hours of spin-up time was required before reasonable initial fields were available, which could be used by ARPS. The MM5 developed an MCS in the northeast corner of the fine mesh domain with a region of extensive precipitation. Although the MM5 is expected to give only a plausible response to large-scale conditions and not necessarily be a perfect match with observed MCSs, satellite imagery from 23 December shows an extensive cold cloud shield symptomatic of a significant convective event in a location similar to the simulated MCS (cf. Figs. 3.1 and 3.2a). The simulated region of convection formed a few hours before the time shown but well after the spin-up had been accomplished.

## 3.2 The 23 December simulation

The ARPS model is initialized with MM5 output from a run in which the MM5 was set up with an outer domain of ~5000 km × 2500 km, slightly larger than the LSA, and an inner domain of ~2500 km × 1500 km, which includes the TOGA COARE Intensive Flux Array (IFA, see Godfrey et al. 1998 for details of the TOGA COARE observational array). Horizontal grid spacings for the coarse and fine meshes were 45 and 15 km, respectively, and both domains contained 25 vertical levels (Chen 1997).

For this experiment, the ARPS domain is 145 × 101 × 35 points, centered at 0.4°N and 168°E, and the initial conditions are a subset of the 2000 UTC 23 December 1992 MM5 fields (Fig. 3.2b). Table 3.1 provides a synopsis of the control simulation parameters for this case. In the early stages, initial convective bands form in locations of horizontal confluence (Fig. 3.2). At three hours (Fig. 3.3a and c), an extensive region of precipitation has developed, structured in two main bands oriented from northwest to southeast. From the orientation of the cold pool (not shown), it can be inferred that the northeast side of the precipitation area is the leading edge that provides upward forcing for the storm-relative inflow. By 6 hours (Fig. 3.3b and d), the southwest band has decayed, and the cold pool has propagated toward the northeast as a density current. New convection forms along the propagating cold pool boundary in an almost continuous cycle, and both convective and stratiform elements coexist. Calculating reflectivity from model out-

put can be problematic and is quite sensitive to the assumptions made by the model microphysical parameterization. The calculation used here is rather crude, and while it produces reasonable spatial patterns, the magnitudes are significantly larger than those found in nature (Nesbitt et al. 2000).

Results from the ARPS simulation show a similar structure and evolution when compared with the "parent" MM5 simulation. Both the MM5 and ARPS produce a two-banded structure, of which the southwestern band decays with time. Another indication of how closely the solutions match is found near the boundaries. A smooth transition from the interior solution to the boundary zones is an indication that the models evolve in a similar manner. Furthermore, both ARPS and the parent MM5 simulation evolve in a manner similar to an actual MCS present in the 23 December 1992 satellite imagery shown in Fig. 3.1. It must be kept in mind that the ARPS simulations are incapable of capturing an entire MCS, much less the large cloud superclusters characteristic of the strong westerly region, but instead represent only a region or subset of an MCS. Some indications of banded structure are present in the satellite imagery. The simulated convection mimics the life cycles of the more intense areas, as inferred from cloud-top temperature. The individual convective bands move slowly toward the northeast in the ARPS and MM5 simulations, whereas they remain nearly stationary in the observations. The MM5 represents well the development of new convection toward the southwest of this large MCS, though of course the ARPS domain is far too small and its location too distant to capture it.

## 3.3 Trajectory analysis and layer inflow

To investigate the nature of the inflow into the simulated convection, six hundred earth-relative trajectories were computed using the method of Doty and Perkey (1993), calculated from ARPS output data beginning at 2 h. The initial tracer locations are inside a volume 20 km × 90 km in the horizontal and 5.7 km in the vertical, placed on the northeast side of the MCS (box in Fig. 3.3a) in an area judged to be an inflow region. Trajectories for a selected column of tracers are shown in Fig. 3.4. At low levels, the wind is mostly northerly at the initial time. The storm-relative motion that carries the tracers into the

developing MCS is determined by a combination of the cold pool propagating toward the northeast and easterly winds being advected into the domain through the northern boundary. It is also likely that the system-generated pressure perturbation pattern is acting to turn the wind with time such that it contains a more easterly component. After being transported toward the south-southwest for approximately an hour, the tracers in Fig. 3.4 enter a strong region of convective updraft, upon which nearly all of the trajectories ascend to varying degrees.

Figure 3.5 shows three different but related perspectives on the behavior of the ensemble of trajectories. As expected and indicated by the sample column of trajectories, the layer mode of inflow is clearly present in this case. Near the surface and up to a level of 1200 m, 95% of the trajectories rise more than 500 m. Even for trajectories with an initial altitude of 4200 m, nearly 40% ascend more than 500 m. The character of the descending trajectories indicates that a significant number of the upper level trajectories ($z_0$ = 5700 m) experience very little change in altitude, with only 8% of trajectories descending more than 500 m from their initial altitude. The behavior of the descending trajectories could be the result of weak evaporative cooling associated with near-saturation conditions over a deep layer, which may result in fewer descending trajectories. This sensitivity to midlevel environmental humidity is explored in Chapter 4.

Table 3.1. Control simulation parameters for 14 and 23 December 1992 cases.

| Parameter | Value |
|---|---|
| Domain width (EW) | 284 km |
| Domain width (NS) | 196 km |
| Domain height | 19.2 km |
| Horizontal grid spacing | 2 km |
| Vertical grid spacing (in PBL) | 200 m |
| Vertical grid spacing (average) | 600 m |
| Timestep (large) | 12 s |
| Timestep (small) | 3 s |
| Length of simulation | 6 h |
| Initial conditions | Horizontally inhomogeneous values of horizontal velocity, temperature, pressure, and water vapor supplied by MM5 output data |
| Boundary conditions | Linearly interpolated in time from hourly MM5 velocity, temperature, pressure, and water vapor data. |

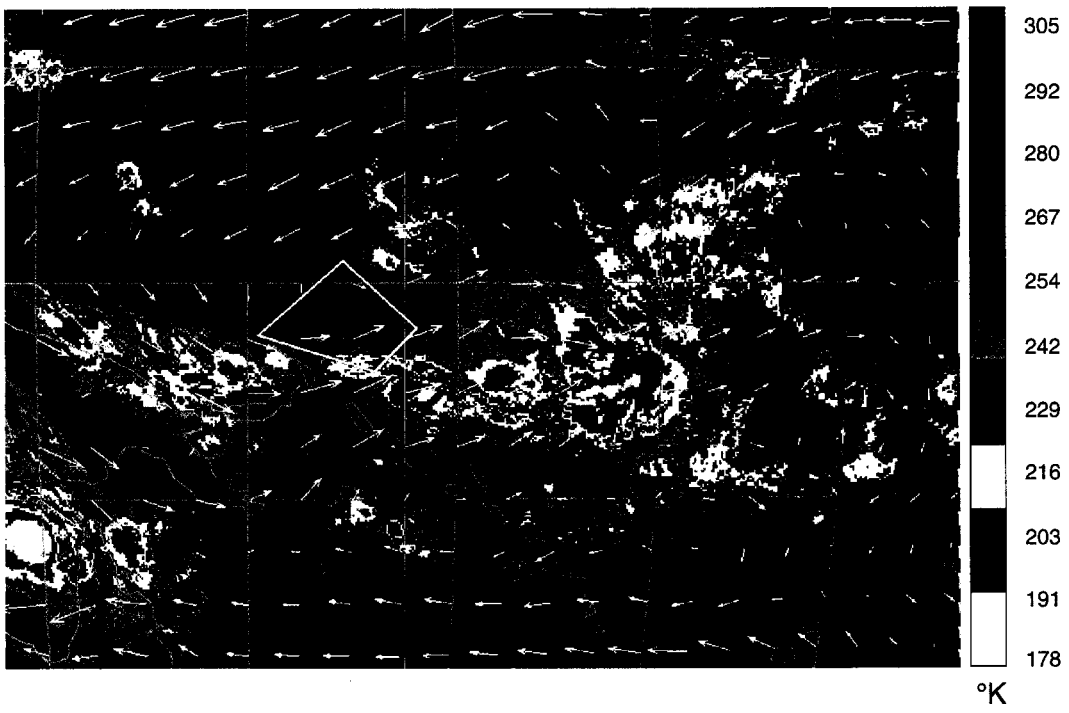


Figure 3.1. GMS IR imagery and 850 mb ECMWF winds at 2000 UTC 23 December 1992. The box encloses the TOGA COARE intensive flux array (IFA). Wind vectors are plotted every 2.5° and are scaled such that a 20 m $s^{-1}$ wind is represented by a vector that would be 2.5° in length on the map at the equator.

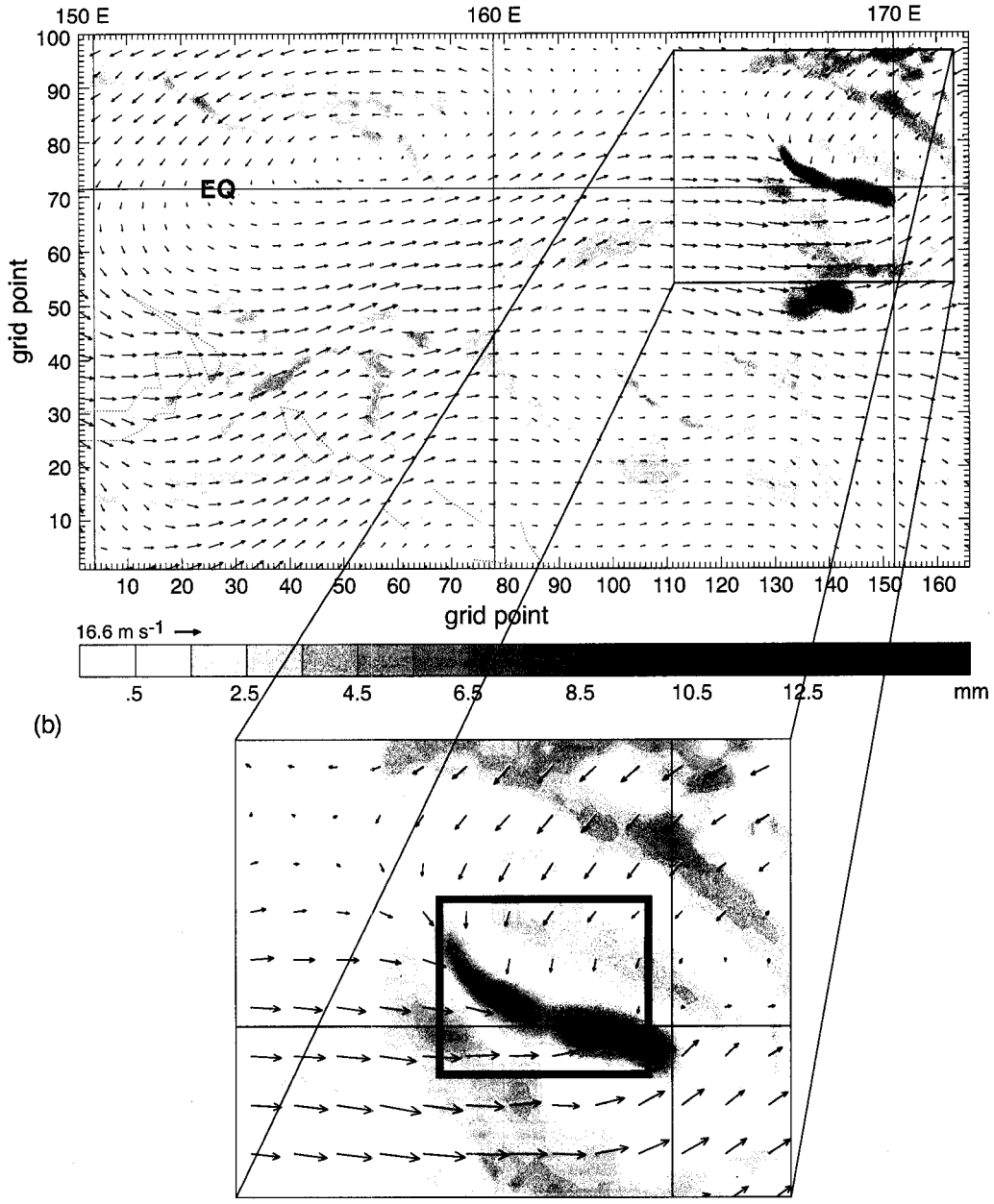


Figure 3.2. (a) 2000 UTC 23 December 1992 horizontal cross section of 850 mb wind and hourly accumulated surface rainfall from the 15 km grid of the MM5 simulation. (b) Magnification of the north-east region of (a). The ARPS (see text) model domain is enclosed by the rectangle centered at 0.4 °N, 168 °E.

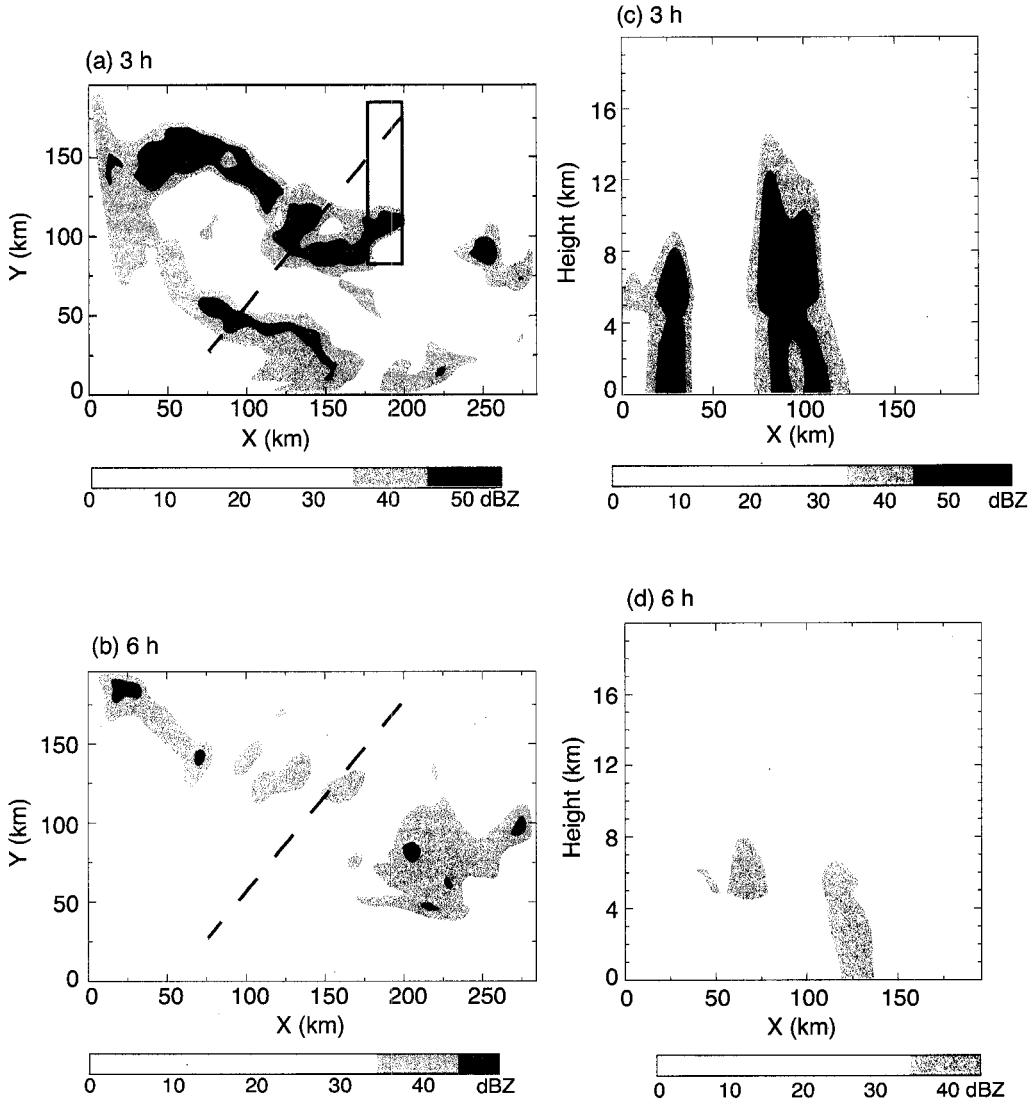


Figure 3.3. Model-derived radar reflectivity for the 23-24 December 1992 experiment: (a) and (b) 1 km horizontal cross sections and (c) and (d) vertical cross sections taken along the dashed lines in (a) and (b). The box in (a) indicates the horizontal span of the initial tracer distribution used in the trajectory calculations.

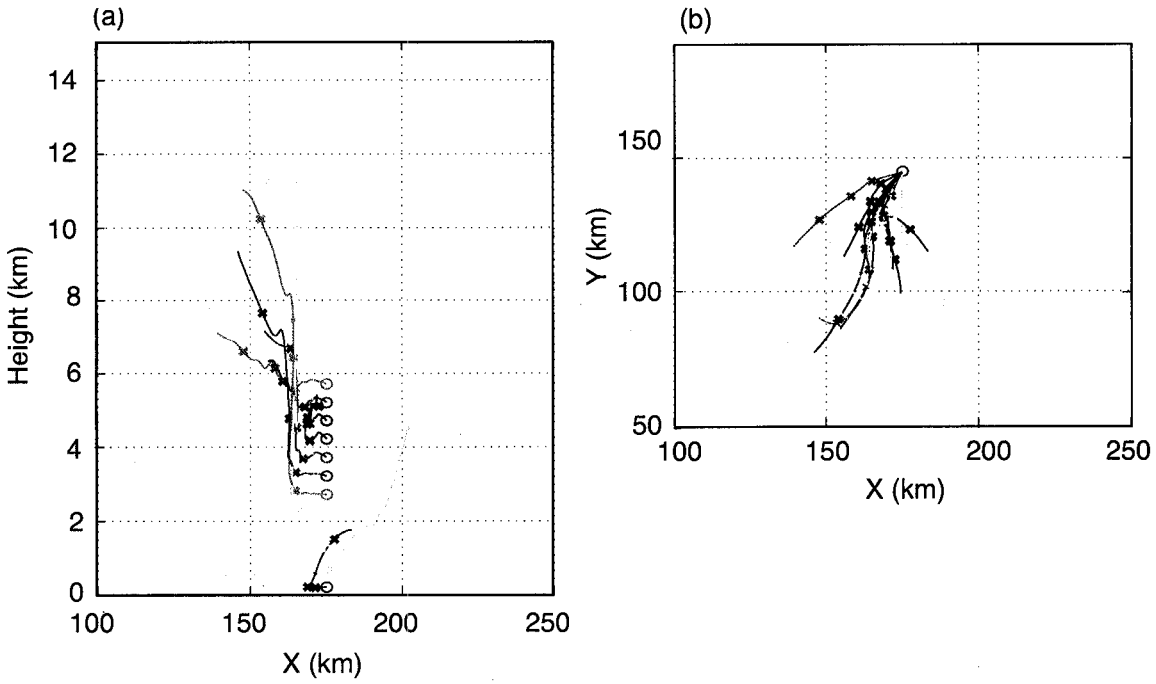


Figure 3.4. Two perspectives of 12 trajectories, each calculated over 3.5 hours of model time, for the 23-24 December 1992 simulation. Initial tracer locations are located at least 500 m apart in a vertical column. Initial locations are marked by o's, with hourly positions denoted by x's. (a) Projection of the trajectory paths onto the x-z (west-east) vertical plane and (b) projection onto the x-y (horizontal) plane.

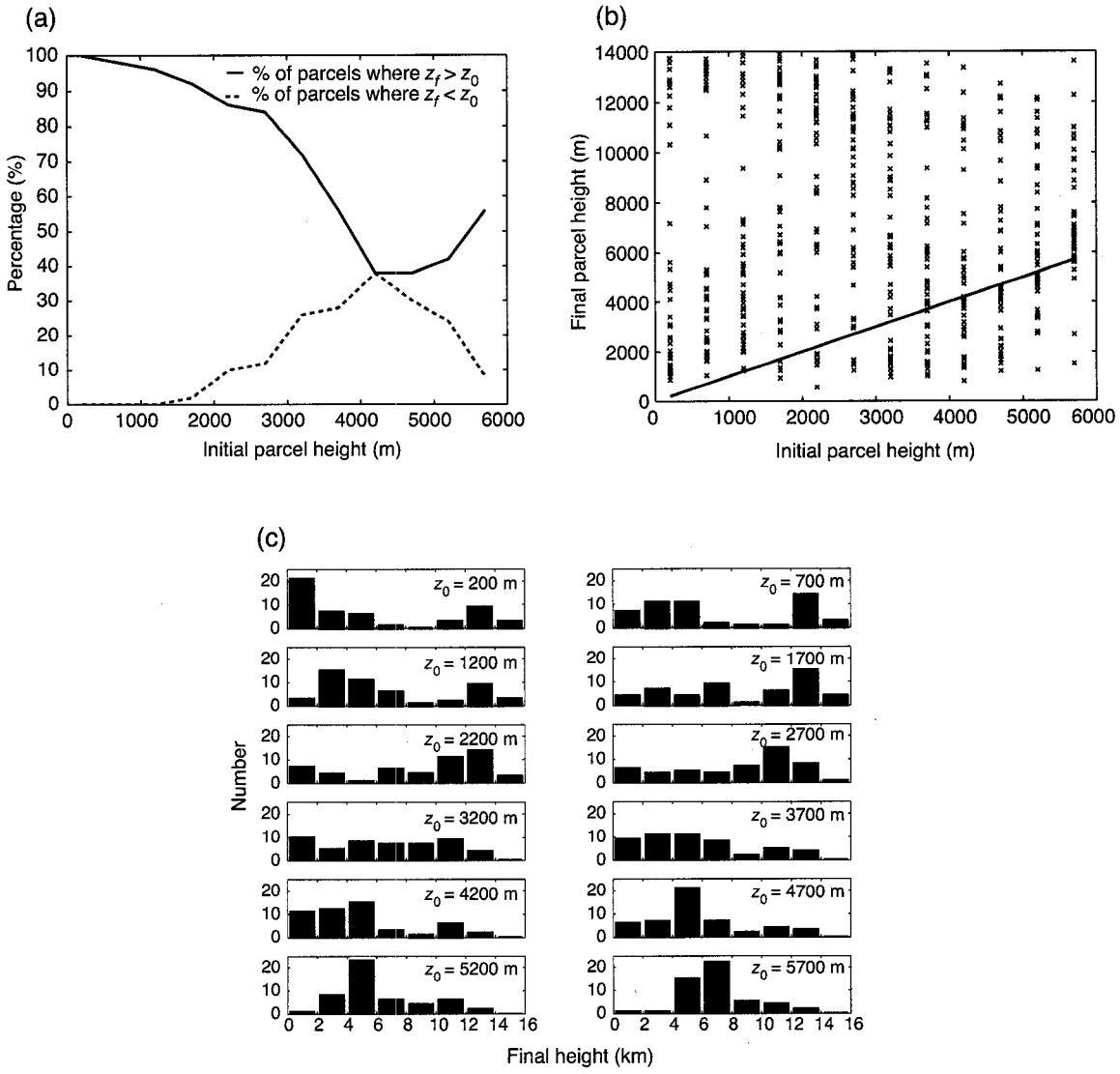


Figure 3.5. Statistics calculated from all 600 trajectories for the 23-24 December 1992 experiment. (a) Percentage of trajectories whose final altitudes, $z_f$, are 500 m higher (solid line) or 500 m lower (dashed line) than their initial altitudes, $z_0$. The sum need not add to 100%. (b) Scatterplot of all 600 trajectories, plotted as tracer final altitude as a function of initial altitude. Plotted values lying along the line correspond to trajectories that experience little change in elevation over their paths. Points above the line indicate tracers that rise, and points under, tracers that descend. (c) Histograms, each indicating the final altitude distribution of the 50 trajectories corresponding to the indicated initial altitude.

# Chapter 4

# The Westerly Onset Region: Parcel and Layer Inflow

The trajectory behavior in the 23 December experiment is indicative of a strong layer inflow signal, since a layer of air much deeper than the tropical boundary layer rises as it is ingested into the MCS. This chapter discusses similar experiments made under the westerly onset regime and how the mode of inflow in the simulated convection is strongly modulated by the vertical thermodynamic structure of the inflow.

## 4.1 Environmental conditions of the 14 December 1992 case

The 23 December case described in the previous section occurred during a westerly wind burst, a 2-3 week period of strong, deep westerlies and widespread occurrence of mesoscale convective systems over the warm pool. The westerly wind burst was preceded by a westerly-onset period, 12-16 December, during which low-level westerlies and midlevel easterlies prevailed over the COARE area (Chen et al. 1996; Houze et al. 2000). This period marked the beginning of the frequent occurrence of large mesoscale convective systems, after a long period of convective inactivity. The mid-upper tropospheric moisture increased during the onset period. The main differences between the onset period and late December were: 1) mid-level moisture was less than during the wind burst period (Lin and Johnson 1996; Chen et al. 1996); 2) convective activity was intense but not as widespread as during the burst; 3) the layer of westerlies was shallower than during the wind burst and overlain by easterlies in mid-levels.

On 14 December 1992 (Fig. 4.1), westerly conditions were beginning to develop over the COARE region, and later in the day a mesoscale convective system was observed in detail by the Doppler radar on board instrumented aircraft (Kingsmill and Houze 1999a, b). The input data for the MM5 and ARPS models are not precise enough to simulate a specific system occurring on a given date. Nonetheless, by initializing the ARPS with the MM5 output for this day, I expected to simulate a mesoscale convective system with properties reasonably similar to that observed by the aircraft. Accordingly, the first results shown are for the ARPS simulation initialized by MM5 output for 14 December 1992.

The MM5 was initialized from the ECMWF global analysis fields, National Centers for Environmental Prediction global SST analysis and, where present, TOGA COARE soundings (Chen 1997). This method captures the large-scale flow field. Mesoscale variability, such as preexisting precipitation or cold pools absent in the large-scale fields, "spin-up" in the MM5. The southern portion of the MM5 domain in Fig. 4.2a shows a region of convection that forms after the model spin-up has been accomplished. Convection begins three hours prior to the time shown, and a cold pool has rapidly propagated toward the east, triggering the new convection investigated in this study.

ARPS was employed in a manner similar to the 23 December experiment. The ARPS domain was 145 × 101 × 35 points and was centered at 5.4°S and 161.9°E. Initialization data were a subset of the 0800 UTC 14 December 1992 MM5 fields (Fig. 4.2b, chosen because of its location in a region of strong model-produced convection). The initialization time was at the early stages of the convection but late enough that precipitation and a significant cold pool had already formed.

## 4.2 The 14 December simulation

Figure 4.3 shows the evolution of the simulated convection via cross sections of model reflectivity at hourly intervals. Early in the simulation, a broad band of precipitation oriented from north to south forms in response to a line of convergence oriented in the same manner. The line of convergence associated with the convection is stronger in the northern part of the domain, and the convection begins there earlier and is ultimately more intense. The system strengthens and becomes more organized between 1 and 2 h, and by 3 h has already begun to weaken. The leading edge of the convection moves toward the east at a rate of ~10 m $s^{-1}$. After 3 h, the system weakens and becomes more disorganized, with no new convection being triggered by the propagating cold pool.

The vertical cross sections (Fig. 4.3d-f) show the evolving structure of the convection. At earlier times, the system is mostly convective in nature and is thus dominated by intense updrafts and downdrafts. As time advances, cloud ice and snow are advected toward the rear of the system (toward the west) where they grow by vapor deposition,

aggregate, and slowly precipitate. (Aggregation in the model occurs through the autoconversion of snow into the graupel field. Since the low fall speed of graupel in the model is similar to that of aggregates, the graupel field in the stratiform region may be thought of as being roughly representative of snow and ice aggregates. This view is consistent with McCumber et al. (1991)). When the precipitating ice hydrometeors melt, they produce a feature similar to a bright band at the melting level (Fig. 4.3f), even without accounting for the reflectivity enhancement associated with a liquid water layer on the snow particles falling through the melting zone. This frame also shows the leading edge of the cold pool, which has propagated ~80 km ahead of the system. Evidently, the conditions at the gust front (Rotunno et al. 1988) do not favor additional convective development. What is left at this time is the decaying stratiform portion of the convection, which results from rearward advection of ice particles and their subsequent growth and sedimentation in the mid-to-upper levels in the remnants of older convective updrafts (Houze 1997).

Direct verification of the simulation is difficult, and although realistic initial and boundary conditions are used, it must be emphasized that the results do not represent any particular case study but rather an idealized response to thermodynamic and flow profiles appropriate to a particular phase of the ISO. Nonetheless, the structure and evolution present in the simulation is consistent with TOGA COARE observations. Dual-Doppler radar observations from a portion of a mesoscale convective system observed during TOGA COARE on 14 December, the day represented by the simulation, show the transition from a mostly convective to a more stratiform regime (Fig. 4.4). In its early stages, the system is characterized by vigorous, deep convective towers and a narrow region of intense rainfall at the surface (Fig. 4.4a, c). At this time, the system is associated with a region of horizontal convergence located near the strongest convective activity. The strong updrafts of the convective cells evidently lofted ice and snow particles high in the troposphere, where upper-level divergence spread them over a broad area, and a stratiform region subsequently developed in place of the earlier vigorous convection (Fig. 4.4b, d). In this stratiform phase, the snow particles settled, further increased in mass by vapor dep-

osition and collection of cloud ice, and finally melted and fell out as stratiform rain (Fig. 4.4d).

It should be kept in mind that the simulated system presented here is best thought of as being of a portion of an MCS, since the domain boundary is not able to circumscribe the entire MCS. This may be one reason that the simulated MCS has a markedly shorter life span than the convection observed on 14 December. The simulated convection lasts for <4 h, while a typical MCS lifetime determined by cloud top IR temperature criteria is 10 h (Houze 1993). However, the simulation does capture reasonably well the temporal transition from convective to stratiform visible in the observations (cf. Figures 4.3 and 4.4) on that day.

## 4.3 Trajectory analysis: parcel mode

As in the 23 December case, six hundred earth-relative trajectories were computed from the ARPS output. For the model time interval 1-5.5 h, trajectories were calculated every six seconds from model data that had been output every two minutes. The initial trajectory locations were inside a volume 20 km × 108 km in the horizontal dimension and 5.7 km in the vertical (twelve vertical levels of fifty points each). This region was the source of the storm's inflow air (Fig. 4.5). The lower level wind is mostly northerly at the beginning of the trajectory calculation. However, in the storm-relative sense the flow is easterly; the tracers enter the convective system on its east side.

Figure 4.6 shows a small sample of trajectories whose initial positions are aligned in a vertical column. Only tracers initially near the surface are prone to rise a significant distance. Tracers initially higher in the column sink or remain at the same level. This is a characteristic of the crossover zone conceptual model, even though the quasi-two-dimensional portrayal of the crossover zone in this simulation is sometimes difficult to identify. Since the vertical wind profiles exhibit significant directional and speed shear with height, the entire concept of layer can be twisted.

Figure 4.7 is similar to Fig. 3.5. It shows three different but related perspectives on the behavior of the ensemble of trajectories. Figure 4.7a shows the likelihood of a parcel

to ascend (solid line) or descend (dashed line) 500 m from its initial height. Trajectories initially near the surface are very likely to rise, but the percentage that rise drops off significantly with height, until at 2200 m, fewer than 3% rise more than 500 m above their initial height. For trajectories initially at the lowest vertical level (200-m height), 95% of the final locations are 500 m above the initial locations, and many of the final locations are at extremely high altitude. A significant number (19/50 = 38%) ascend to approximately 13 km.

Above 3000 m, the number of trajectories that descend more than 500 m from their original altitude increases significantly with height and peaks at 70% above 5200 m, though most of these only descend a kilometer or two. Inspection of the scatterplot (Fig. 4.7b) and the histograms (Fig. 4.7c) shows that few of these trajectories ascend through as deep a layer as do those with initial heights near the surface.

These statistics are largely consistent with the crossover zone of the conceptual model. The boundary layer air, characterized by large $\theta_e$, is most apt to rise, while the drier air lying just above is mostly entrained into the updrafts and downdrafts, becoming negatively buoyant and sinking. After being entrained into the convective region, the middle part of the layer achieves neutral buoyancy, and hence the tracers neither rise nor sink significantly. A few tracers initiating at levels above 3000 m rise. Zipser (1977) mentions the possibility that a small percentage of middle level ambient air might mix with a relatively large percentage of updraft air, causing some parcels of ambient air to rise. Although the tracers originating in the upper part of the layer sink, their descent appears to be less than what might be expected from the conceptual model, where the relatively dry, upper part of the layer enters the convective zone and helps initiate and enhance mesoscale unsaturated downdrafts. This process seems to be occurring only in a limited fashion in the model, though it should be noted that the low $\theta_e$ air at model midlevels is several degrees larger than that in the conceptual model (335.5 K in the simulation versus 332 K in the schematic diagram of the conceptual model from Zipser 1977). Thus, perhaps less strengthening of the downdrafts and less downward movement of the tracers might be expected given the model environmental conditions.

Changing the initial positions and times of the trajectories tested the validity of the trajectory statistics. Moving the initial tracer locations small amounts in the horizontal (1 km to the east and 1 km to the north of the control case locations) results in some large changes in final locations, both horizontally and vertically; however, the ensemble properties of the trajectories remain virtually unchanged. The trajectories are somewhat sensitive to the initial calculation time. Keeping in mind that the interest is to release the trajectories in the system inflow, some care is needed in choosing the initial time. Beginning too early means the tracers reach the convective region before it has had a chance to fully form and spin-up; beginning too late means the tracers never reach the convection but rather head to the south and subsequently to the east. The trajectory statistics are quite similar for initial calculation times between 1and 1.5 h.

## 4.4 Cellularity in the temperature field

Redelsperger and Lafore (1988) suggest that the crossover of different air masses (which occurs between 1.5 and 5 km in their model) involves pockets of high and low $\theta_e$ having similar sizes. This process is particularly apparent in the strengthening stages of a convective system, especially when vigorous convective cells are spaced along a cold pool, as is the case for the 14 December simulation. Figure 4.8 indicates the presence of these convective scale pockets of temperature perturbation. As for the pressure perturbation, formulating temperature perturbation can be problematic for initial conditions that are horizontally inhomogeneous. It is here calculated as a deviation from the horizontal mean at the initial time. Although the initialization is horizontally inhomogeneous, the initial perturbations at 3 km were only ~0.5 K, with most of the domain occupied by values much smaller, and a representative profile taken from the pre-storm environment is virtually identical to the horizontal mean profile taken at the initial time. At an altitude of 3 km, a line of negative temperature perturbation (dashed) ahead of the convection in the northern part of the domain indicates a portion of the leading edge of the spreading cold pool (Fig. 4.8a), though not the cold pool itself. Although this line is continuous, local

maxima associated with individual convective cells are present, as are local minima located to the west.

Figure 4.8b shows that after 3 h the edge of the cold pool and a region of shallow convection has propagated 30 km ahead of the active region in the northern part of the domain. With the negative temperature perturbation resulting from the cold pool located a significant distance east of the convection, individual convective cells and their associated temperature perturbations are more visible. By this point in the simulation, the convective region has already begun to weaken. This time appears to be a transition between convective and stratiform regimes. By 4 h (Fig. 4.8c), the cold pool boundary has nearly reached the east edge of the model domain. The interior solution, previously dominated by convective scale cells, has been replaced by a mesoscale region of generally cool air associated with the organized stratiform precipitation visible in the derived radar imagery.

## 4.5 The nature of observed inflow on 14-15 December 1992

Although the trajectory calculations indicate that the crossover conceptual model seems appropriate for the simulated convection of the control run, radar observations on this day contain evidence of a deep layer of inflow, the whole of which appears to rise upon entering the convective system (Fig. 4.9). The system observed by aircraft between 1630 and 1830 UTC has sloping layer inflow from the west, while the relative inflow produced by the model is shown by the trajectories to be largely from the east. This behavior of the model is not really at odds with the observations. Chen et al. (1996) applied a tracking algorithm to infrared satellite imagery to show the long-term movement of large tropical cloud clusters. Figure 4.10 shows a bifurcating propagation in which the 14 December cloud system splits into eastward and westward propagating systems (Box A). In addition, a significant eastward propagating system occurred on 15 December (Box B). These opposing movements in the satellite observations suggest that the same system had portions of convection with different inflow directions. The direction of propagation is determined largely by the ambient low-level shear (Rotunno et al. 1988), though observations indicate it can also be affected by vertical transports of momentum (Houze et al. 2000).

Houze et al. suggest that in the westerly onset region, the large-scale shear favors midlevel easterly inflow in the early stages of convection. They suggest that a mature mesoscale convective system with a significant region of stratiform descent is able to transport midlevel easterly momentum downward, favoring new convection on the west side of the MCS, which is characterized by low-level westerly inflow (see their Fig. 25). In their analysis of aircraft dual-Doppler radar data collected on 14 December, Kingsmill and Houze (1999a) found multiple storm-relative inflow directions in three different regions of convection on 14 December (see their Table 4). Figure 4.11 shows a region where the inflow was easterly. This piece of convection, sampled by the aircraft from 1700 to 1715 UTC, was south of the region shown in Fig. 4.9 and was likely at an earlier stage in its life cycle. The easterly inflow that appears in the model seems more consistent with this portion of the convection.

## 4.6 Processes determining parcel or layer inflow

As noted in the previous section, the midlevels were drier in the initial conditions used to represent 14 December than in the 23 December case. This section describes a numerical experiment designed to isolate the effect on the inflow of the midlevel environmental moisture. I perform a sensitivity test on the 14 December case by increasing the midlevel moisture in the initial conditions of the model run.

### 4.6.1 Enhanced moisture experiment

The radar data in Figs. 4.9 and 4.11 show deep layers of inflow, in contradiction to the model results, which suggest a parcel lifting scenario — the only air reaching high levels being parcels originating from near the ocean surface. The observational evidence suggests that this parcel lifting occurs in the model because of the dry midlevels in the model input data. Figure 4.12 shows thermodynamic profiles taken in the inflow region of the simulated MCSs. Midlevels of the 23 December experiment, in which the layer inflow mode was present, are significantly moister by comparison. The goal of our sensitivity experiment was to test whether the parcel lifting in the 14 December simulation would be replaced by a layer-type inflow if the midlevels were moistened. The experiment makes

no assumptions about the mechanism that causes the moistening, although some possible mechanisms will be discussed below.

For the sensitivity experiment, the relative humidity was set to 95% for all points in the domain between 1700 and 6000 m altitude. The new mean inflow profile is plotted on Figure 4.12. Rationale for this choice is that Kingsmill and Houze (1999b) found that the depth and breadth of the convection, and hence its degree of organization on the mesoscale, to have been correlated with the humidity of air entrained into the system at low to middle levels. The moistening is therefore reasonable, even if the exact mechanism or mechanisms are not understood.

The simulated radar reflectivities in Fig. 4.13 compared with those in Fig. 4.3 provide an overview of the sensitivity experiment. Adding midlevel moisture results in convection that is horizontally more extensive than that in the control simulation. It has a more extensive stratiform region, and the convection cells are stronger. The temporal development of the two runs is quite different. In the enhanced moisture experiment, the convective region is maintained longer, and the stratiform region develops earlier. New convective cells form behind (to the west of) the leading line but are unable to maintain their intensity, transitioning rapidly into small but numerous regions of stratiform precipitation that subsequently aggregate in time (Houze 1997). In contrast to the control case, new convective elements are triggered at the edge of the cold pool. According to the reasoning of Rotunno et al. (1988), the slightly deeper (though weaker) front edge of the cold pool in the enhanced moisture experiment produces a more ideal balance between vorticity generated by the cold pool and that present in the ambient flow. For these reasons the convective system in the sensitivity experiment exhibits a better-defined spatial pattern of convective and stratiform structure, where both elements are present together for a longer period of time, and the system more slowly evolves to its dissipative stage. An additional reason for the slower evolution may be that the increase in midlevel humidity modulates the intensity of the cold pool. Early in the life of the system, when convective cells dominate, the cold pool temperature perturbation for the control case is -4 K, while for the sensitivity case it is only -2 K. The enhanced humidity leaves less potential for evaporation

of rain and melted ice particles. The cooling in the sensitivity experiment results more from melting of ice particles than from evaporative processes. In the control case, evaporation is dominant for the early-to-mid stages of the system, but eventually the evaporation from falling hydrometeors nearly saturates the middle levels.

In addition to greater spatial extent, the convection in the sensitivity experiment is more intense, having stronger updrafts and downdrafts than the control results. A moister environment producing more intense convection is in agreement with Lucas et al. (2000), although both control and sensitivity results in the present study seem to be more intense than in the Lucas et al. corresponding experiments. The reason for this difference is not immediately clear, though the difference in initialization methods is the moist logical possibility, since the microphysical and sub-grid schemes are quite similar. Lucas et al. (2000) conclude that the stronger updrafts in the enhanced moisture case result from decreased dilution via entrainment of midlevel environmental air. This seems to be the case for the enhanced moisture experiment in this study, too, although the results do not (for the reasons stated above, regarding saturation deficit) appear to extend to the cold pool magnitude.

### 4.6.2 Trajectory analysis of the enhanced moisture experiment

Trajectories were calculated for the sensitivity experiment using the same initial block of points. The number and initial tracer locations are the same as for the control case, and trajectories computed from a single column of initial points are shown in Fig. 4.14. Whereas for the control case (Fig. 4.6) only tracers in the lowest few hundred meters ascend, tracers in this case show more of a tendency to ascend a significant distance. Only a few of the tracers represent air being entrained into the downdraft, becoming negatively buoyant and sinking. As in the control case, the final tracer horizontal locations can be significant distances from each other.

Figure 4.15 shows the statistical behavior of the ensemble of trajectories for the sensitivity run. As for the control case (Fig. 4.7), the tracers initially near the surface are very likely to rise. The depth for which 95% rise more than 500 m above their initial level is 1700 m. Above 1700 m, the percentage that rises decreases but less so than for the con-

trol case. In the control run, only 3% of the tracers with initial altitudes of 2200 m ascend more than 500 m, while nearly 75% do so in the environment with enhanced midlevel moisture. For points beginning at 4700 m, nearly 40% ascend, and the scatterplot (Fig. 4.15b) and distribution (Fig. 4.15c; $z_0 = 4700$ m) show that, unlike for the control experiment (Fig. 4.7c), a significant number of these trajectories extend a significant distance upwards.

The percentage of tracers at upper levels of the inflow layer that descend more than 500 m are similar for both experiments, and the scatterplot and histograms reveal that the descent is in general greater for the case with the enhanced moisture. This initially seems wrong from a parcel-mixing perspective, because dry midlevel air entering a system and mixing with a saturated downdraft would tend to cool the downdraft via evaporation. However, results from numerical experiments investigating microbursts (Srivastava 1985) show that a moist middle level in the environment humidity profile can actually enhance the strength of some downdrafts (and hence, the tendency for the tracers to descend farther), since the contribution of the moisture perturbation in the buoyancy term becomes more negative as the base state mixing ratio increases. Most likely, the peculiar relative behavior of the descending tracers in the two experiments may arise from the lack of robust, mesoscale unsaturated downdrafts in the control simulation and the overall slightly stronger nature of the convection (and downdrafts) in the sensitivity run. In addition, the timescale of the simulated convection is shorter than in nature, and it is unlikely that the weaker downdrafts in the control simulation are able to fully form over the relatively short duration of the simulation.

### 4.6.3 Thermodynamic differences between the model experiments

The control experiment profile in Figure 4.12 is similar to the "fair weather" category described by Lucas and Zipser (2000), with a dry midlevel $\theta_e$ of ~335 K and characterized by isolated showers and small MCSs. The profile from the sensitivity experiment is more similar to Lucas and Zipser's (2000) active category, which has a midlevel $\theta_e$ of ~340 K and is accompanied in the model by extensive deep convection and layer inflow,

as demonstrated by trajectory analysis. The profile from the 23 December experiment is even moister and also exhibits layer inflow.

Horizontal cross sections of $\theta_e$ along the direction of the storm-relative inflow show significant thermodynamic differences between the control and the enhanced midlevel moisture experiments. The cross section in Fig. 4.16a of the control experiment at 3 h shows a pattern strikingly similar to results from Fovell and Ogura (1988) and strongly indicative of crossover flow. The inflow at low levels (from right to left) is plainly evident, as is the midlevel $\theta_e$ deficit at a height of 4 km. At low levels, the air flows along lines of constant $\theta_e$, but when the inflow encounters the cold pool and begins to rise, it begins to cross isopleths of $\theta_e$. This thermodynamic pattern, where $\theta_e$ is not conserved in the front-to-rear flow, is a strong characteristic of the crossover zone. In addition, this region of flow normal to the $\theta_e$ isopleths is associated in the model with a strong positive correlation of vertical velocity and $\theta_e$, another strong indication of crossover zone "mixing."

A similar cross section through the enhanced moisture domain shows significant differences (Fig. 4.16b). The $\theta_e$ isopleths indicate that the thermodynamic character of the inflow channel is rather well maintained as it rises above the cold pool. Vertical velocity and $\theta_e$ are correlated as in the control case, which indicates that overturning of the environment is still taking place. It appears, though, that whereas the form of the overturning in the control experiment is a typical crossover zone, the physical manifestation of the overturning in the enhanced moisture case is a deep layer inflow.

Bryan and Fritsch (2000) observed layer inflows into midlatitude MCSs and conceived of a thermodynamic state that could explain the long-term existence of this absolutely unstable state. They use the term "MAUL" (moist absolutely unstable layer) to indicate a saturated layer in which the lapse rate is greater than the saturated lapse rate. They applied these conditions to rawinsonde and model data to show that MAUL regions were well correlated with deep layer inflow. The gray regions in Fig. 4.16 are zones where the environment was analyzed to satisfy MAUL criteria. The size of the MAUL in the enhanced moisture case is significantly larger than that in the control case, which

exhibits MAUL conditions near cloud base only. The large MAUL region in the enhanced moisture experiment lies near the center of the inflow channel and is very similar in size and shape to those found by Bryan and Fritsch. Although not shown, the cross section for the 23 December case resembles the 14 December enhanced moisture case, including a deep ascending inflow channel and a significant MAUL. Figure 4.17 shows time-height cross-sections for the three cases to indicate a lower bound on the lifetime of the simulated MAUL. For the layer mode cases, the structure and timescale are also similar to those in Bryan and Fritsch, with MAUL conditions typically lasting between 20 and 40 minutes at fixed locations. Figure 4.17c bears a particularly close resemblance to Figure 17 in Bryan and Fritsch (2000).

### 4.6.4 Possible mechanisms that could bring about the layer mode

The experiments have shown a tendency for layer overturning, as identified by trajectory analysis, to be correlated with midlevel environmental humidity. Three possible mechanisms that might bring about the layer mode of MCS inflow are suggested: two speculative external factors pertaining to the creation of enhanced midlevel humidity and one factor internal to the simulated MCS arising from enhanced moisture.

Moistening and cooling of the upper part of a subsaturated environmental inflow layer would reduce the static stability of the inflowing layer of air, enabling the gust front to produce more lifting for a given amount of work. The closer to saturation the air becomes, the more immediately relevant the value of moist static stability. When a layer of air is near saturated and moist neutral it is easily lifted by a cold pool. The question arises how the inflow layer could become nearly saturated and moist neutral in the case of convection over the warm pool. Two possibilities are suggested.

One proposed mechanism that could produce a moistened lower tropospheric layer with a moist adiabatic lapse rate is mixing by cumulus congestus or cumulonimbus of moderate depth. Johnson et al. (1999) and Mapes (2001) present evidence from TOGA COARE that vertical mixing by such clouds has a measurable impact on the large-scale thermodynamic stratification of the atmosphere over the warm pool. If the layer of air approaching an organized MCS passes through a field of moderate convection, the humid-

ity of the layer would be raised by upward eddy transport of humidity from near the ocean surface. In addition, moderate convection would homogenize the $\theta_e$ in the inflow layer, though the time scale for shallow cumulus overturning is O(12 h).

A second method for producing a nearly saturated moist neutral inflow layer is more complicated but plausible. The inflow layer might moisten by passing through a preexisting region of stratiform precipitation such as in Figure 4.18. Figure 4.19 shows another example of probable inflow layer moistening from Houze and Rappaport (1984), who described a tropical oceanic mesoscale convective system in which the inflow to the convective region passed under a precipitating portion of the anvil of the system. Thus, the cloud system itself modified the environmental inflow. It is also conceivable that the environmental inflow could pass under the precipitating anvils of other mesoscale systems in the neighborhood of the MCS in question. As the warm pool becomes populated by numerous mesoscale cloud systems during the westerly onset and westerly wind burst periods, this scenario becomes more likely. Moistening and cooling by precipitation particles falling from an anvil into the upper part of a subsaturated inflow layer would reduce the static stability of the inflowing layer of air. Melting and evaporation of the precipitation particles would cool and moisten the layer of inflow air. Subsidence below the anvil cloud base would largely compensate the evaporative cooling, so the net effect on the dry static stability could be quite small. This mechanism by itself would leave $\theta_e$ unchanged.

Since tropical oceanic convection typically exists in log-normal populations in which a few large precipitating cloud systems are accompanied by numerous middle-sized and small convective clouds (López 1976, 1977, Houze and Cheng 1977, and others), it seems plausible that the two mechanisms for moistening the environment could work in concert.

The model pressure perturbation and momentum fields suggest another aspect of the effect of the moistened inflow layer on whether layer or parcel lifting occurs. This process is internal to the mesoscale convective system. Perturbation pressure is calculated relative to the horizontal mean at the initial time. This is reasonable, since the initial horizontal variability is much less than that later in the simulation. System-relative u-velocity

is calculated by subtracting the propagation speed from the total u-field. Weaker evaporative cooling in the cases of high midlevel humidity is evident in the perturbation pressure field, which appears to modulate in some manner the slope of the inflow layer. The slope of the inflow for the 14 December sensitivity experiment is 3-4°, a value in excellent agreement with the system observed on that day (Kingsmill and Houze 1999a), while the slope is steeper in the control case. The amount of evaporation affects the strength of the cold pool, as reflected in the pressure perturbation field. The positive perturbation associated with the cold pool is both more intense and deeper in the control case where more evaporation occurs (Figure 4.20). The pressure gradient associated with the cold pool at the surface and with the hydrostatic low above the cold pool is associated with the sloping descending rear inflow regions visible in the plots of zonal velocity. A deep layer of air entering the system in the enhanced moisture run appears to be rising whereas for the control case, inflow air attempts to ascend but seems partially blocked by the system rear inflow that steeply descends. The plots of storm-relative zonal velocity may not be completely reliable as indicators of whether inflow obeys the parcel or layer flow models, but the plots qualitatively agree with the trajectory calculations in showing that increasing the midlevel relative humidity tends to have a significant impact of the character of the inflow. Because of the relationship between pressure (i.e. buoyancy) and momentum, a detailed forcing analysis would have to be performed to determine the root cause of the airflow slope. The implication of the more gradually sloping cold pool is that the mesoscale circulation takes on a greater share of the overturning of the atmosphere when the midlevel environment is moistened. That is, the conversion of potential energy by the layer lifting that is made possible when the environment is moistened may be a more efficient mechanism than isolated parcel lifting for overturning the tropical atmosphere over large spatial regions.

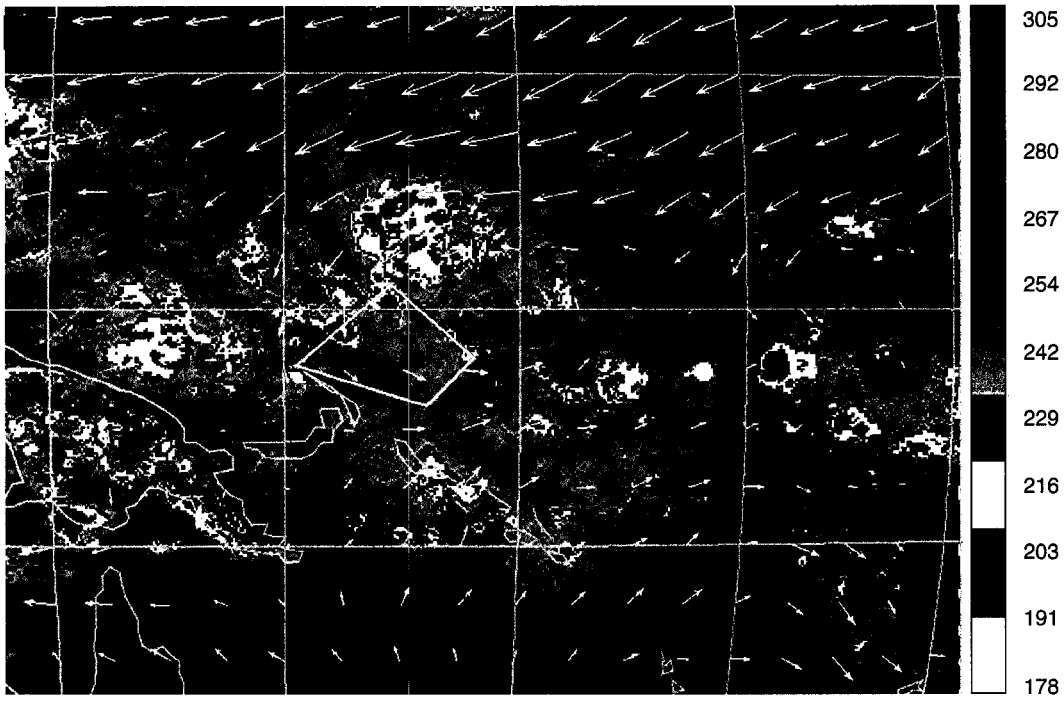


Figure 4.1. GMS IR imagery and 850 mb ECMWF winds at 0800 UTC 14 December 1992. The magenta box encloses the TOGA COARE intensive flux array (IFA). Wind vectors are plotted every 2.5° and are scaled such that a 20 m $s^{-1}$ wind is represented by a vector that would be 2.5° in length on the map at the equator.

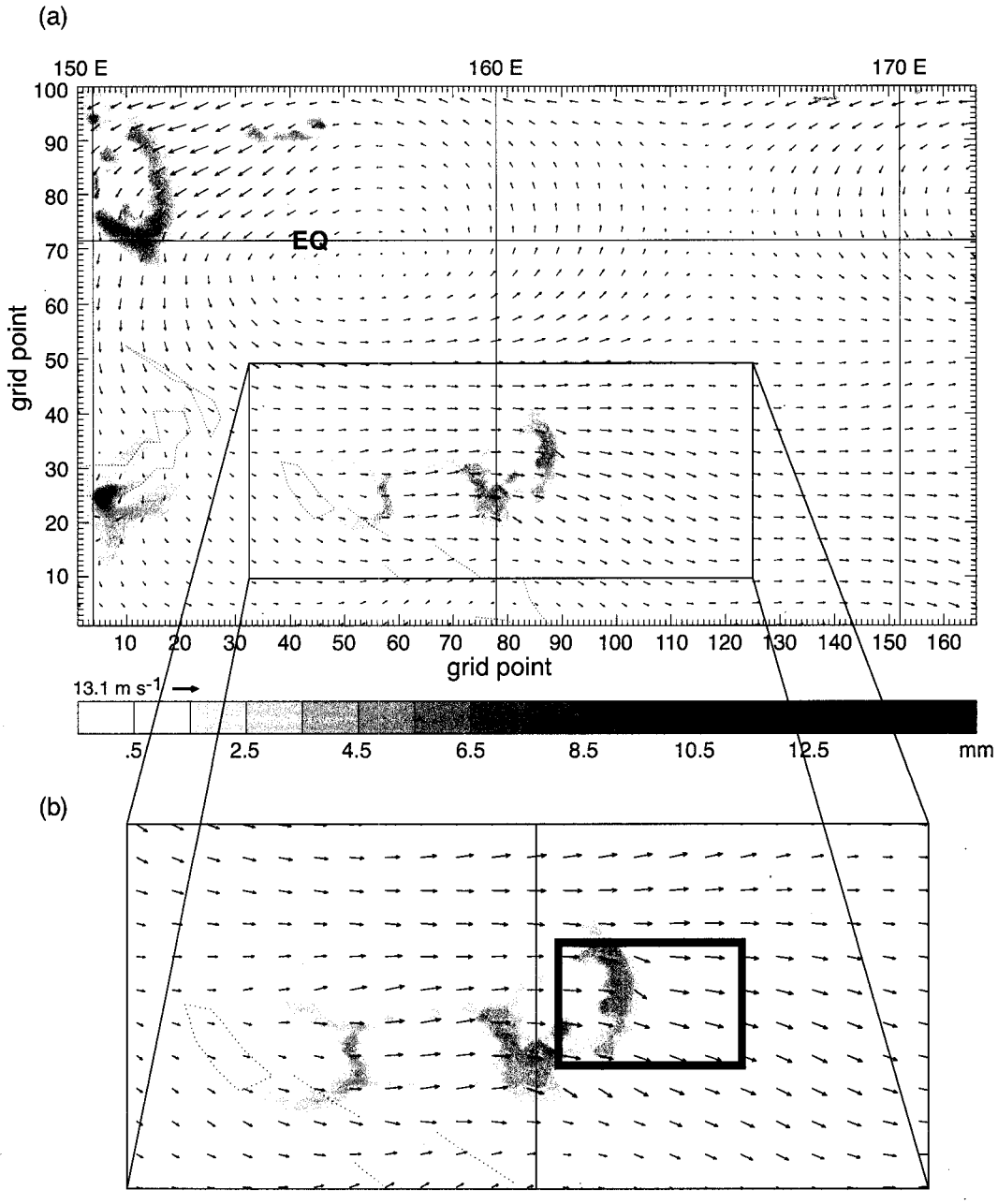


Figure 4.2. (a) 0800 UTC 14 December 1992 horizontal cross section of 850 mb wind and hourly accumulated surface rainfall from the 15 km grid of the MM5 simulation. (b) Magnification of the north-east region of (a). The ARPS (see text) model domain is enclosed by the rectangle centered at 5.4 °N, 161.9 °E.

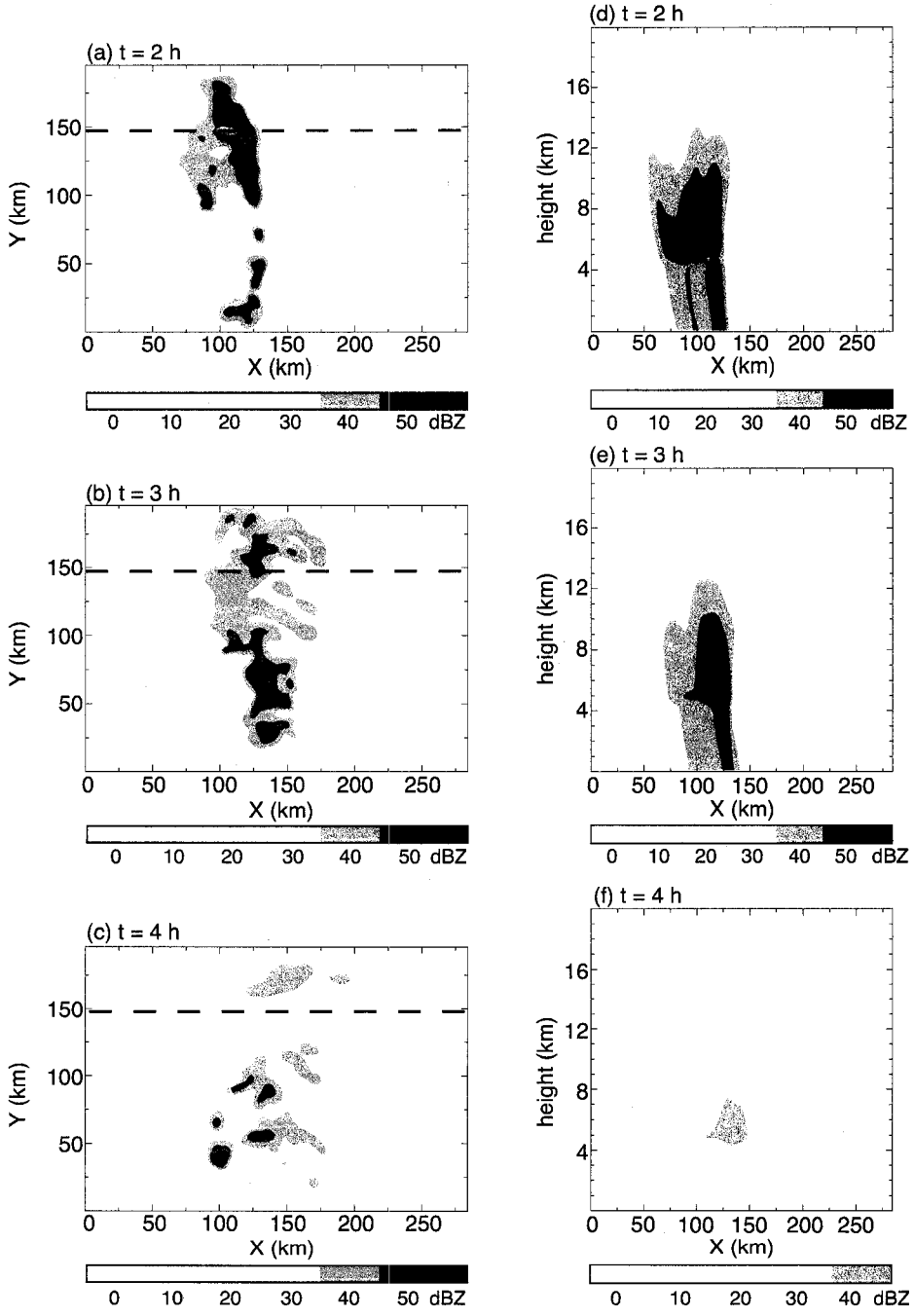


Figure 4.3. Model-derived radar reflectivity for the 14 December 1992 control experiment: (a)-(c) 1 km horizontal cross sections taken at hourly intervals and (d)-(f) vertical cross sections (indicated by dashed lines in (a)-(c)) taken through the northern part of the convective system.

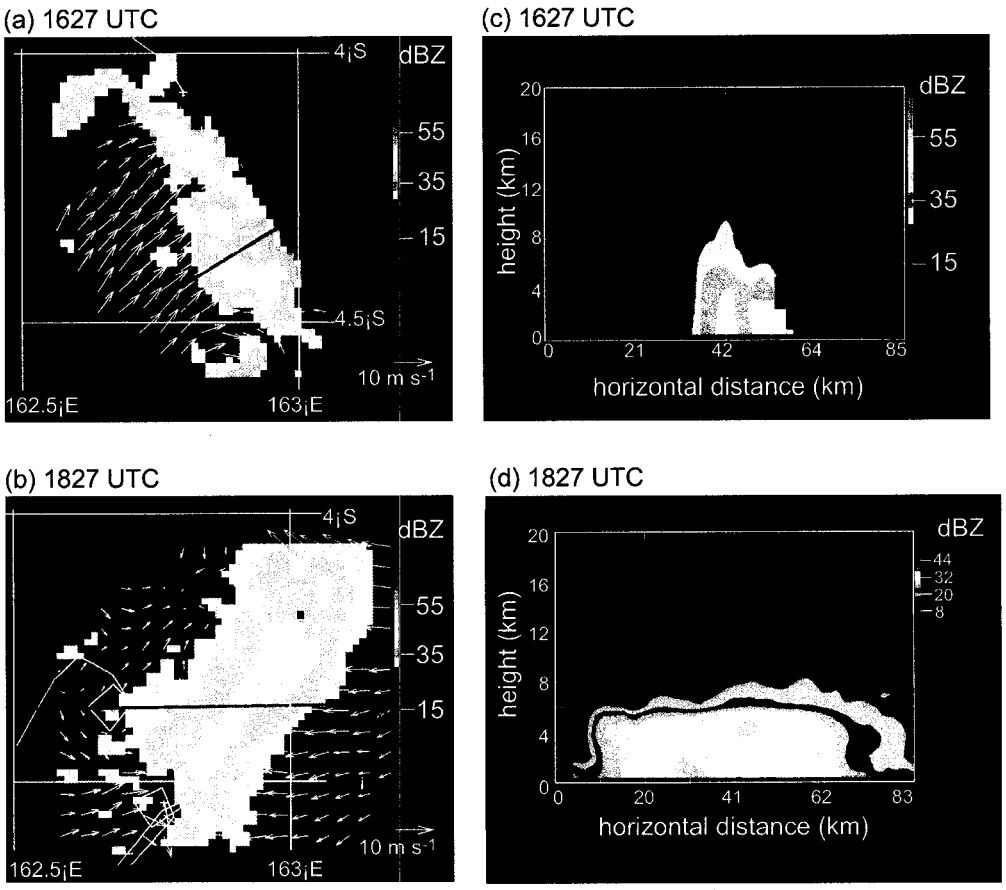


Figure 4.4. Airborne dual-Doppler radar data obtained by a NOAA P3 aircraft during the TOGA COARE field project on 14 December 1992 (flight track in yellow). Filled contours indicate radar reflectivity and superimposed vectors indicate the measured horizontal wind velocities. (a) and (b) are horizontal cross sections taken at 4.4 km above mean sea-level. (c) and (d) are vertical cross sections taken through the red lines in (a) and (b), respectively.

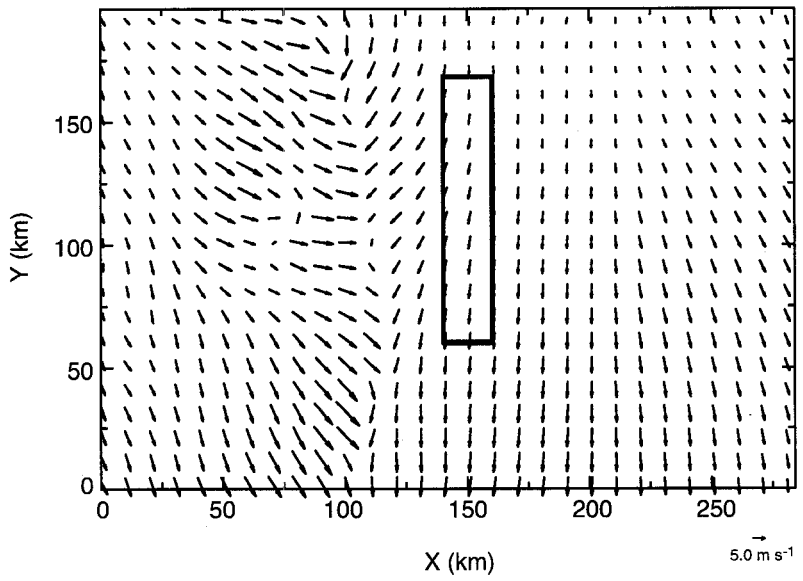


Figure 4.5. The horizontal span of the initial tracer distribution, indicated by the box and overlaid on the 1 h surface wind field.

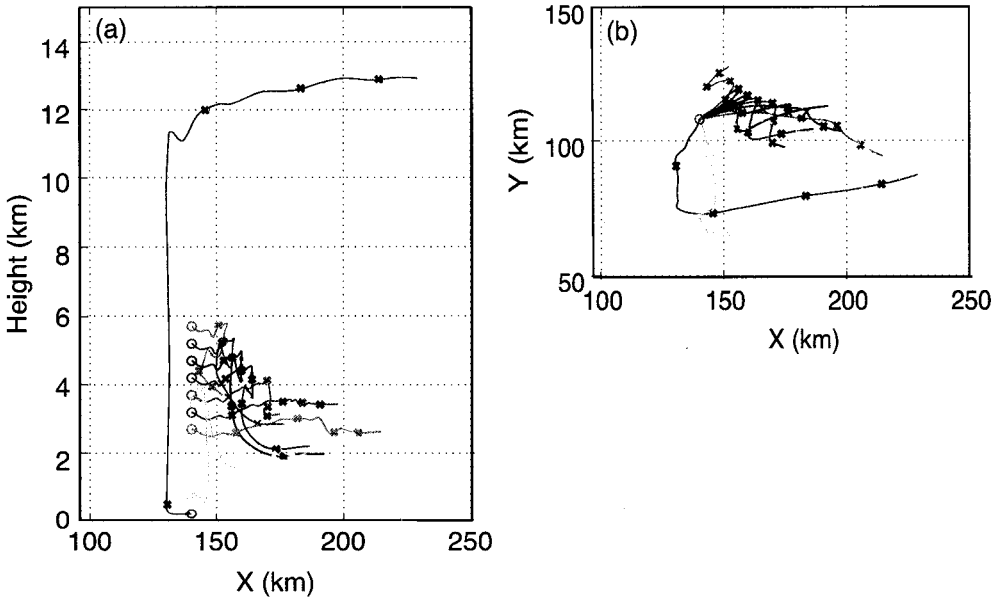


Figure 4.6. Two perspectives of 12 trajectories, each calculated over 4.5 hours of model time, for the 14 December 1992 control simulation. See Fig. 3.4 for explanation.

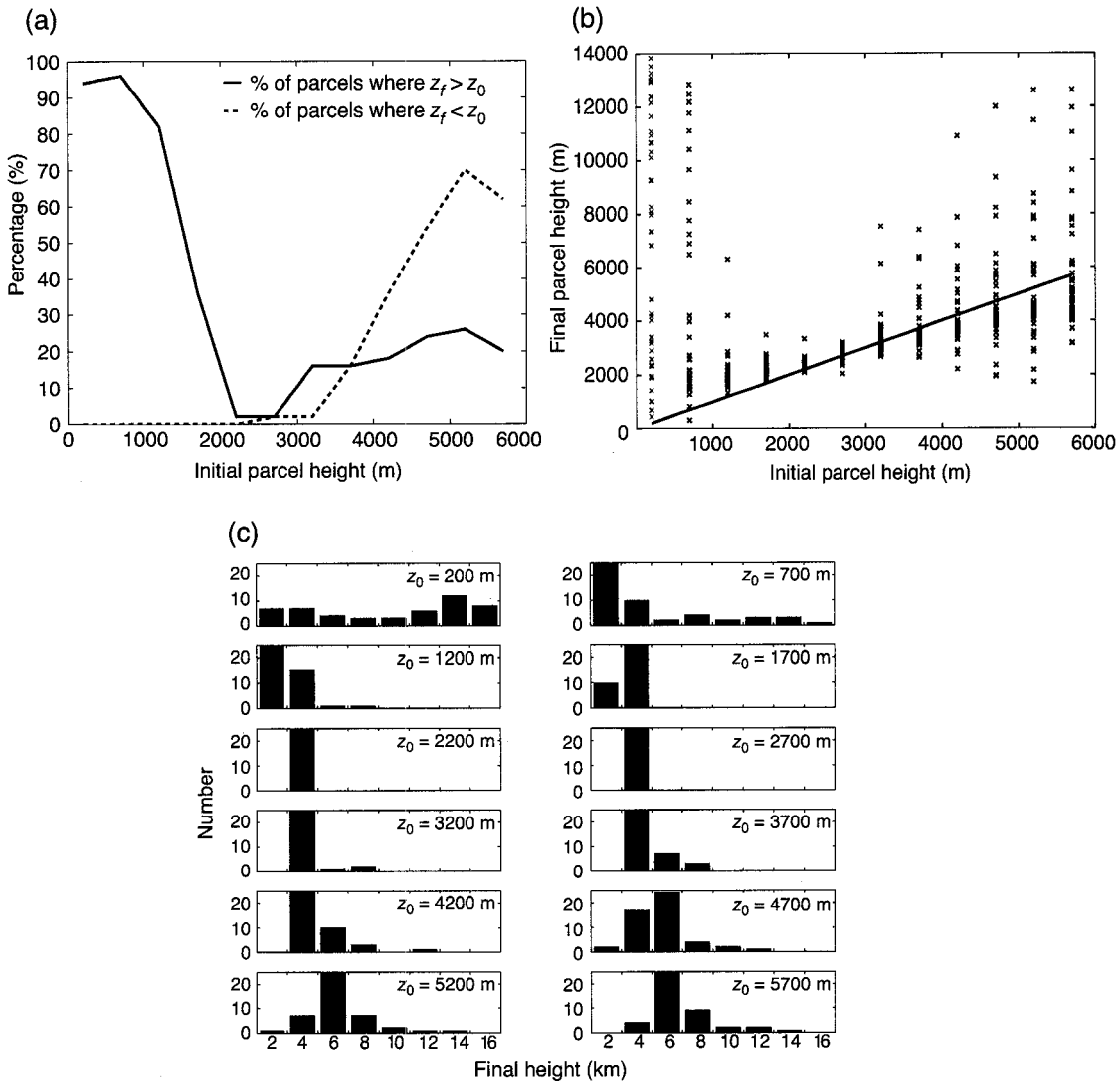


Figure 4.7. As in Figure 3.5 but for the 14 December 1992 control experiment.

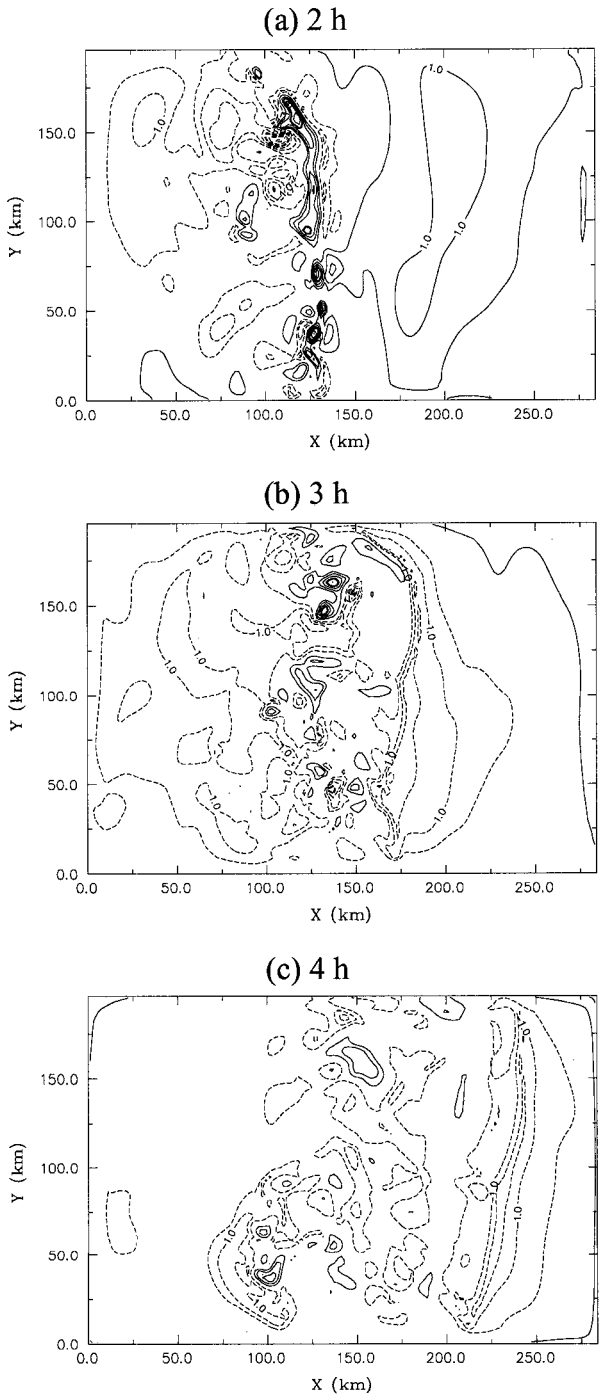


Figure 4.8. Horizontal cross sections of $\theta'$ taken at 3 km. Negative contours are dashed, and the contour interval is 0.5 K.

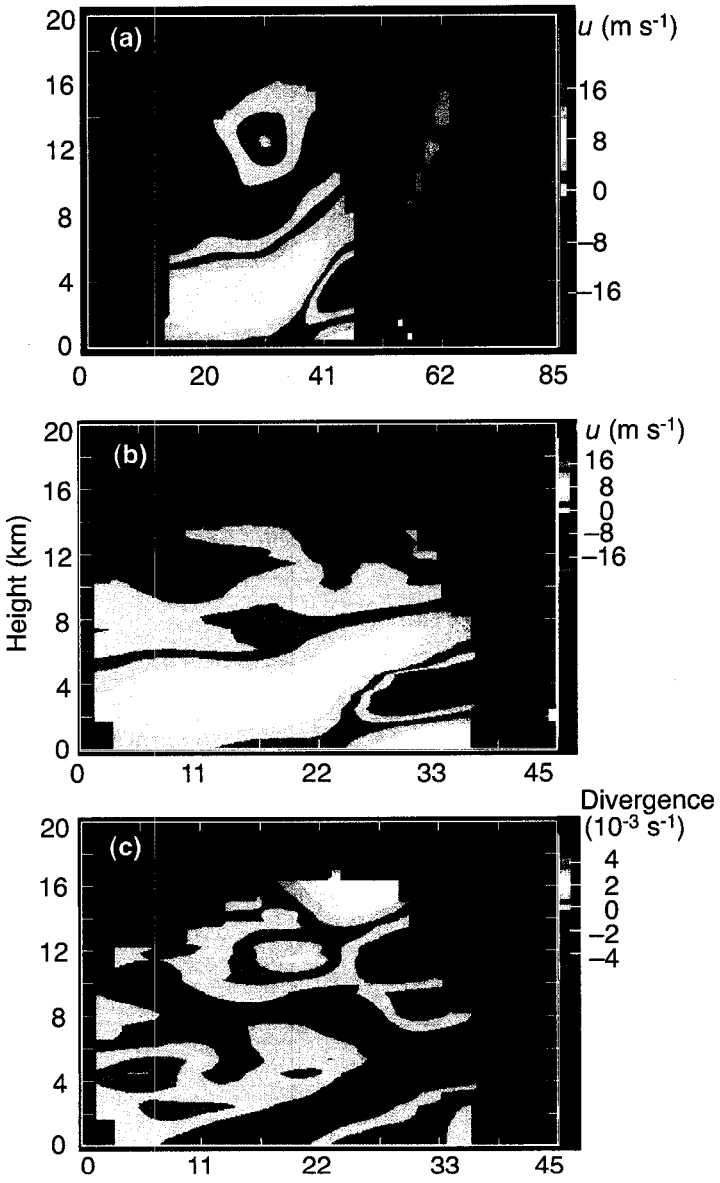


Figure 4.9. Airborne dual-Doppler analysis of part of a convective system observed on 14 December 1992. (a) Vertical cross section of u velocity at 1627 UTC taken along a line A-A′ in Figure 4.4. Yellows and browns indicate positive u; greens and blues correspond to negative u. Vertical cross sections of (b) u velocity and (c) horizontal divergence at 1635 UTC taken along a similar, shorter line while the system is still quite convective in nature. Regions of green indicate convergence; yellows and browns indicate divergence.

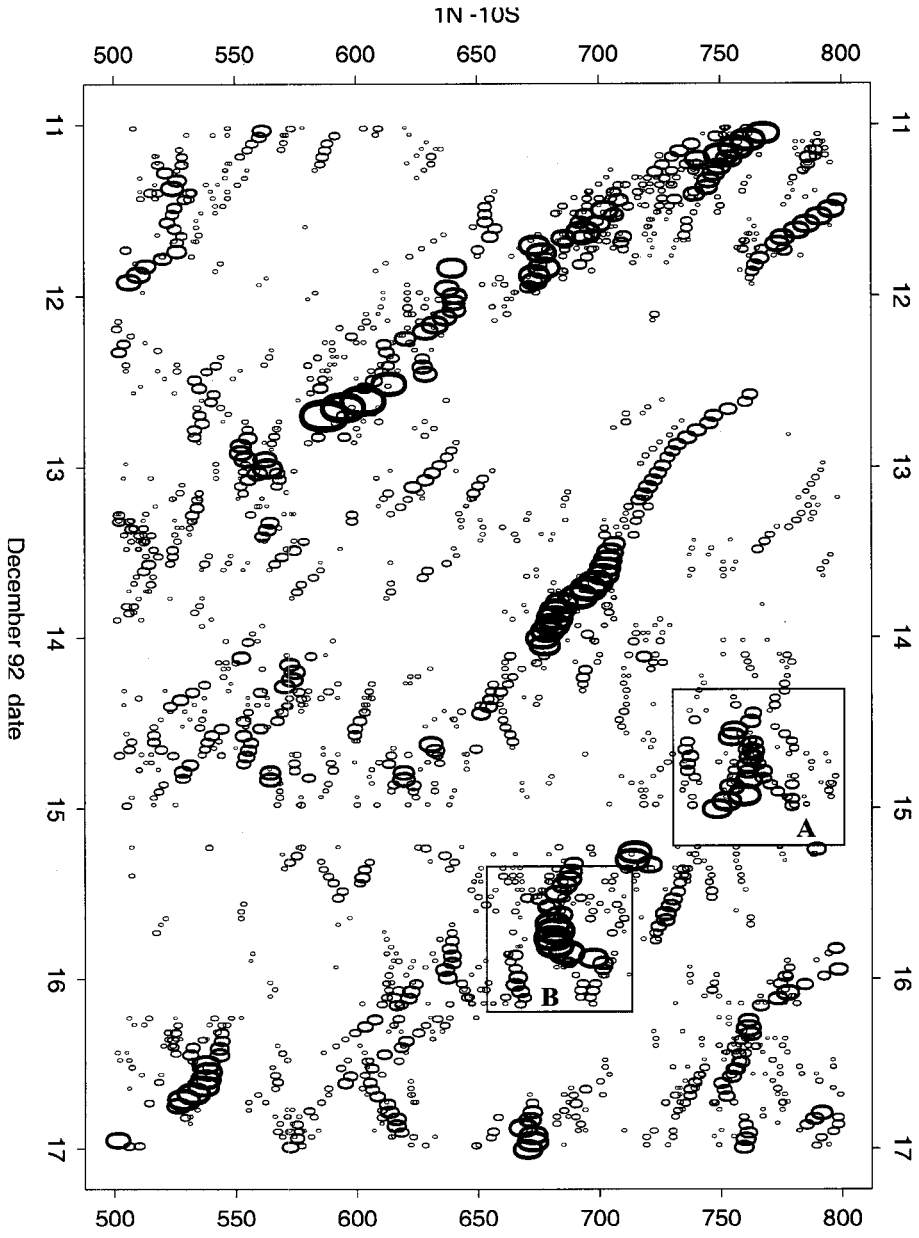


Figure 4.10. Time-longitude diagrams of cloud clusters colder than 208 K between 1 ° and 10 °S. Oval size is proportional to cloud cluster size. Rectangle A encloses simultaneous cloud clusters moving both east and west, and rectangle B shows a strong eastward-moving cluster (Adapted from Chen *et al.* 1996).

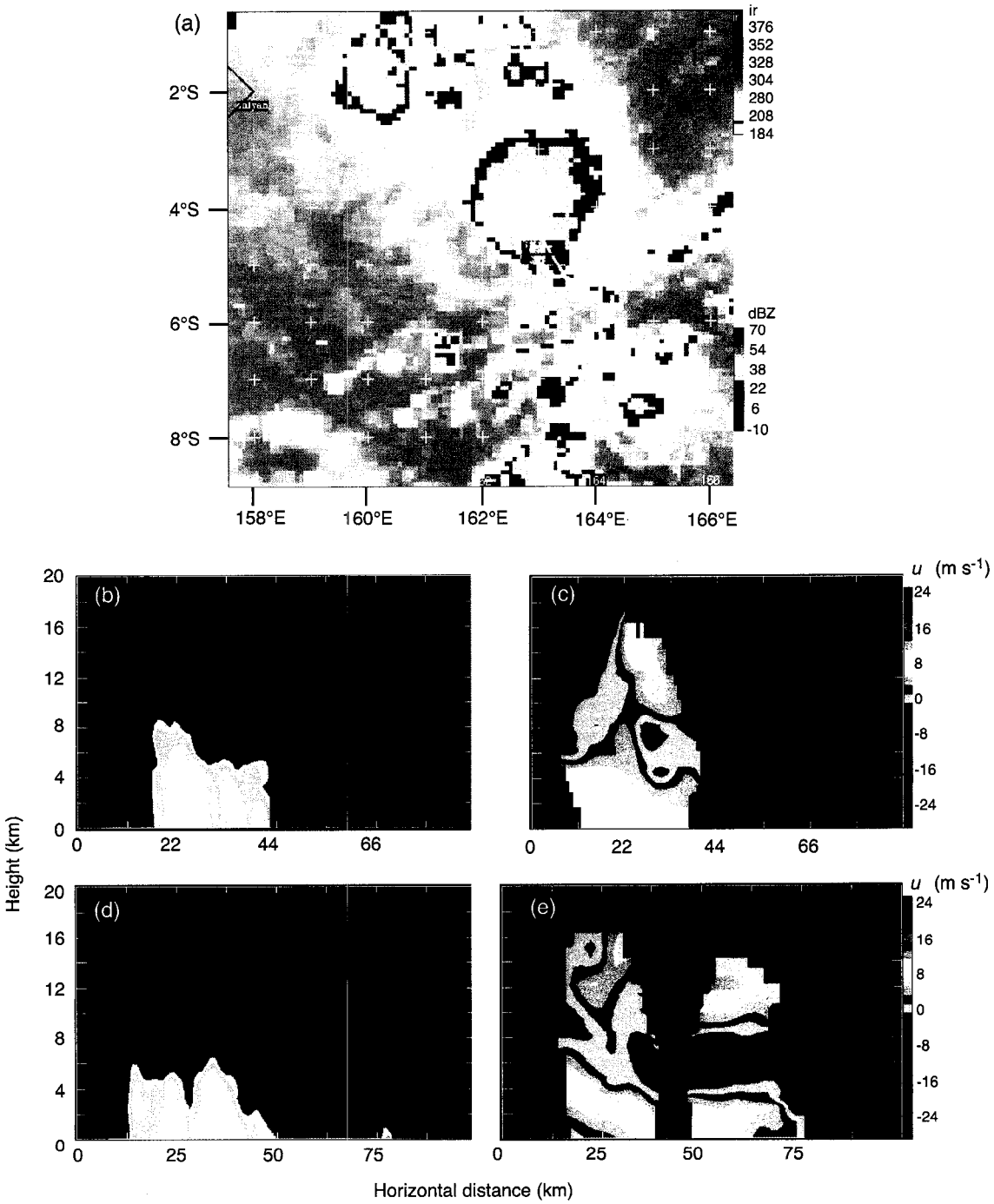


Figure 4.11. Airborne radar reflectivity and dual-Doppler analysis of the southern part of a large MCS for 1700 UTC on 14 December 1992. (a) Reflectivity overlaid on IR cloud temperature (K), and vertical cross sections of radar reflectivity and u velocity taken through predominantly west-east orientation at (b) and (c) 1700 UTC and (d) and (e) 1715 UTC, respectively.

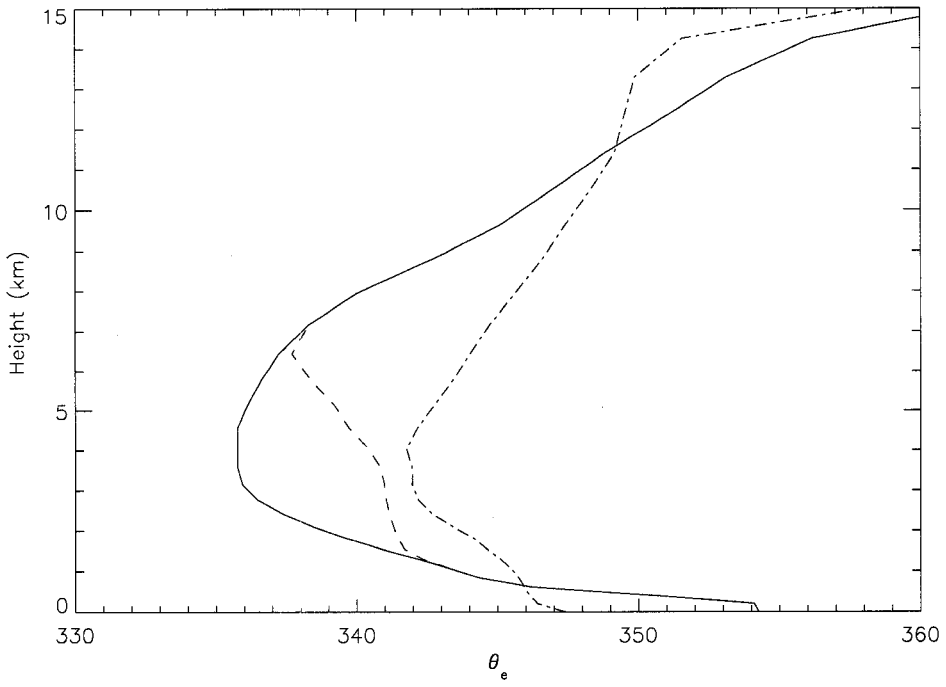


Figure 4.12. Representative equivalent potential temperature, $\theta_e$ (K), profiles in the inflow region of the simulated mesoscale convective systems for the 14 December control (solid line), the 14 December enhanced moisture (dashed line), and the 23-24 December (dash-dot line) experiments at the initial model times.

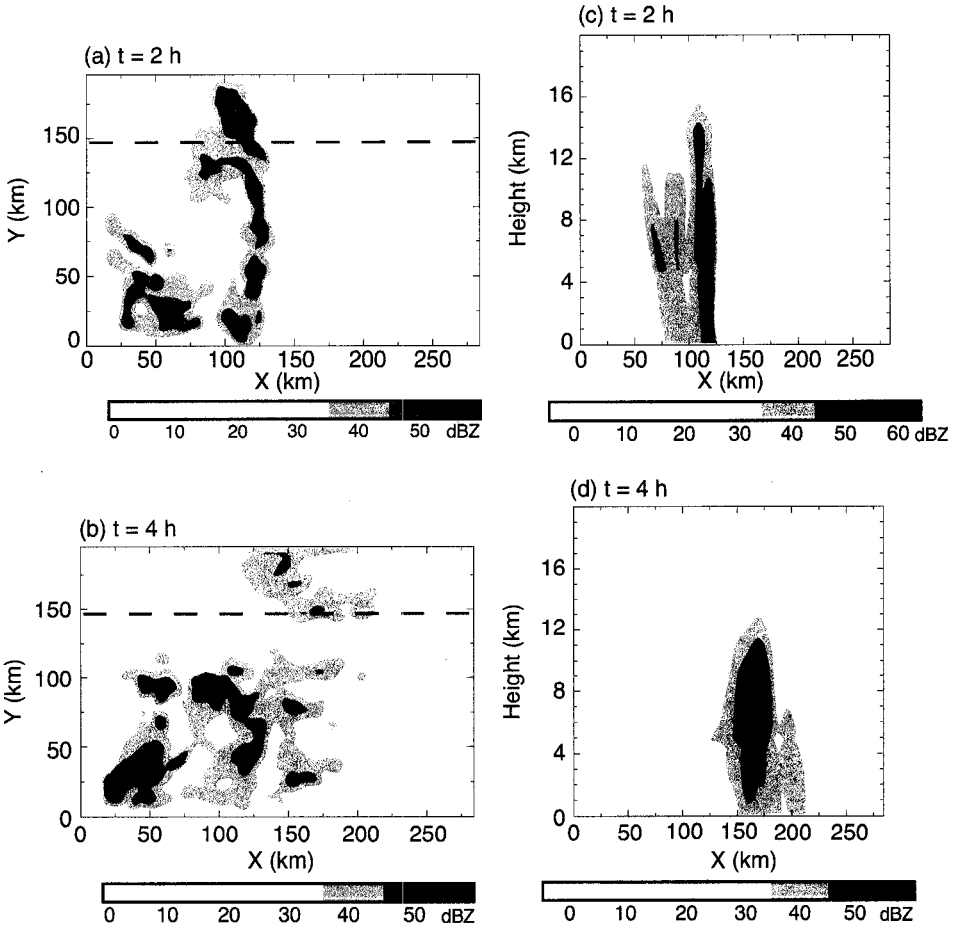


Figure 4.13. Model-derived radar reflectivity for the 14 December 1992 enhanced mid-level moisture experiment: (a) and (b) 1 km horizontal cross sections taken at 2 and 4 h and (c) and (d) vertical cross sections (indicated by the dashed lines in (a) and (b)) taken through the northern part of the convective system.

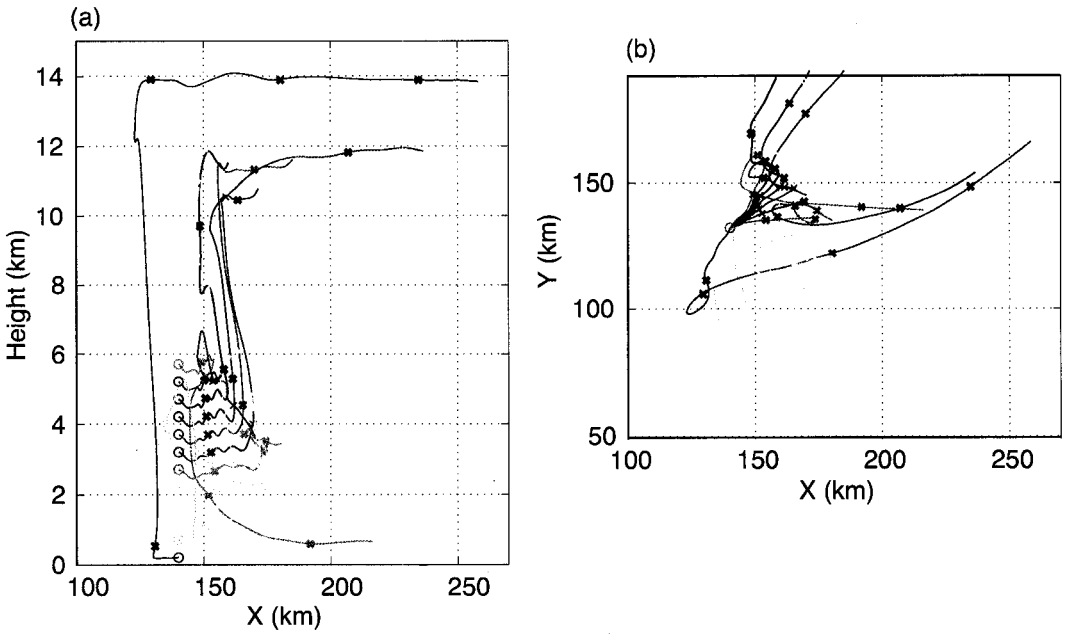


Figure 4.14. As in Fig. 3.4 but for the 14 December 1992 enhanced mid-level moisture experiment.

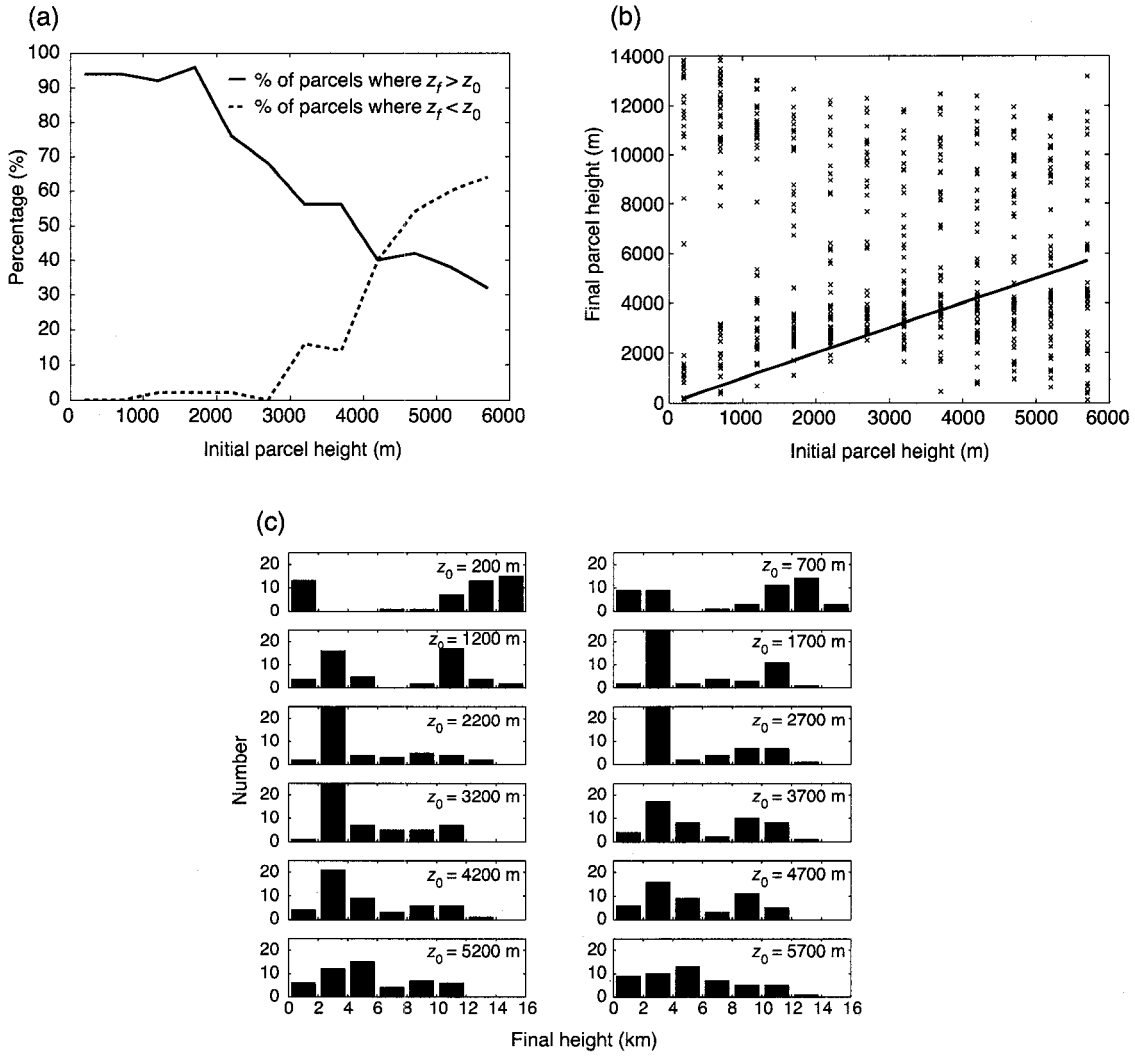


Figure 4.15. As in Figure 3.5 but for the 14 December 1992 enhanced mid-level moisture experiment.

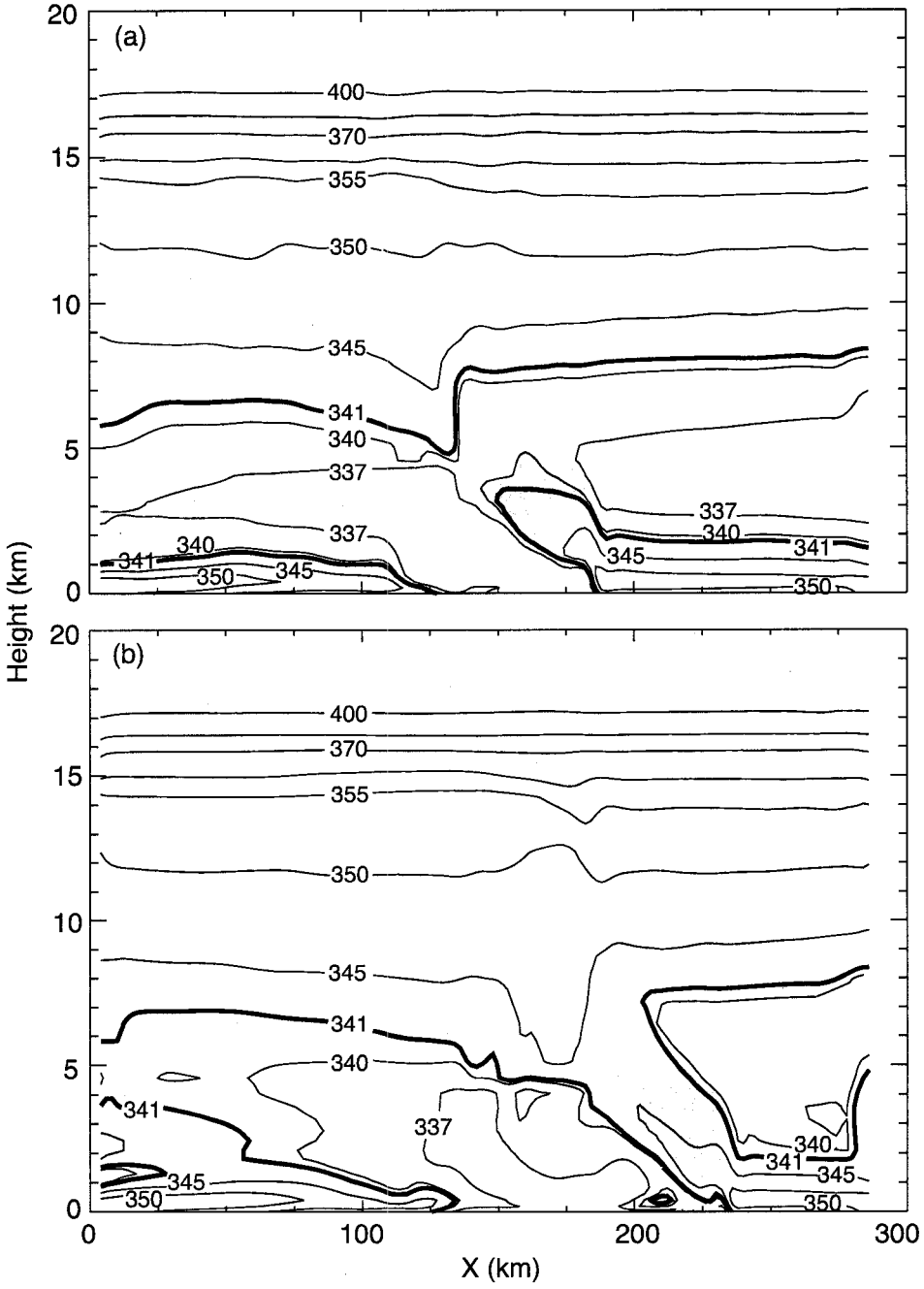


Figure 4.16. Vertical cross sections of equivalent potential temperature (K) taken through the lines indicated in Figures 4.3 and 4.13: (a) 14 December control experiment and (b) 14 December enhanced mid-level moisture experiment. Shaded regions are moist absolutely unstable layers, as defined by Bryan and Fritsch (2000).

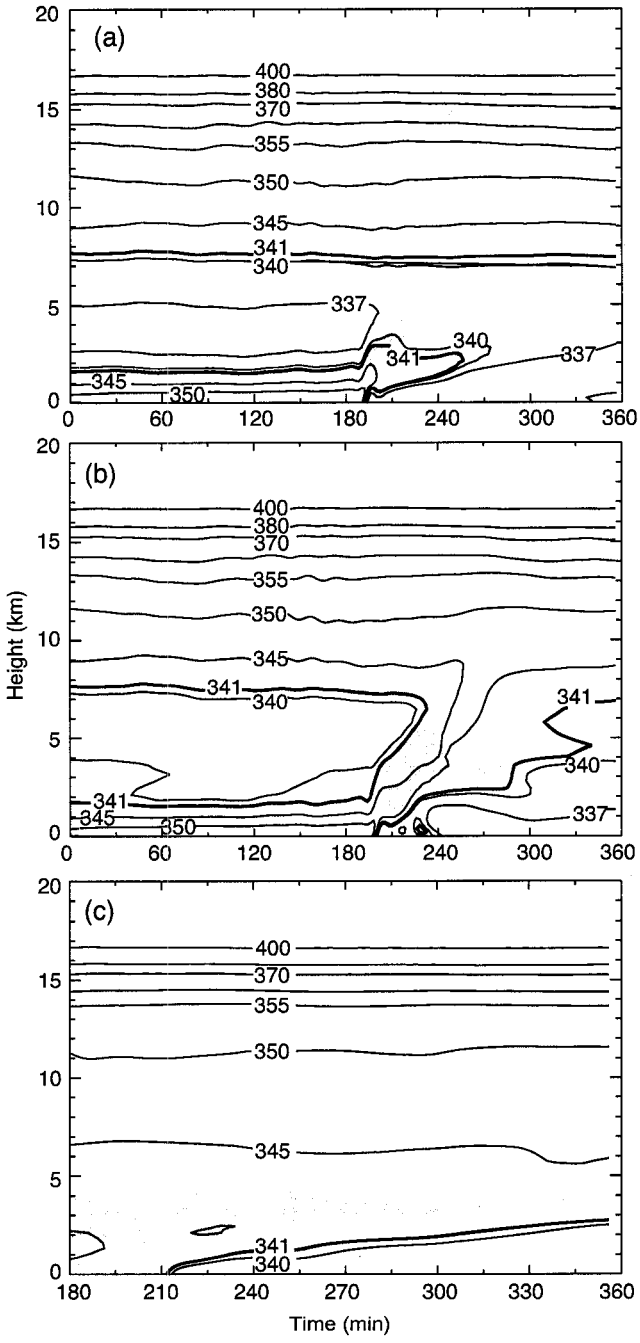


Figure 4.17. Time-height cross sections of equivalent potential temperature (K) from a location in the low-level inflow region: (a) 14 December control experiment and (b) 14 December enhanced-moisture experiment. The point chosen for the 14 December runs was located at x = 198 km, y = 148 km on Figures 4.3 and 4.13. (c) 23 December experiment, the point located at x = 148 km, y = 122 km on Fig. 3.3. Regions satisfying MAUL criteria (see text) are shaded.

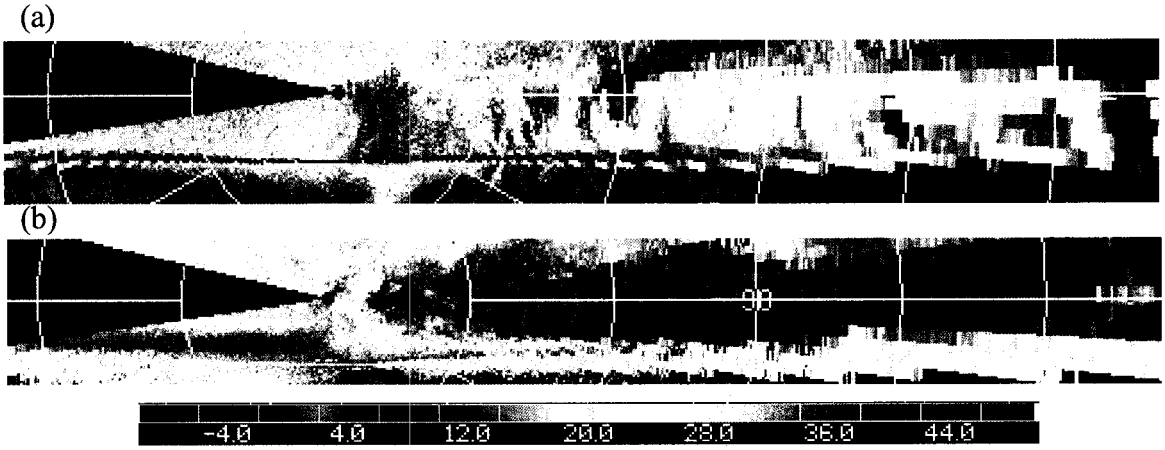


Figure 4.18. P-3 tail radar scan from 1630 UTC on 14 December 1992 indicating inflow passing through a region of robust stratiform precipitation. (a) reflectivity. (b) radial velocity, with cool colors indicating motion toward the aircraft and warm colors away. Aircraft is pointed toward the south, with MCS inflow from right to left. Positive radial velocities at low levels likely indicate gust front presence.

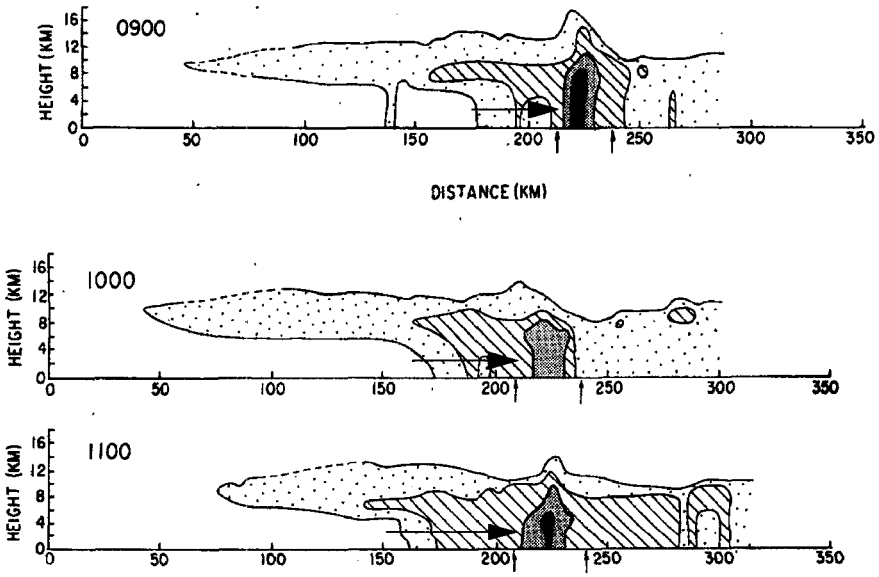


Figure 4.19. Evolution of the vertical structure of a tropical Atlantic squall system radar echoes from Houze and Rappaport (1984) to illustrate possible moistening of an inflow layer. Arrows indicate the storm inflow passing through a region of stratiform precipitation prior to rising into the convective region.

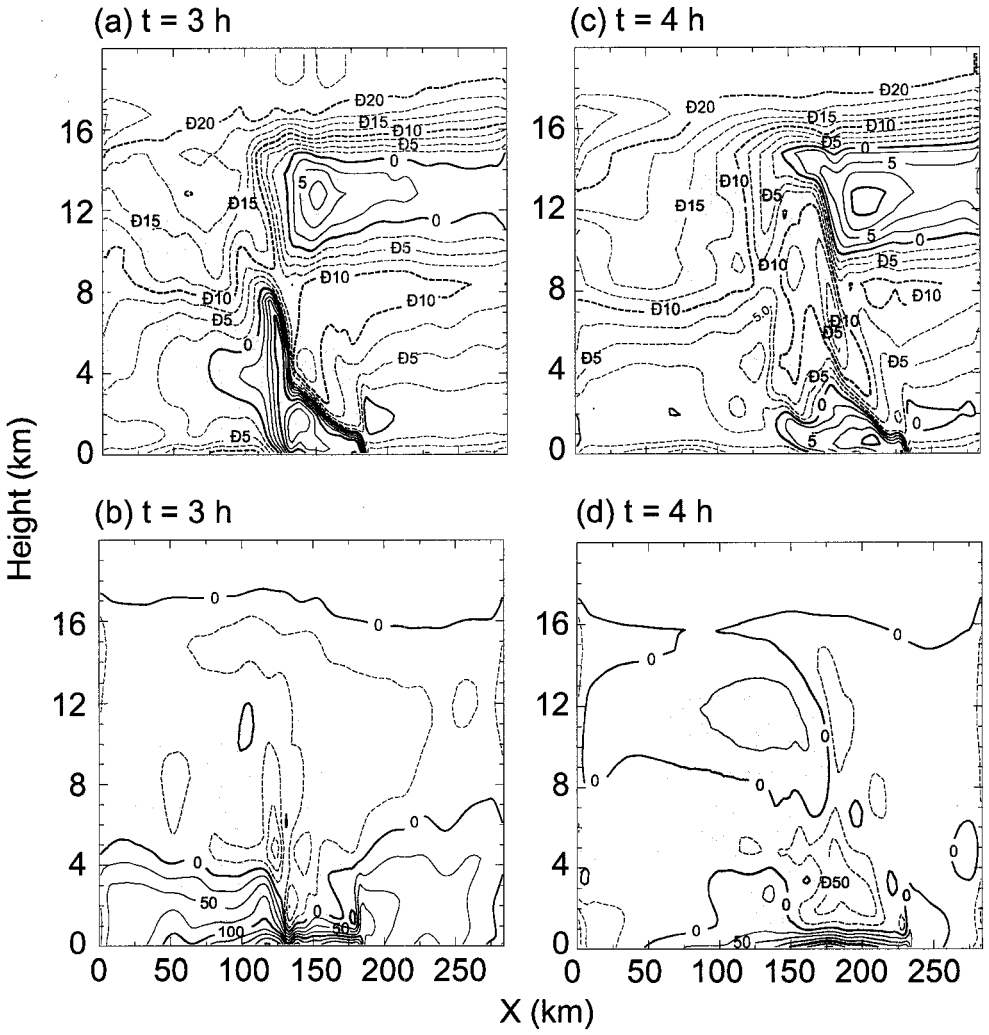


Figure 4.20. Vertical cross sections for the 14 December 1992 control and enhanced mid-level moisture experiments, taken along the same line as the cross sections in Figures 4.3 and 4.13. (a) and (b) System-relative inflow (u) overlaid on the shaded total hydrometeor field (ice + liquid) at 3 h. Contour interval is 2.5 m $s^{-1}$. (c) and (d) Perturbation pressure field overlaid on the shaded hydrometeor field at 4 h. Contour interval is 25 Pa. Different times correspond to a similar stage of the convective life cycle. Negative values are shown dashed.

# Chapter 5

# Momentum Transport Processes over the Warm Pool

Chapters 3 and 4 have discussed how organized, layered low-level inflows can arise under conditions where the midlevels are particularly moist. The layer mode of convective overturning appears to accompany a degree of mesoscale organization higher than of an ensemble of isolated updrafts. This chapter will demonstrate that the simulated organized tropical convection under the westerly onset and strong westerly regimes exhibits certain robust signals of low-level and midlevel momentum transport associated particularly with the extensive stratiform regions.

## 5.1 Character of the large scale momentum field

Chapter 1 describes how the large scale flow over the tropical western Pacific warm pool region during the southern hemisphere summer is largely determined by the phase of the ISO. Gill (1980) provides an idealized description of the surface wind over the propagating KR wave pattern: a strong westerly region of the KR wave structure between the gyres and a westerly onset region west of the transition from easterlies to westerlies.

The Gill model arises from the atmospheric response to an idealized stationary equatorial heat source but differs significantly from the ISO. First, the steady-state response is unable to capture the location of the most heavily precipitating deep convection relative to the wave pattern. Organized convection is observed to be in the region of westerlies rather than in the area of convergence where the easterlies transition to westerlies, as the idealized model might predict. Second, the vertical structure present in the tropical wind field is not produced by the idealized model. In the observed zonal wind shown in Figure 5.1, the westerly onset phase occurring in mid-December is characterized by a layer of easterlies overlying the weak surface westerlies, producing an easterly zonal shear below 550 mb. In the strong westerly region of late December, the maximum in westerlies is located at 750 mb, producing a shallow layer of westerly shear below this jet and an strong easterly shear through the depth of the troposphere. Finally, because the

Gill model is a steady-state response, the idealized circulation suggests no propagation mechanisms for the wave pattern, specifically how the region of strong low level westerlies becomes established at a given location as the ISO progresses.

The large scale vertical wind profile has a significant effect on the degree of mesoscale organization the convection attains and on the consequent momentum transport. Shear at low levels interacts with the horizontal vorticity generated by the cold pool (Rotunno et al. 1988) and is an important factor in explaining the long duration of MCSs, while upper level shear is important for its ability to advect solid condensate far from the deep convective region, enabling the creation and maintenance of broad regions of stratiform precipitation (e.g. Biggerstaff and Houze 1991). Thus, not only does the nature of the large scale flow itself determine the momentum transport, the flow also determines the degree of mesoscale organization, which can further influence the transport. The degree of mesoscale organization may be influenced by other aspects such as sea surface temperature, since the most extensive MCSs tend to be observed over the western Pacific and Indian Ocean warm pools (Chen et al. 1996).

## 5.2 Numerical model configuration

Details about the model and experimental setup were presented in Chapter 2. The experimental configuration is virtually identical to the thermodynamic part of the study, except the initial midlevel zonal momentum profile was modified in the 14 December 1992 simulation to bring it into better agreement with observations.

## 5.3 Comparison of the westerly onset and strong westerly simulations

### 5.3.1 Case descriptions

Conditions typical of the strong westerly flow regime, easterly shear throughout the depth of the troposphere above a strong low-level westerly jet, dominated the warm pool during the late December period of TOGA COARE. This time period was convectively active and characterized by numerous MCSs in the region of strong low-level westerly winds, satisfying the definition of super cluster conditions (Nakazawa 1988; Mapes and Houze 1993; Chen et al. 1996). Large, long lasting regions of stratiform precipitation

observed over this time period indicate a significant degree of mesoscale organization, possibly enabling the convection to affect the momentum character of the large scale flow over a significant area.

MM5 data from simulations over the TOGA COARE Large Scale Array under both flow regimes provide initial and boundary conditions for ARPS. The MM5 was initialized at 00 UTC on 14 December 1992 and 12 UTC on 23 December 1992, in the manner previously described in Chapters 2-4. Domain-mean profiles of the MM5 wind field in Figure 5.2 show reasonable agreement with observed wind field in Figure 5.1 for the two cases. However, the vertical structure in the 14 December profile lacks the strong midlevel easterly jet corresponding to the onset phase of the KR wave that is present in the observations shown in Figure 5.1. To bring the MM5 data into better agreement with the observations, easterly momentum was added in the form of a Gaussian profile, centered at 5.5 km, with standard deviation of 750 m. The peak magnitude of the added wind field was 12 m $s^{-1}$. The Gaussian profile was added to all of the MM5 wind fields prior to preprocessing by ARPS so that the modified wind field would be used for both initial and boundary condition data in the simulation discussed in this chapter.

Figures 4.2 and 3.2 show the general low level flow profile for the simulation domains. The MCS simulated in the 14 December case (Fig. 4.2) occurs in a region of low level westerlies characteristic of the onset period. Figure 3.2 shows that the MCS under strong westerly conditions is dominated by mesoscale convergence and strong westerlies over the southwest portion of the ARPS domain. The northeasterly winds in the box are an effect of the Rossby gyre located toward the north of the westerlies (see Fig. 3.1 and Fig. 8j in Chen et al. 1996). The domain has been extended further south and west relative to the simulation in Chapter 3 to include convection in the pure westerlies.

### 5.3.2 Synopsis of simulations

Chapters 3 and 4 discuss in detail the simulations of both cases and the comparison with observational data collected during TOGA COARE. The discussion here emphasizes the later stages of the MCSs after significant wake stratiform precipitation and mesoscale organization develops. A region of mesoscale forcing ultimately leads to the broad band

of convection shown in Figure 5.3b. New cells are periodically triggered, and the system strengthens and becomes more organized until about 3 h, when it begins to weaken as the cold pool propagates to the east at a faster speed than the convection, effectively outrunning the convection (Figs. 5.3f-5.3h). Lacking new convective cells triggered by a cold pool, significant wake precipitation remains for the next two hours (Figures 5.3c and 5.3d). The latter stages of the MCS do not have a strong linear pattern commonly associated with organized convection; nevertheless, studies have shown that such a signal is not a necessary condition for a significant degree of mesoscale organization (Houze et al. 2000). It will be shown that an organized mesoscale flow underlies the complicated reflectivity pattern in Figure 5.3c.

The broad, northwest-to-southeast oriented region of convergence at 1 km height implied by the wind vectors in Figure 5.4a forces initial convection in the 23-24 December strong westerly simulation. After three hours (Figure 5.4b), two extensive regions of precipitation, oriented from northwest to southeast, are present in the northern subdomain. The individual bands move toward the northeast, likely with the mean flow, while new convection is triggered in a nearly continuous manner on the leading edge of the cold pool. Even after five hours, the system is still quite strong (Figure 5.4c). In the 14 December case, after triggering convection early in the simulation, the cold pool rapidly propagates far from the MCS, and only the wake precipitation area remains. Here in the strong westerly case, however, the cold pool is weaker and propagates more slowly (Fig. 5.4e and 5.4f, subdomain N), triggering new convective elements which coexist with the decaying stratiform region. The significant convergence pattern indicating the forcing of the southern system is initially just west of the southern subdomain. Convection over the southern domain attains a squall line-like pattern and rapidly moves toward the east-northeast in a manner similar to the 14 December system. The initial and boundary conditions appear to impose on the simulation the more organized mesoscale circulation present in the MM5 fields.

### 5.3.3 Mean flow evolution

MCSs in both cases strongly affect the horizontal momentum at low levels. From a visibly smooth pattern of northwesterly flow, the wind field develops a complicated structure over the course of the 14 December simulation. The boxed region in Figure 5.3b shows an example where strong convective regions, characterized by large values of reflectivity, are generally associated with enhanced westerlies. This feature may also be seen at later times in the simulation. In the stratiform wake regions behind (to the west) the convective zone, the westerlies tend to be suppressed, as is visible over the regions outlined by the dashed boxes in Figure 5.3g and 5.3h. The evolution of the wind field in the strong westerly regime shows a related behavior in Fig. 5.4b and 5.4c, with westerlies increasing in strength over the convective region. Unlike the damping of the westerlies over the wake region in the onset case, the westerlies in the 23-24 Dec. simulation appear to actually increase there, just as they do in the active convective region.

Traditionally, momentum transport by convection has been addressed by assuming that the convection has some semblance of a linear shape and then analyzing the transports in the line-normal and line-parallel components. In this study, only the zonal component is addressed because the MCS geometry is not always easy to define and because the largest variability is normally in the zonal direction. Additionally, upscale feedback processes are most useful when framed in terms of the zonal component, since the KR wave structure is predominantly defined by variations in the zonal wind. Perturbation velocity best expresses the evolution of the flow field and its tendency to become more easterly or westerly with time. In the case of initial horizontal inhomogeneity, perturbation velocity is best defined by

$$u'(x, y, z, t) = u(x, y, z, t) - u_0,$$

where $u_0 = u(x, y, z, t = 0)$ is a fully three dimensional base state. The traditional choice for the base state, where it is defined to be a horizontal average of the initial field, introduces perturbations (spatial fluctuations) into the initial $u'$ field and makes the interpretation of evolution considerably difficult. This study considers either the total zonal wind field $u(x, y, z, t)$ or the perturbation $u'$ as defined above.

Figure 5.5 illustrates the time evolution of $\langle u' \rangle$ for both cases, with the $\langle\ \rangle$ operator indicating averages at the respective times taken over the boxes in Figure 5.3g, 5.3h, 5.4e, and 5.4f, which have been superimposed over the cold pools. The boxes roughly represent the stratiform wake region and are chosen to be well behind the 10-20 km wide convective region where LeMone (1983) found the bulk of convective momentum flux. As long as the boxes are kept roughly within the wake area and well away from the active convective elements at the front of the line, the averages are relatively insensitive to moderate changes in box size and location. The evolution of the momentum field in the context of organized precipitating mesoscale regions explains why the wake region of the MCS is the focus. Because of the way $u'$ is defined, the initial profiles are zero. Vertical profiles of $\langle u' \rangle$ from the onset case in Figure 5.5a show an increase with time in easterly perturbation momentum from just above the surface to a height of 5.5 km, approximately the level of the easterly jet maximum. Above this feature is a shallow, 2.5 km layer of westerly perturbation momentum, overlaid by strong easterly tendencies that span the remaining depth of the troposphere. The strong westerly domains, in contrast, show increases in low level perturbation momentum from the surface to about 5 km (Figures 5.5b and 5.5c). Above local minima from 5.5-7 km over the northerly subdomain (Figure 5.5b), the westerlies tend to increase with time, while a deep layer of easterly tendencies overlay the low level westerly tendencies in the southern subdomain (Figure 5.5c). These statistics confirm quantitatively the wake features visible in the Figure 5.3 and 5.4 wind fields that suggest the momentum tendencies in the two flow regimes differ in some fundamental way. The next two sections address particulars about how the zonal momentum structure is modified by MCSs in the westerly onset and strong westerly regimes of the ISO.

## 5.4 Momentum transport during the westerly onset phase

### 5.4.1 Evolution of the zonal wind component

Figure 5.6 shows the hourly evolution from 3-6 h of the 14 December experiment. The initial $u'$ field is uniformly zero, and the velocity structures that subsequently develop

result directly from the convection or the boundary condition forcing. By 3 h, the vertical cross section of $u'$ in Fig. 5.6 shows that the flow in the upper part of the domain associated with the convective region is strongly divergent (See Box A), though asymmetrically so, with easterlies being significantly stronger and covering more area than the westerlies. The asymmetry arises when the convective updrafts act upon the deep layer of westerly shear from 5.5 km up to nearly 13 km, biasing the momentum features toward easterlies. Box B outlines a small transient region of easterlies being transported upward, a feature consistent with the results of Houze et al. (2000), who found that during the onset phase the convective updrafts consistently carried easterly momentum upward, in a direction opposite that found in the stratiform region. This transient feature is likely responsible for the easterly bias in the divergence structure.

The cross sections in Figure 5.6 from 3-4 h show a feature in typical of lines of convection. In the hour between these figures, both $u'$ and perturbation pressure cross sections show that the cold pool propagates from X=158 km to X=200 km. At 3 h, $u'$ at low levels just to the west of the cold pool edge are colored red and have approximate magnitudes of 10 m $s^{-1}$, while the easterly perturbation flow in blue just above the cold pool is 8 m $s^{-1}$. An hour later, the lower levels behind the cold pool edge have positive values of as large as 14 m $s^{-1}$, while the area above these positive perturbations has negative values of 12 m $s^{-1}$. A perturbation pressure gradient associated with the strong convective region has apparently accelerated the inflows. A strong cold pool produces a low level pressure perturbation maximum, and strong latent heating a hydrostatic minimum above, resulting in an eastward-directed pressure gradient acceleration in the cold pool and westward-directed acceleration above (between X=75 m and X=160 m in the 3 h field of Fig. 5.6). The perturbation pressure pattern produces increased low level westerlies and further strengthens the midlevel easterly jet, implying a local evolution of the momentum field which is countergradient in nature. Because the convective region weakens significantly between 3 h and 4 h, the hydrostatic pressure minimum associated with strong latent heating (at X=120 km) is significantly reduced, likely weakening the front-to-rear flow acceleration. Although the pressure gradient acceleration, averaged over a suffi-

ciently large domain, becomes zero, the system may through it generate momentum locally which can then be transported vertically by updrafts and downdrafts. The easterly momentum being transported upward in the convective region is likely partly environmental, partly system-generated.

Most relevant to the organized mesoscale aspect of the system is the downward transport of midlevel easterly momentum that is apparent from 4-6 h in Figure 5.6. The values of $u'$ become negative at or just below the easterly jet maximum (5.5 km) and descend to the surface. The magnitude is not particularly strong (4-6 m $s^{-1}$), but the area affected is significant. The transition at the surface from westerly to easterly perturbation flow (represented by the arrows in 5 h and 6 h vertical cross sections) occurs somewhat abruptly and in a manner similar to the single-Doppler radar observations from Houze et al. (2000), where easterly flow periodically "pulses" down into the boundary layer. A significant degree of mesoscale organization is prerequisite to the low level downward transport of easterly momentum, as the transport does not occur until a broad region of stratiform precipitation becomes established.

5.4.2 Momentum forcing structure

The structure of the momentum forcing can shed further light on the relative importance of the different terms. The time-averaged u-momentum equation is

$$\frac{\partial \overline{u}}{\partial t} = -\frac{1}{\rho}\frac{\partial \overline{p}}{\partial x} - \overline{u}\frac{\partial \overline{u}}{\partial x} - \overline{v}\frac{\partial \overline{u}}{\partial y} - \overline{w}\frac{\partial \overline{u}}{\partial z} - \overline{F_u} \quad ,$$

TEN PGA HAD VAD SGS

where p is pressure; w is vertical velocity; $F_u$ is subgrid scale mixing. The forcing terms are calculated from 2 minute model data dumps, and the averaging operator is

$$\overline{(\ )} = \int_{T_1}^{T_2} (\ )\, dt,$$

with $T_2$-$T_1$, the averaging time for the calculation, being 30 minutes.

In the westerly onset case, the system-wide downward transport of midlevel easterlies does not take place until an organized pattern of mesoscale descent is present.

Although the model reflectivities at 4 h and 5 h become somewhat disorganized, reflecting the decaying character of the convection, the horizontal cross section of the VAD field in Figure 5.7, taken at an altitude of 2.4 km, shows a highly organized pattern. The VAD forcing in the boxed region results from weak downward velocities typical of wake precipitation regions, with magnitudes in this case in the 0.5 m $s^{-1}$ range. The spatial extent of these downward velocities is impressive, and a rough calculation provides an estimate of 6300 $km^2$ with significant (at least 0.25 m $s^{-1}$) downward vertical motion. This large, robust area of mesoscale descent provides the means of transporting significant easterly momentum, either environmental or system-generated, toward the surface. The VAD cross section in Figure 5.7 indicates that the large region of mesoscale descent coupled with the large scale zonal momentum field is responsible for the negative values of near the surface late in the simulation.

The latter stages of the convection are of most interest, since that is when the significant region of easterly perturbation momentum becomes established at low levels. West-east cross sections of VAD, HAD, PGA, and TEN, taken at a late stage of the convection and averaged over a 40 km strip, are given in Figure 5.8, with arrows indicating the downward easterly momentum transport implied by Figure 5.6. SGS is omitted, as in Yang and Houze (1996), since the turbulence term is only appreciable near strong convective updrafts and regions of detrainment in the upper troposphere. Figure 5.8a confirms that the vertical transport term is strongly negative below the easterly jet maximum (z = 5.5 km) in the region where the low level easterlies near the surface increase. Because the low level westerlies are maximum between 1-2 km rather than at the surface, the VAD term is positive between the surface and the westerly maximum, as the descent attempts to transport this positive momentum downward. Mapes and Wu (2000) also show regions of positive u-eddy tendency (e.g. their Figure 3c) at low levels during the westerly onset phase, which increase in magnitude as the ISO transitions to the strong westerly phase. The HAD pattern (Fig. 5.8b) below the easterly jet maximum (5.5 km) is partially out of phase with the vertical transport term, a result similar to that found by Trier et al. (1998). Between X=75 and X=225 km, the TEN term in Figure 5.8d shows that the sum of the

negative HAD forcing and the positive values of VAD in the same region results in a slight negative term, indicating that easterly momentum, particularly over the west side of the domain, descends all the way to the surface, as indicated by the arrow. The strong perturbation pressure field at 3 h in Figure 5.6 suggests that the convective inflows might be accelerated in the early stages of the simulated MCS. By the decaying stage of the convection shown in the forcing cross sections, the PGA field has become quite disorganized but still comparable in magnitude to the transport terms. Regions of weak low level forcing between X=0 and X=150 km in Fig. 5.8c are likely associated with the elevated positive hydrostatic pressure perturbation visible at 5 h and 6 h in Figure 5.6. This elevated perturbation pressure maximum appears to be a hydrostatic response to the melting layer just above.

## 5.5 Momentum transport during the strong westerly phase

### 5.5.1 Evolution of the zonal wind component

In the strong westerly regime, above the low level westerly maximum, the u-momentum shear is deep, monotonic, and easterly — much simpler than the complex easterly jet structure present during the onset phase. The height of maximum environmental westerlies is already rather low at the beginning of the simulation, and vertical cross sections of the full $u$ field indicate that this jet slopes downward toward the east (arrows in the vertical cross sections in Figure 5.9), resulting in an enhancement of low-level zonal velocity. The westerly jet structure maximum just below 2 km in the northern subdomain cross section is nearly horizontal at the initial time, while from 3-6 hours it dramatically slopes downward toward the east. The southern subdomain cross sections show a similar structure but with a deeper mid-level inflow layer. Houze et al. (2000) documented a similar structure and suggested that the flow-feature likely resulted from simple downward transport of momentum possibly combined with the MCS-generated perturbation pressure field accelerating the inflow toward the convective region (similar to but more general than the mechanism suggested by Smull and Houze 1987).

The cross sections of $u'$ in Figures 5.10 and 5.11 provide further evidence of the downward sloping mid-level inflow structure over the northern and southern subdomains. Figure 5.10 documents the evolution of $u'$ over the northern subdomain at successive hours from 3-5 h. As before, $u'$ as defined is initially zero everywhere. The cross sections taken through the mostly stratiform region of the MCS show a widespread, contiguous hydrometeor pattern (shaded field in the lower frames of Figure 5.10). Upward transport of momentum near the active convection is evident in the boxed region in the vertical cross section of $u'$ at 4 h. This region contains a significant, elevated pocket of westerly velocity perturbation. These pockets of enhanced positive $u'$ are produced at early times in the vicinity of strong convective updrafts (boxed region in Figure 5.11 at 3 h) and result from upward vertical transport, as do the pockets of easterlies at 3-4 h in Figure 5.6 for the westerly onset case. By 3 h into the simulation, the pressure field over both subdomains is generally smooth with small perturbations associated with the cold pool and convective heating maxima. The negative region of $u'$ at 3 h (x = 380 km, z = 5 km) is clearly a pressure-driven inflow arising from the hydrostatic perturbation low pressure.

### 5.5.2 Momentum forcing structure

As was done for the westerly onset case, the spatial structure of the momentum forcing determines the processes responsible for the increase in zonal velocity at low levels, from the surface to 1 km. The VAD forcing term over the northern and southern subdomains, averaged over the half hour interval from 4.5-5 h and plotted in Figure 5.12, shows in the dashed boxes broad regions of positive forcing at a height of 1 km, which in the stratiform wake region is well correlated with the vertical velocity pattern. The height of maximum westerlies lies lower than the vertical velocity maximum (peak just below the melting level), but enough overlap is present to produce this transport signal in both regions. The late stage of the system is characterized by a broad region of organized mesoscale descent, a significant area of which is covered by vertical velocities stronger than 0.25 m $s^{-1}$. Above the area of mesoscale descent are regions of significant updrafts with magnitudes of ~2 m $s^{-1}$, indicating an organized mesoscale aspect of the system, both

in structure and life cycle. This region of elevated mesoscale ascent slopes upward toward the rear of the MCS in the same fashion as midlatitude squall lines (Houze 1993). The systems observed during the strong westerly phase of TOGA COARE tended to be larger and more organized than those observed during the westerly onset phase (Chen et al. 1996; Houze et al. 2000), so it is plausible that the regions of mesoscale vertical motion are larger, too. In the model, the mesoscale descent arises from the melting, sublimation, and subsequent partial evaporation of aggregates falling over the broad stratiform area.

West-east cross sections for VAD, HAD, PGA, and TEN for the northern subdomain are given in Figure 5.13. Results parallel those for the westerly onset case, though the forcing terms are generally opposite in sign, with the vertical transport term being negative in regions of the low level velocity perturbations. The peak of the westerlies lies between 1-2 km, so the positive forcing is confined below this maximum (between X=20 km and X=120 km), and because the mesoscale descent is broad and robust, so too are the transport terms. Above the low level westerly maximum is a deep layer of easterly shear extending through much of the troposphere, both in the observations (Figure 5.1) and in the large scale MM5 fields (Figure 5.2). In the layer from 2 to 5 km altitude, just above the low-level jet maximum, the VAD term is negative (Figure 5.13a). This signal results from the pattern of organized mesoscale descent superimposed over the deep layer of easterly shear. The mesoscale vertical velocity transitions from downdraft below the melting level to updraft above. This broad region of elevated ascent above the melting level explains the VAD term becoming positive from 5 to 9.5 km (boxed region in Fig. 5.13a), where robust organized stratiform updrafts act in concert with the deep layer of easterly shear to increase the westerly momentum. In the 14 December case, the stratiform updraft quickly decays and is small relative to the downdraft over the period in which the forcings are calculated. In addition, the stratiform updraft is imposed over a region of only weak shear, explaining the negligible VAD signal there. Together with the mesoscale downdraft transport at lower levels, this pattern results in a +/-/+/- VAD structure in the vertical. I speculate that the top most region of negative VAD results from transport by the stratiform updraft of front-to-rear inflow. In contrast, a mesoscale downdraft acting by itself on an

easterly jet structure, as it does in the 14 December onset case, tends to produce a simple -/+ dipole as seen on either side of the easterly jet (~4.5 km altitude) in Figure 5.8a. The region of negative VAD below 1.5 km in Figure 5.8a results from downward transport of low-level westerlies, which are maximum just above the surface.

As in the westerly onset case, the HAD pattern from X=10 km to X=120 km is largely out of phase with the VAD term and has a -/+/-/+ structure in the vertical. At the surface, the VAD term slightly dominates the out-of-phase HAD forcing. The PGA term at this late stage of the convection is quite disorganized, though positive forcing is significant below 4 km between x=65 km and x=100 km, indicating acceleration of the system rear inflow. The net forcing is disorganized, the boxed region in Figure 5.13d showing the only robust signal of a superposition of the pressure-driven descending rear inflow and the upward VAD transport in the wake region. Trier et al. (1998) also found that the magnitude of the net forcing was generally much smaller than that of individual forcing terms. The weak NET signal at low levels indicates that at this particular time the downward transport of westerly momentum by the organized wake downdraft is mostly balanced by the other forcing terms.

Forcing terms over the southern subdomain exhibit similar behavior. The VAD term in Figure 5.14a has a +/-/+ structure, the low-level positive over negative the result of negative vertical velocities on a low-level westerly jet structure. HAD is out of phase, with the region of positive values decisive in establishing a positive zone of TEN (box in Figure 5.14d). The PGA term at this stage is rather weak. The out of phase structure of VAD and HAD in these simulations appears to result from the sloping nature of the descending inflow layers that is brought about by pressure accelerations during the vigorous convective stage — a purely horizontal inflow passing through a mesoscale region of descent would presumably produce a vertical but not a horizontal transport signal. This interpretation is consistent with the squall line rear inflow paradigm of Smull and Houze (1987).

## 5.6 Inferred modification of the large scale momentum structure

This analysis does not discriminate between transport of system-generated momentum sources and transport of ambient flow momentum, and because of the small size of the domain a definitive conclusion as to how an MCS occurring under each regime affects the large scale momentum structure cannot be drawn. The simulation results in the onset phase show that the active convective region is dominated by the pressure gradient acceleration which increases westerly momentum near the surface and easterly momentum at midlevels, producing a countergradient momentum transport relative to the large scale mean monotonic easterly shear between the surface and 550 mb (visible in Figure 5.1). However, the upward transport of easterly momentum in the convective region is downgradient, at least in the zone of westerly shear from 5.5-12.5 km, since the transient features in Figure 5.6 (box B) that transport easterly momentum upward would tend to decrease the mean shear profile. The latter stages of the convection are characterized by a broad region of wake precipitation composed of decaying convective elements with downward vertical velocities below the 0 °C level. These gentle velocities, coupled with the large scale flow profile, produce a negative downward transport of momentum in the region where the easterlies increase with height. The nature of the transport in the precipitating wake region is downgradient, though evaluating the significance of downgradient or countergradient is made more challenging when the flow field is nonmonotonic, as is the case in the westerly onset phase. For complicated flow profiles, it may in fact be conceptually more practical to say that the momentum associated with the jet descends (Mapes and Wu 2000) rather than to address the evolution of shear itself.

It is clear that for the westerly onset case simulated here the net effect of the MCS on the large scale momentum field lies somewhere between the effects of the convective and wake components. Unfortunately, the net effect cannot be meaningfully assessed using these simulation results, since the strongest convective and most organized wake stratiform circulations do not exist simultaneously. Analysis is further complicated by the nature of the boundary conditions, in which points near the boundary are forced to the external solution.

Houze et al. (2000) postulate that the descending easterly MCS inflows at low levels act as a drag on the large scale propagating Kelvin-Rossby wave pattern and are a negative feedback to the large scale flow structure. The downward transport of easterly momentum is opposite to the tendency of the large scale wave to increase westerly momentum at lower levels and would tend to retard the propagation of the wave structure. In this simulation, momentum transport terms calculated at low levels over the organized stratiform wake region seems to support those findings. The net partitioning of convective and stratiform momentum forcings remains unknown, however. One external manifestation of negative feedback may also be present in enhanced low level convergence resulting from the interaction of low level onset westerlies with the downward transported easterly momentum visible at 5 h and 6 h in Figure 5.6. This interaction could conceivably result in low level convergence that might initiate new convection west of the original MCS, in a direction counter to that of the propagating wave pattern. Although the downward transport of easterly momentum is captured by these simulations, the domain is not large enough to capture the interaction between this momentum perturbation and the large scale flow; however, it seems reasonable to assume that a larger domain might capture new convection initiated on the west side of the decaying MCS.

Unlike for the simulated westerly onset case, where it was difficult to assess the net momentum forcing from competing portions of the MCS, in the strong westerly simulation both convective and stratiform regions act to strengthen the westerlies at the lowest levels. Like a typical line of convection, the cold pool in the strong westerlies simulation produces a positive pressure perturbation at the surface, and a hydrostatic minimum aloft, a result of latent heating in the convective region. The pressure field accelerates the low level westerlies. The organized mesoscale downdraft is able to transport downward the strong preexisting environmental westerlies and any westerlies produced by the MCS-generated perturbation pressure pattern. In the strong westerly region simulation, the pressure generation term plays more of a role than the vertical transport in strengthening the low level westerlies. This process is envisioned to be a synergistic one where the MCS as a whole is able to increase the low level momentum more than the simple sum of sepa-

rate convective and wake stratiform regions. Pressure perturbations associated with the convective region act to accelerate the air flowing through the stratiform wake, and this momentum is transported downward by both pressure forces and organized mesoscale downdrafts. The stratiform wake region acting along will produce transport, but only of environmental momentum features; the convective region alone will generate momentum but will not be able to transport it downward. It seems logical that both regions together produce the optimum increase in low level momentum.

For the strong westerly regime of the ISO, vertical momentum transport is postulated to act as a positive feedback to the large scale flow structure by attempting to amplify westerlies at the lowest levels (Houze et al. 2000). The simulation implies a definite increase in zonal momentum at levels just above the surface, resulting from a combination of vertical transport and pressure gradient acceleration. The resulting enhanced convergence at the gust front on the eastern edge of the system implies a positive feedback to the propagating Kelvin-Rossby pattern, since the triggering of new convection would be occurring along the same direction as the wave propagation. Furthermore, it is surmised that the same sign of the low level system-generated momentum and vertical transport aids in producing stronger surface fluxes of heat and moisture and more widespread convection typical during the strong westerly phase.

## 5.7 Summary

The manner in which warm pool convection affects the large scale momentum fields is dependent on the large scale flow which is itself a function of the phase of the ISO. This observation allows the convection to be thought of as a feedback control on the amplitude and propagation characteristics of the large-scale Kelvin-Rossby wave pattern. The important aspect of this study is to emphasize how the degree of mesoscale organization may influence the establishment of strong low level westerlies as the ISO progresses. In this study, convection occurring during the westerly onset phase appears to act as a negative or neutral feedback on the propagation of the wave pattern, depending upon the partitioning of momentum forcing between convective and stratiform portions of the MCS.

Unfortunately, convective and wake stratiform elements do not coexist in the 14 December simulated convection, so the net effect is difficult to determine. The convective updrafts transport upward easterly momentum associated with the midlevel jet, acting to smooth the momentum profile. On the other hand, the pressure accelerations associated with the tilted updraft/downdraft structure attempt to increase the mean shear at low and midlevels, although it must be noted that a variety of storm orientations were observed on this day, which for some updraft orientations would not produce the countergradient flux seen in the simulation. In the wake region, midlevel easterly momentum is brought downward to low levels, acting counter to the low level westerlies which the propagating wave pattern is attempting to establish. This is the robust downward transport signal documented by Houze et al. (2000). Increased easterly momentum at low levels would tend to generate new cells on the west side of existing convection, according to the Houze et al. (2000) conceptual model, which might act as an additional mechanism to retard the onset of the strong low level westerlies.

Organized mesoscale descent, which plays such a strong role in the onset simulation, is present in the strong westerly phase but has a less significant effect in modifying the environmental momentum, since little overlap is present between the westerly jet and mesoscale descent structures. More important is the momentum associated with the rear-to-front inflow and the westerly momentum being transported upward by front-to-rear ascent organized on the mesoscale. In the strong westerly phase, the convection transports westerly momentum downward, implying enhanced convergence on the east side of the existing MCS, which results in stronger forcing for new convective elements in the same direction as the propagation of the wave structure and would constitute a positive feedback process.

The correlation $w'u'$ in the boxed regions of Figure 5.15 synopsizes the effect that the stratiform wake region and overall mesoscale organization might have on the large scale flow. The positive values of $w'u'$ in Figure 5.13a indicate a region of easterly momentum being transported downward in the westerly onset phase, while the broad zones of predominantly negative $w'u'$ in Figures 5.13b and 5.13c indicate downward

transport of westerly momentum during the strong westerly phase. Although not specifically of interest, an area of negative $w'u'$ to the south of the boxed region in Figure 5.13a results from upward transport of convectively-generated easterly inflow visible the hour before in the vertical momentum cross section at 4 h in Figure 5.6. Mean profiles of $w'u'$ over the model domain and the stratiform region shown in Figure 5.16 demonstrate that the stratiform transport signal (and the flux convergence, indicating momentum tendency) is reflected in the domain-mean, implying the possibility of upscale feedback. The layer of positive $w'u'$ from 1-4 km indicates downward transport of easterlies. Similar behavior is present in the strong westerly regime, as seen in Figure 5.17. The stratiform regions show strong, deep negative layers of $w'u'$ at low levels, indicating downward transport of westerlies. The entire domain also shows this signal, though averaging over such a large area reduces its magnitude.

The net effect of the MCS on the environmental momentum is ambiguous for this simulation because of the system's rapid movement toward the east and the fact that the system-relative low level inflow is easterly. As explained in Chapter 3, TOGA COARE radar data and time-longitude plots of satellite-tracked cloud clusters support the possibility of both eastward- and westward-moving MCSs. The conceptual cartoon in Figure 5.18 illustrates differences between eastward- and westward-moving MCSs. The westerly onset simulation is best described by Fig. 5.18a, where the system-relative inflow is from the east, and local pressure gradient accelerations associated with the convective region accelerate the ascending and descending branches of the inflow, as discussed in Sec. 5.4.1. This acceleration is countergradient, since the ascending branch attempts to further accelerate the midlevel easterly MCS inflow, while the descending branch accelerates the low level westerlies. In the organized stratiform wake region, a broad mesoscale downdraft transports downward easterlies associated with the midlevel jet plus system-generated momentum. As the schematic indicates, momentum tendencies from the pressure-driven inflow and that from the vertical transport over the wake region are for this MCS orientation of opposite sign, making the net effect difficult to discern.

The analyses of Houze et al. (2000) imply that Figure 5.18b might better represent momentum behavior for a westward-moving MCS. As in the easterly-moving case, an organized region of descent interacts with the easterly jet structure to transport easterlies downward. Here, however, the downward transport acts in concert with the pressure field, which accelerates the inflow downward and toward the west. For the westward-moving MCS, both the active convective and stratiform parts of the circulation act in the same sense to increase easterly momentum at low levels. This is the MCS orientation that best fits the Smull and Houze (1987) rear inflow paradigm.

Figure 5.18c shows a conceptual sketch of the MCS inflows as they appear in the strong westerlies simulation. The drawing is nearly a mirror image of Fig. 5.18b and indicates the tendency of the stratiform wake and convective region to act in the same manner toward increasing the low level westerlies. The convective region accelerates the westerly inflow toward the east and downward, while momentum associated with the inflow is transported downward by mesoscale downdrafts. Mid-level inflow momentum is also transported upward by broad mesoscale ascent that by the later stages of the westerly onset simulation has decayed and is not present.

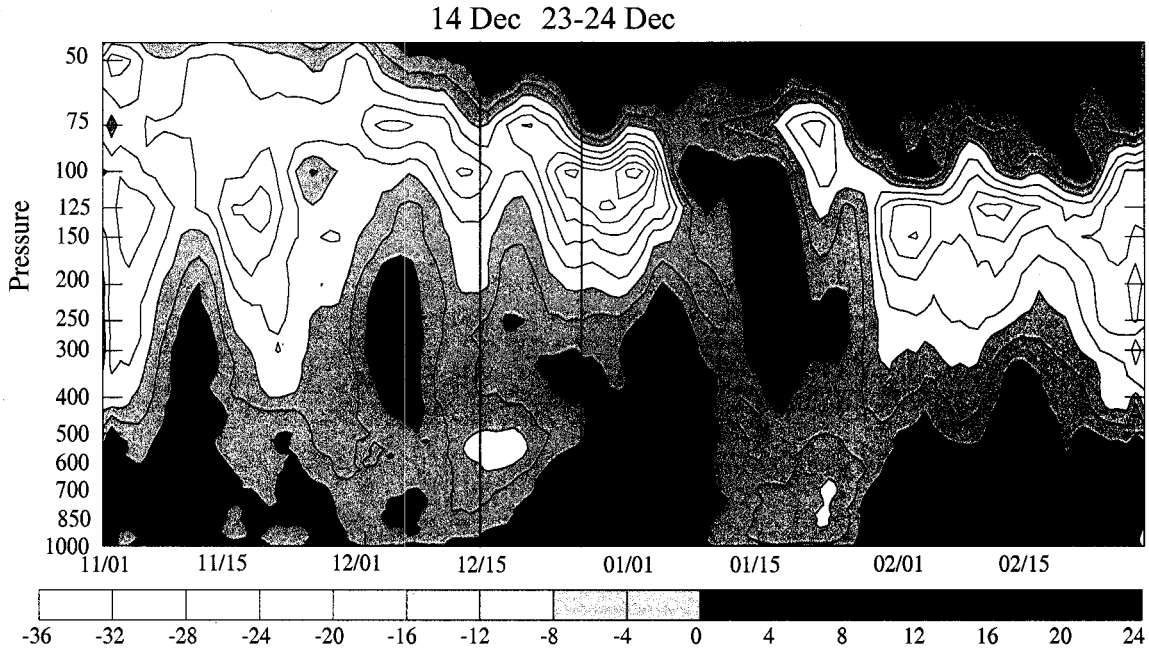


Figure 5.1. Time-height plot of 5-day running mean of zonal wind ($ms^{-1}$) from rawinsonde observations within the intensive flux array (IFA) from November 1992 to February 1993. (Adapted from Chen et al. 1996).

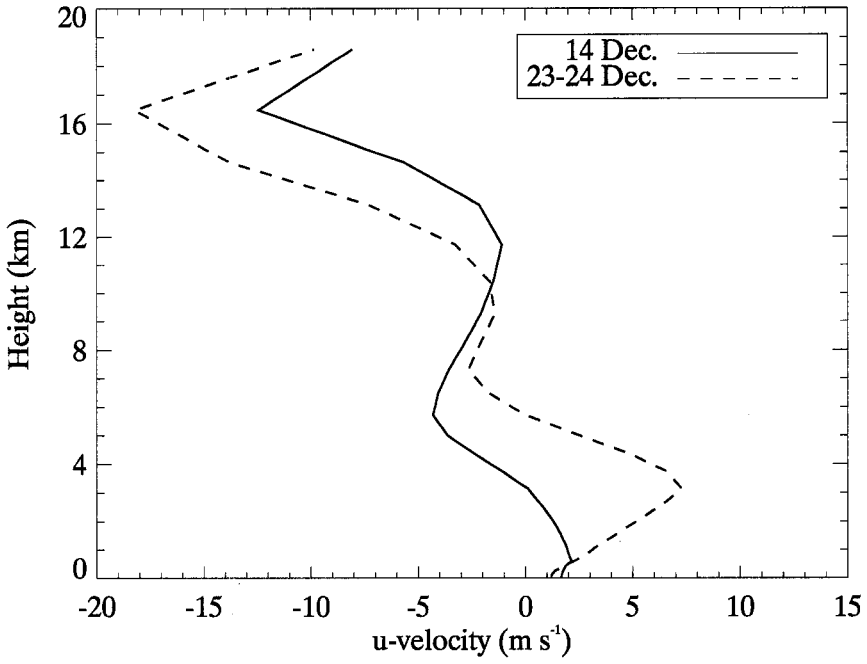


Figure 5.2. Mean zonal velocity over the MM5 domain for 14 Dec. and 23-24 Dec. cases.

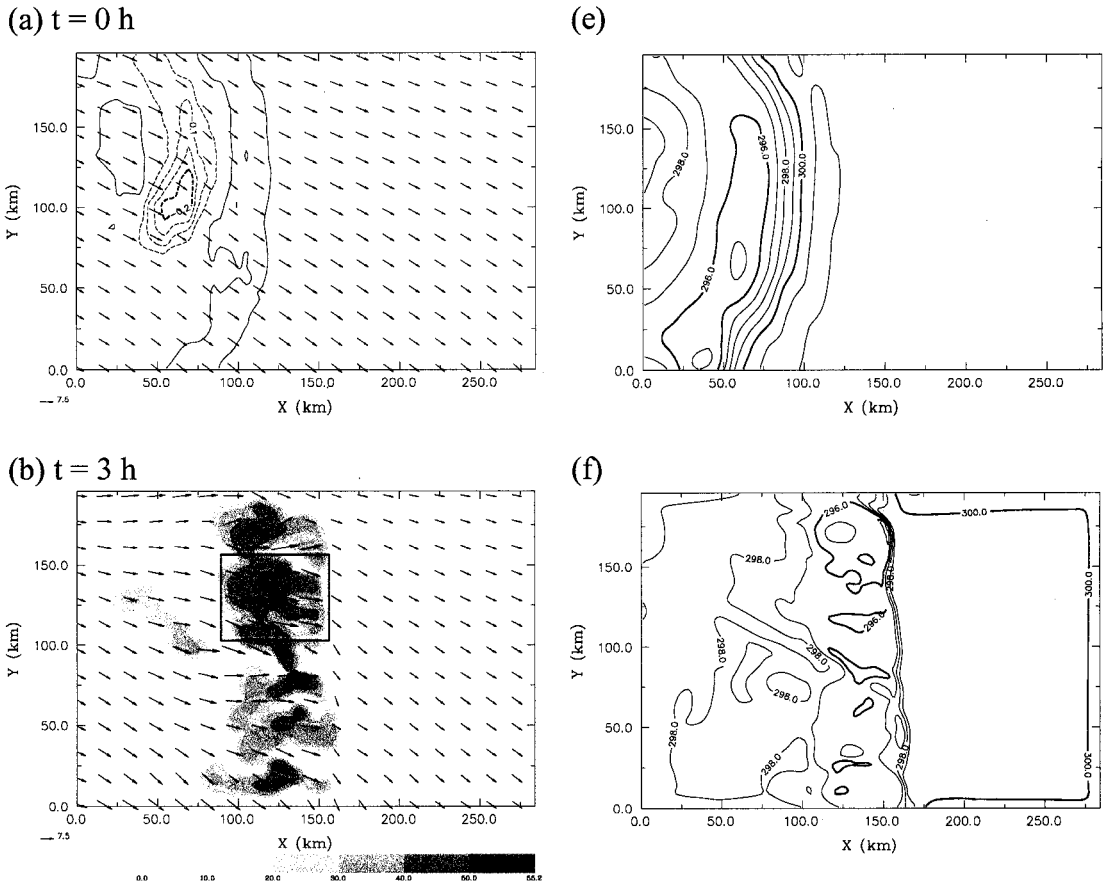


Figure 5.3. (a)-(d) Model-derived radar reflectivity and wind vectors at specified times taken at 1 km altitude for the 14 December 1992 experiment. (e)-(h) Surface potential temperature (contour intervals of 1 K). Solid box in (b) identifies enhanced westerlies in the convective region. Boxes in (g) and (h) roughly denote the stratiform region over which mean statistics in Fig. 5.5 are calculated.

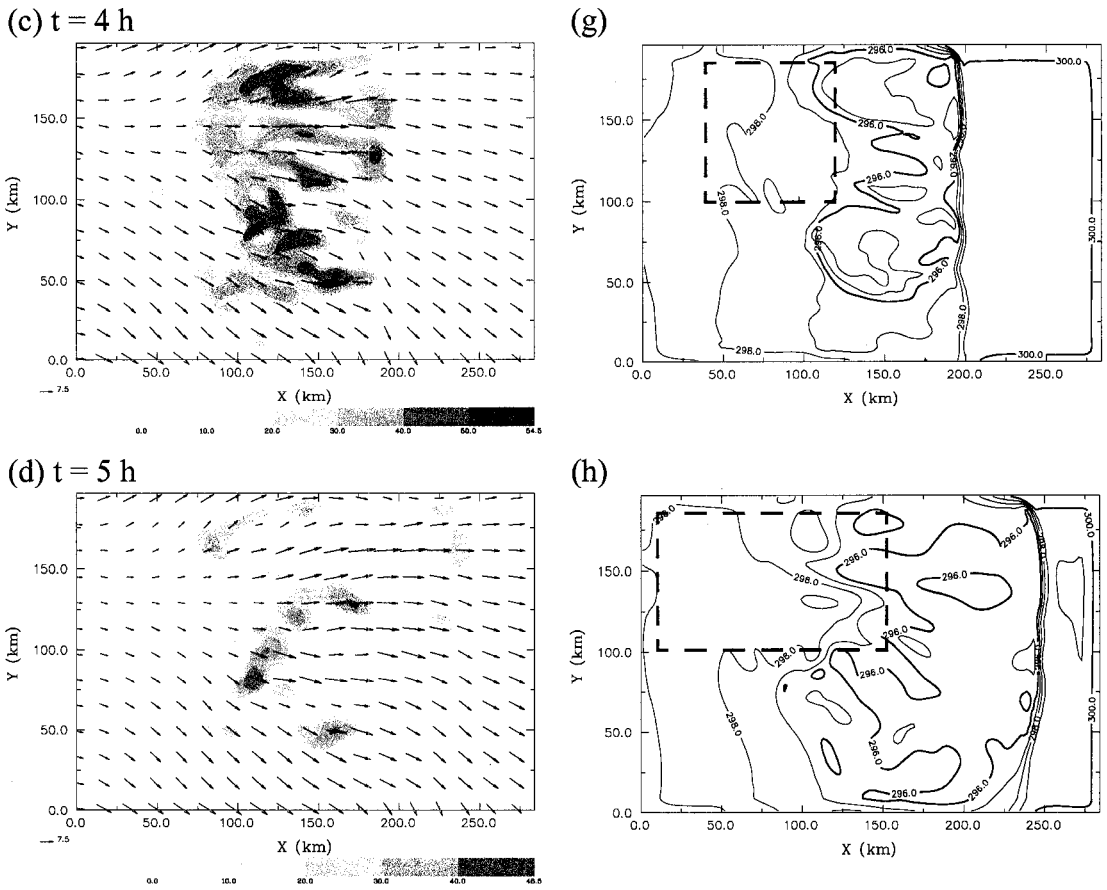


Figure 5.3. (Continued).

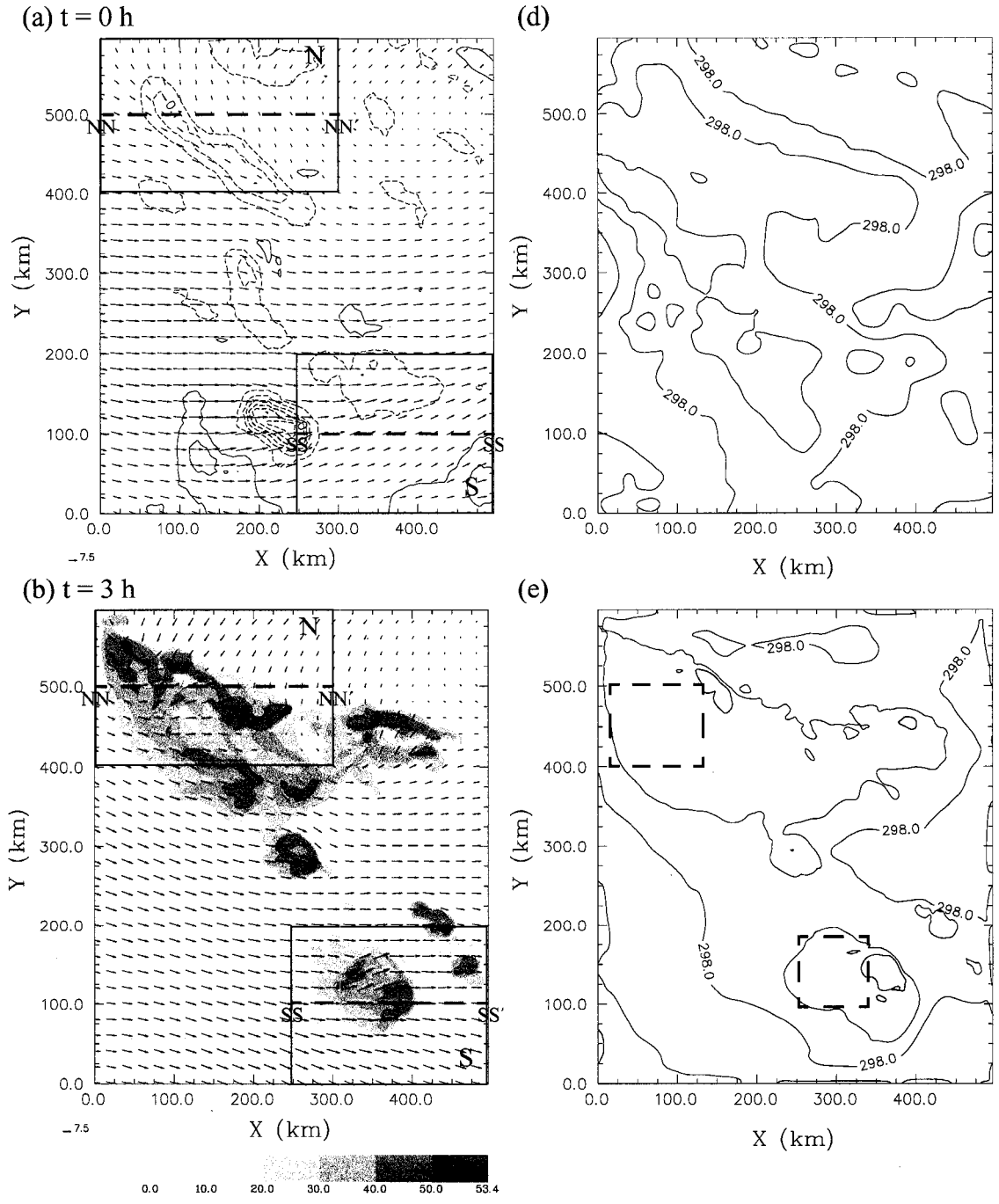


Figure 5.4. (a)-(c) Model-derived radar reflectivity and wind vectors at specified times taken at 1 km altitude for the 23-24 December 1992 experiment. Northern and southern subdomains are indicated by "N" and "S." Dashed lines NN–NN′ and SS–SS′ indicate cross sections shown in Figure 5.9. Divergence ($10^{-3}$ $s^{-1}$) at 1 km is overlaid in (a). (d)-(f) Surface potential temperature. Boxes in (e) and (f) roughly denote the stratiform regions over which mean statistics in Fig. 5.5 are calculated.

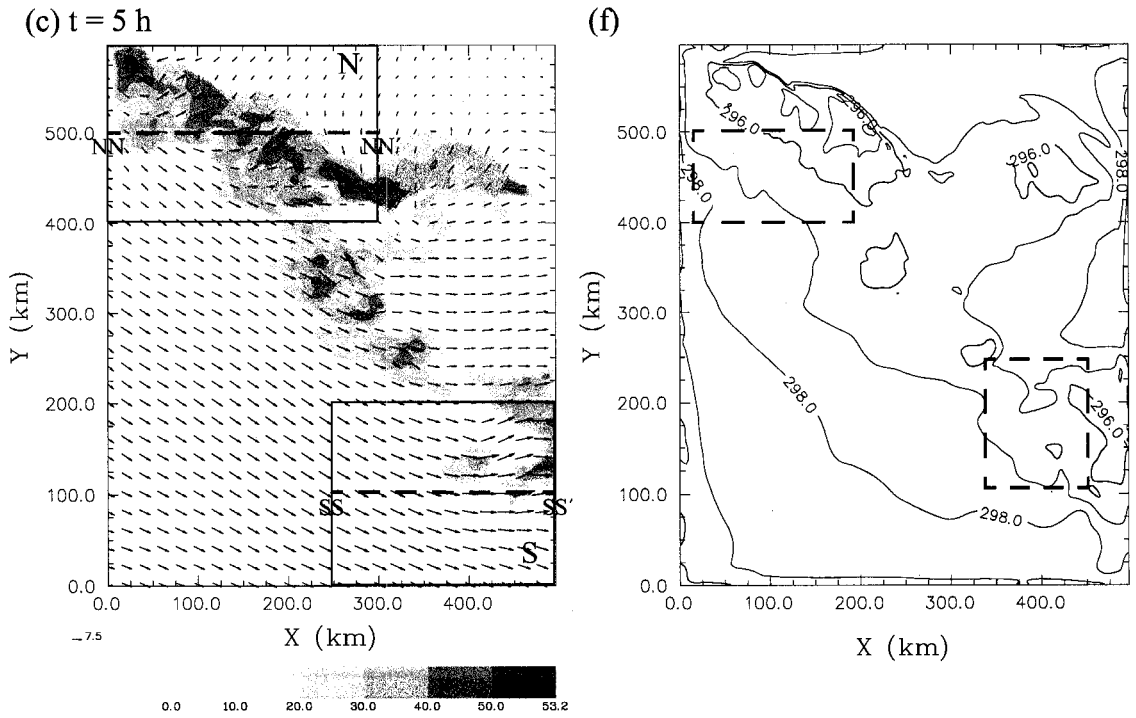


Figure 5.4. (continued).

(a) 14 Dec. 1992

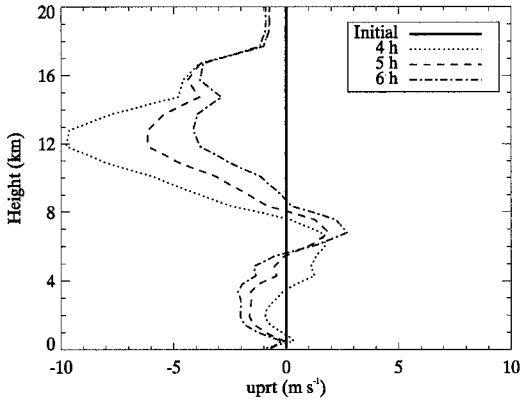


(b) 23-24 Dec. 1992 (Northern subdomain)

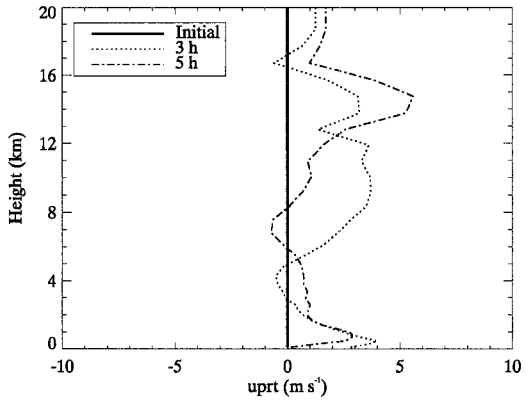


(c) 23-24 Dec. 1992 (Southern subdomain)

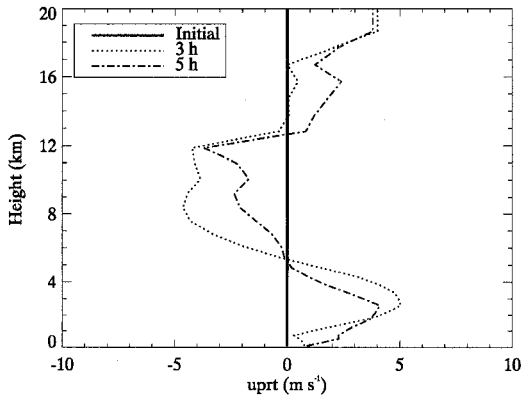


Figure 5.5. Evolution of mean profiles of $u'$, as defined in the text, for the 14 and 23-24 December 1992 experiments. For each case, calculations are made over the stratiform regions denoted by the moving boxes in the potential temperature cross sections of Figs. 5.3 and 5.4.

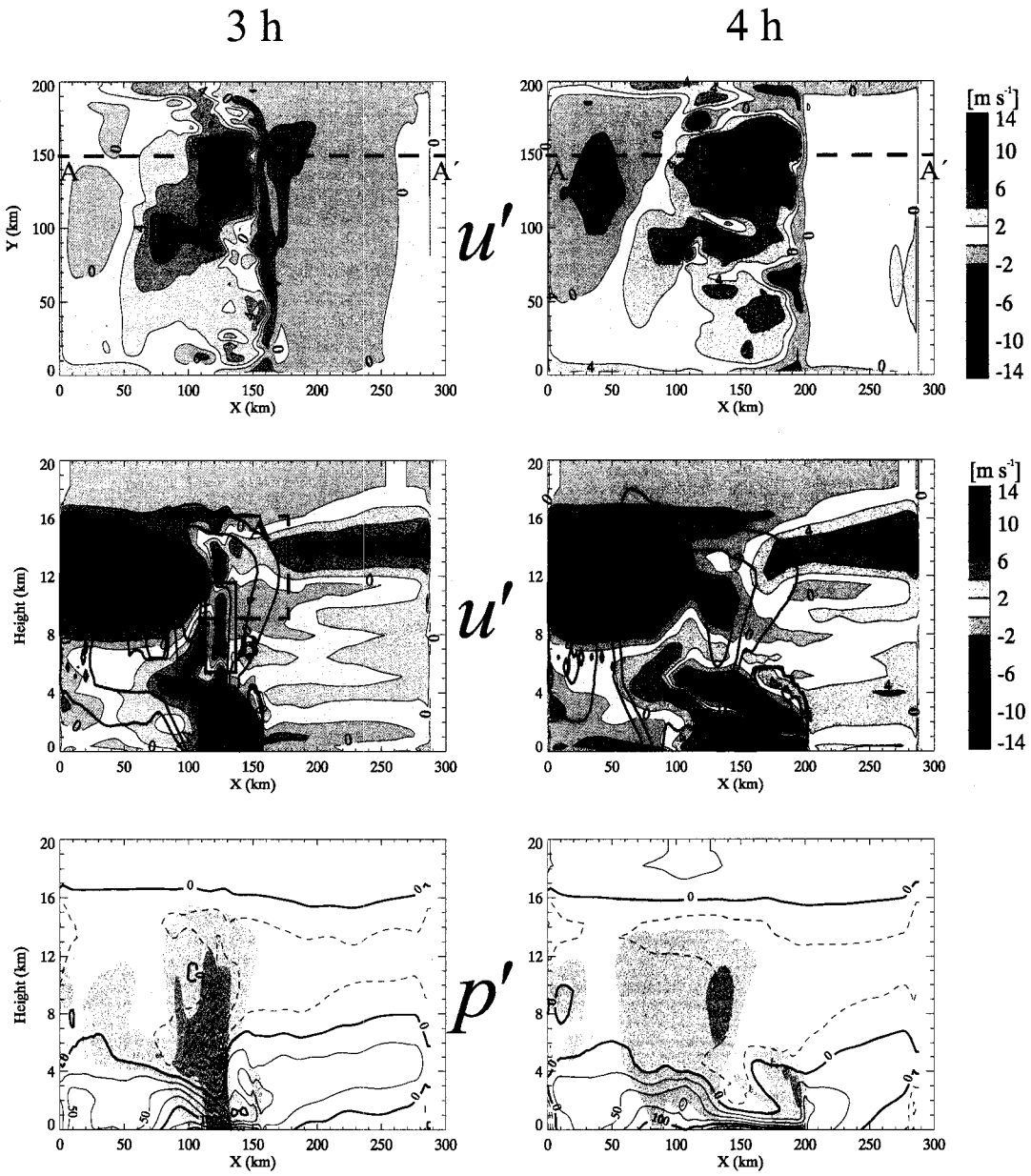


Figure 5.6. Cross sections of model quantities at hourly intervals from 3 h to 6 h for the 14 Dec. 1992 simulation. The top panels in each column show filled contours of perturbation zonal velocity $u'$, as defined in the text, taken through a horizontal cross section of height z=1 km. Middle panels are vertical cross sections of $u'$, taken through the dashed line A-A′ at y=150 km. (Continued…)

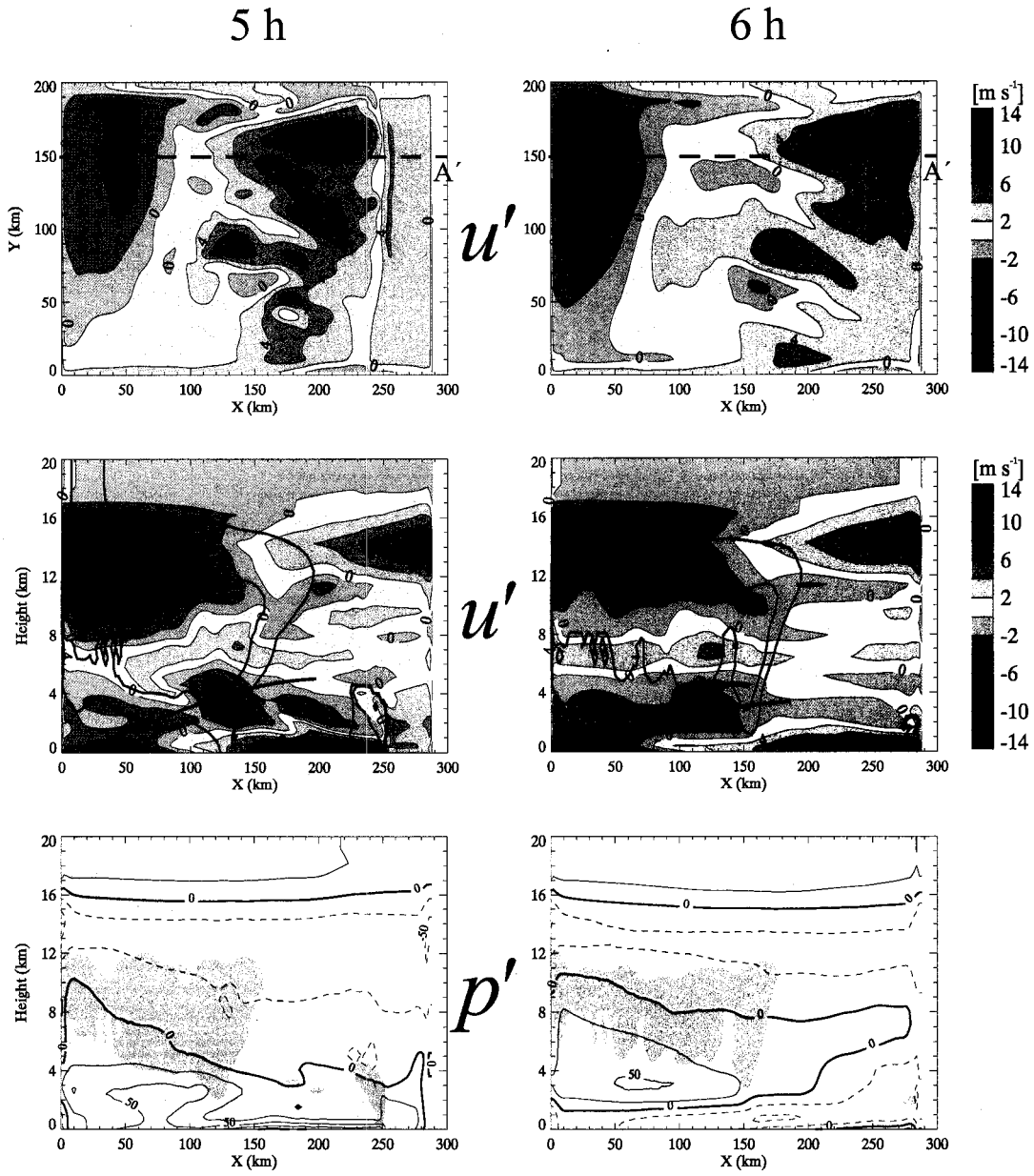


Figure 5.6. (Continued). The contour interval for $u'$ is 2 m $s^{-1}$, with shades of red indicating positive (westerly) perturbations and shades of blue negative (easterly) perturbations. Contours of the total hydrometeor content (contour levels of $10^{-5}$, $10^{-4}$, $10^{-3}$ kg $kg^{-1}$) are overlaid on the top and middle frames to indicate the general location of the convection. The lower frames show contours of perturbation pressure along A-A′, overlaid on shaded total hydrometeor content (levels of $10^{-5}$, $10^{-4}$, $10^{-3}$ kg $kg^{-1}$). The contour interval is 25 Pa. Boxes A and B are described in the text. Arrows emphasize perturbation flow.

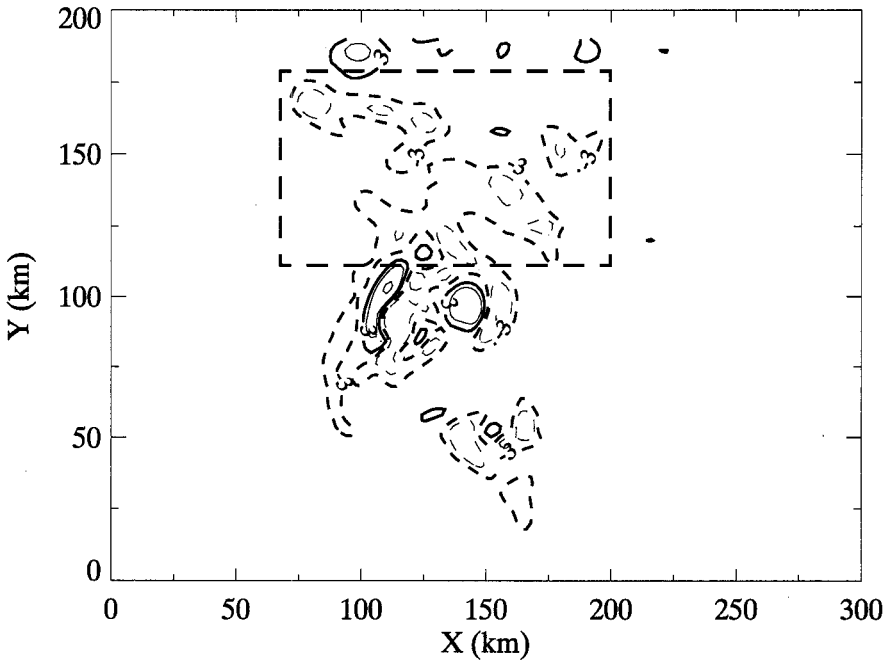


Figure 5.7. Horizontal cross section of the 30 minute time-mean (5-5.5 h) VAD momentum acceleration term taken at an altitude of 2.4 km for the 14 December 1992 simulation. Contour values are [-17, -7, -3, 3, 7, 17 m $s^{-1}$ $h^{-1}$]. The box emphasizes a region of organized downward transport of easterly momentum.

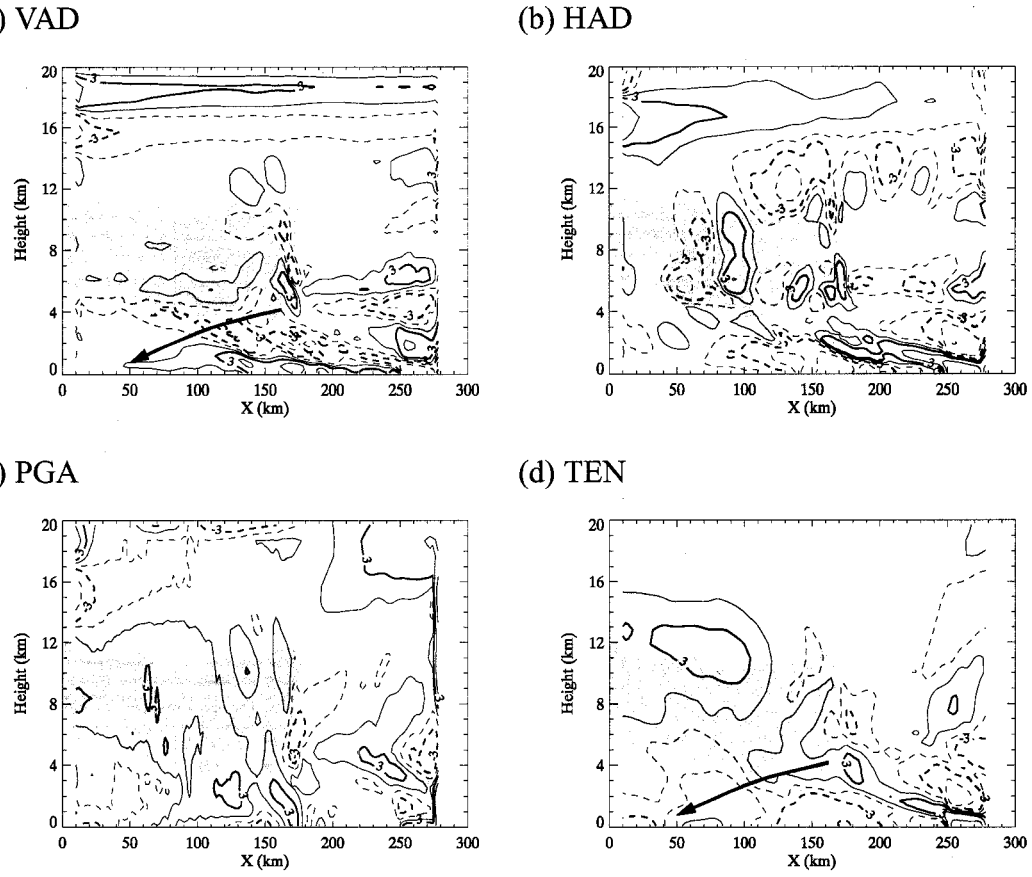


Figure 5.8. Vertical cross sections of 30 minute time-mean (5-5.5 h) momentum forcing terms for the 14 December 1992 simulation, averaged over a strip from y=120-160 km (Figure 5.6, top panels) overlaid on the total hydrometeor field ($10^{-5}$, $10^{-4}$, $10^{-3}$ kg $kg^{-1}$). (a) VAD; (b) HAD; (c) PGA; (d) TEN. Contour values are [-17, -7, -3, -1, 1, 3, 7, 17 m $s^{-1}$ $h^{-1}$]. Arrows indicating perturbation flow are superimposed over the forcings.

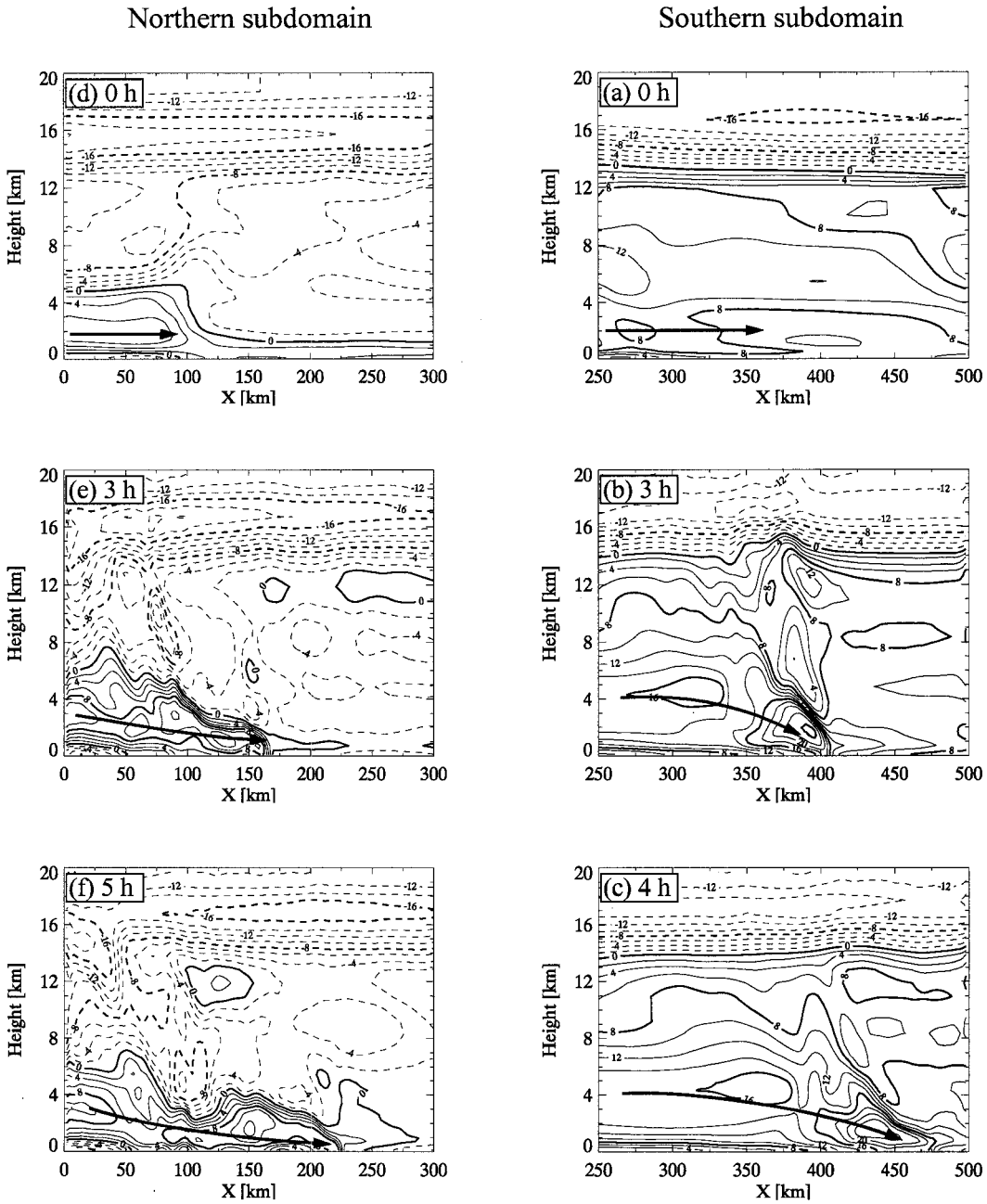


Figure 5.9. Cross sections of zonal velocity, $u$, for the 23-24 December 1992 experiment for the indicated times. The cross sections are taken through NN–NN′ and SS–SS′ in the northern and southern subdomains of Figure 5.4. Arrows emphasize descending mid-level inflow layer

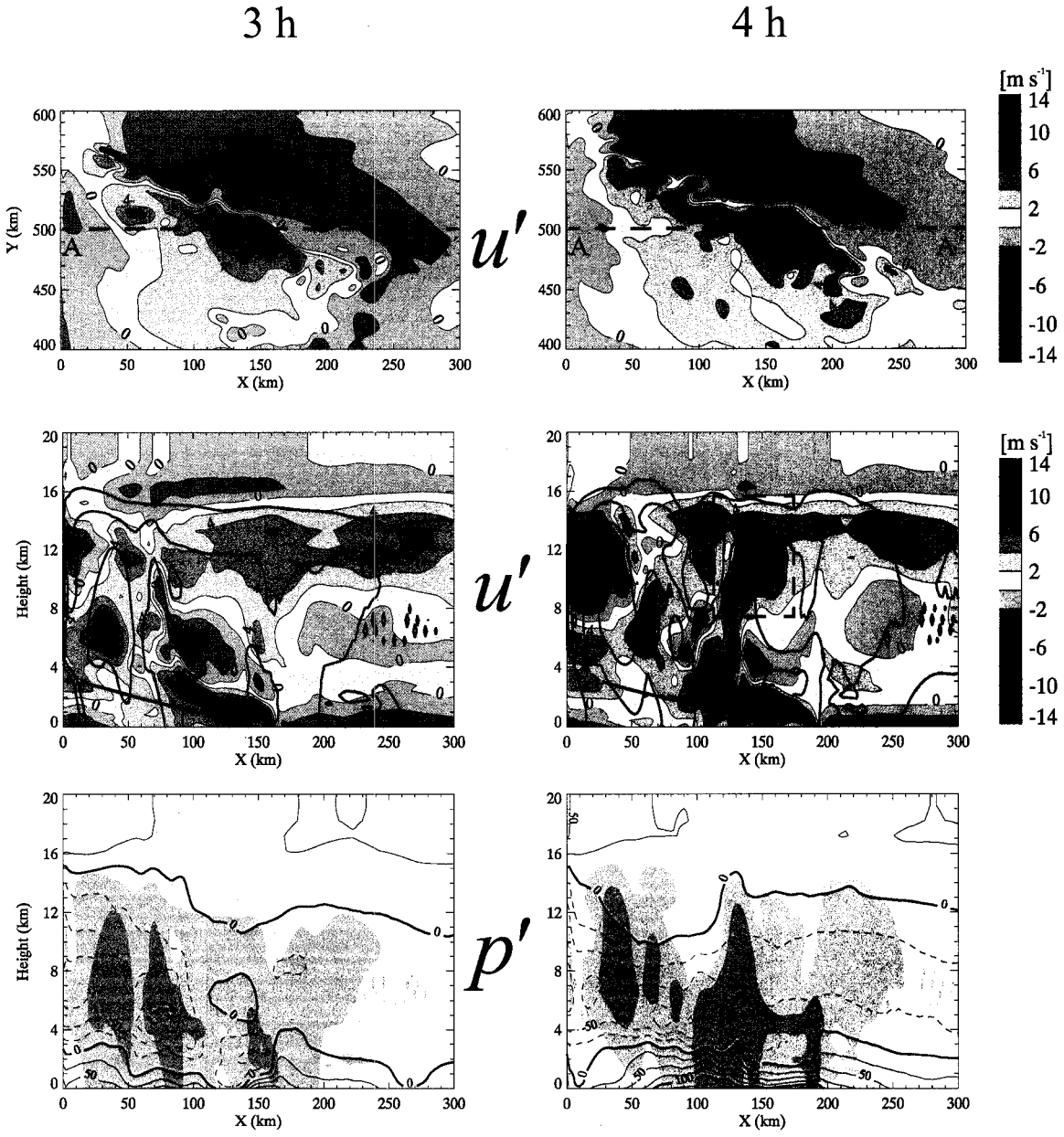


Figure 5.10. Cross sections of model quantities at hourly intervals from 3 h to 5 h over the northerly "N" (shown on Figure 5.4) for the 23-24 Dec. 1992 simulation. The top panels in each column show filled contours of perturbation zonal velocity $u'$, as defined in the text, taken through a horizontal cross section of height z=1 km. Middle panels are vertical cross sections of $u'$, taken through the dashed line A-A′ at y=500 km. (Continued…).

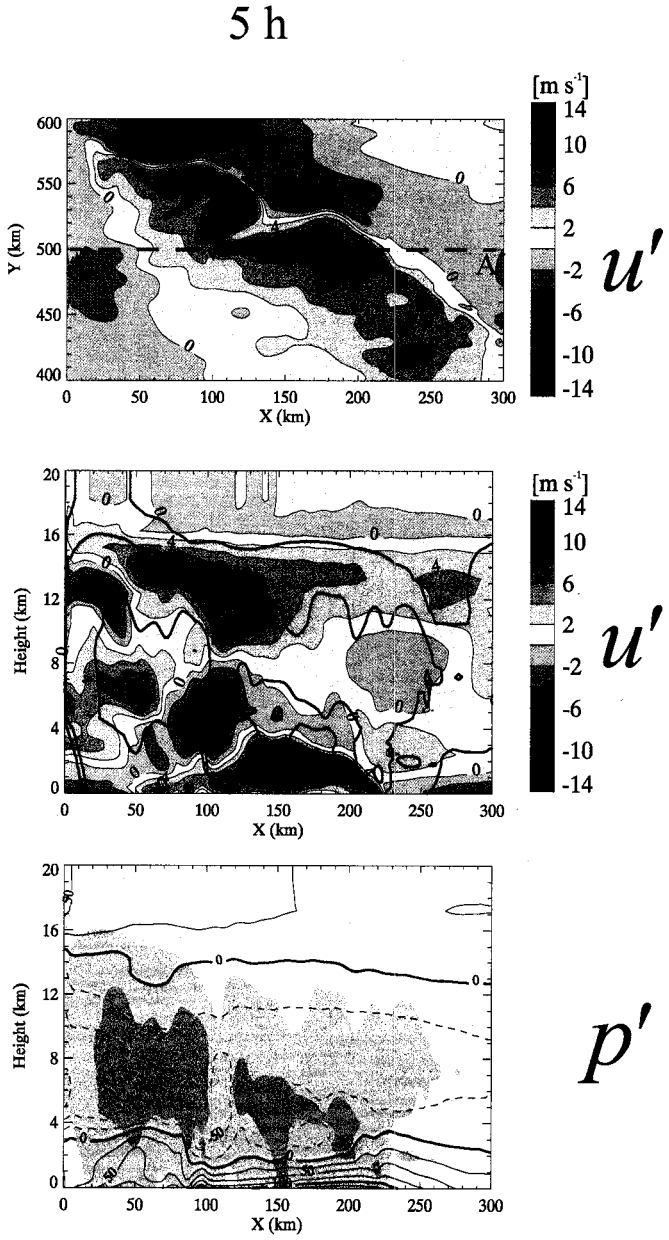


Figure 5.10. (Continued). The contour interval for $u'$ is 2 m $s^{-1}$, with shades of red indicating positive (westerly) perturbations and shades of blue negative (easterly) perturbations. Contours of the total hydrometeor content (contour levels of $10^{-5}$, $10^{-4}$, $10^{-3}$ kg $kg^{-1}$) are overlaid on the top and middle frames to indicate the general location of the convection. The lower frames show contours of perturbation pressure along A-A′, overlaid on shaded total hydrometeor content (levels of $10^{-5}$, $10^{-4}$, $10^{-3}$ kg $kg^{-1}$). The contour interval is 25 Pa. The dashed boxes are described in the text. Arrows emphasize perturbation flow.

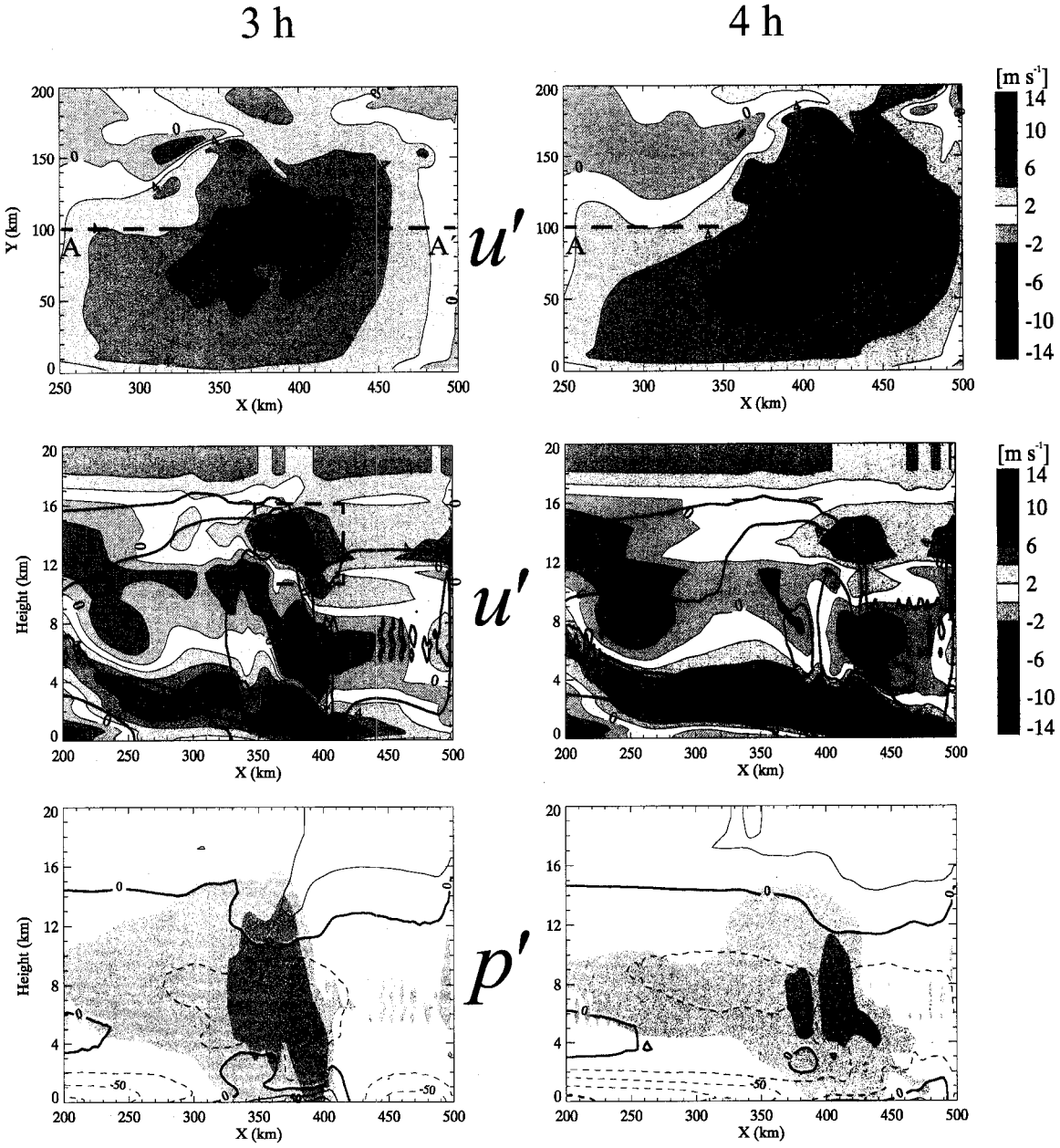


Figure 5.11. As in Figure 5.10, but taken at 3 h and 4 h over the southerly subdomain "S" (shown in Figure 5.4) for the 23-24 Dec. 1992 simulation. Cross section is taken through y = 100 km.

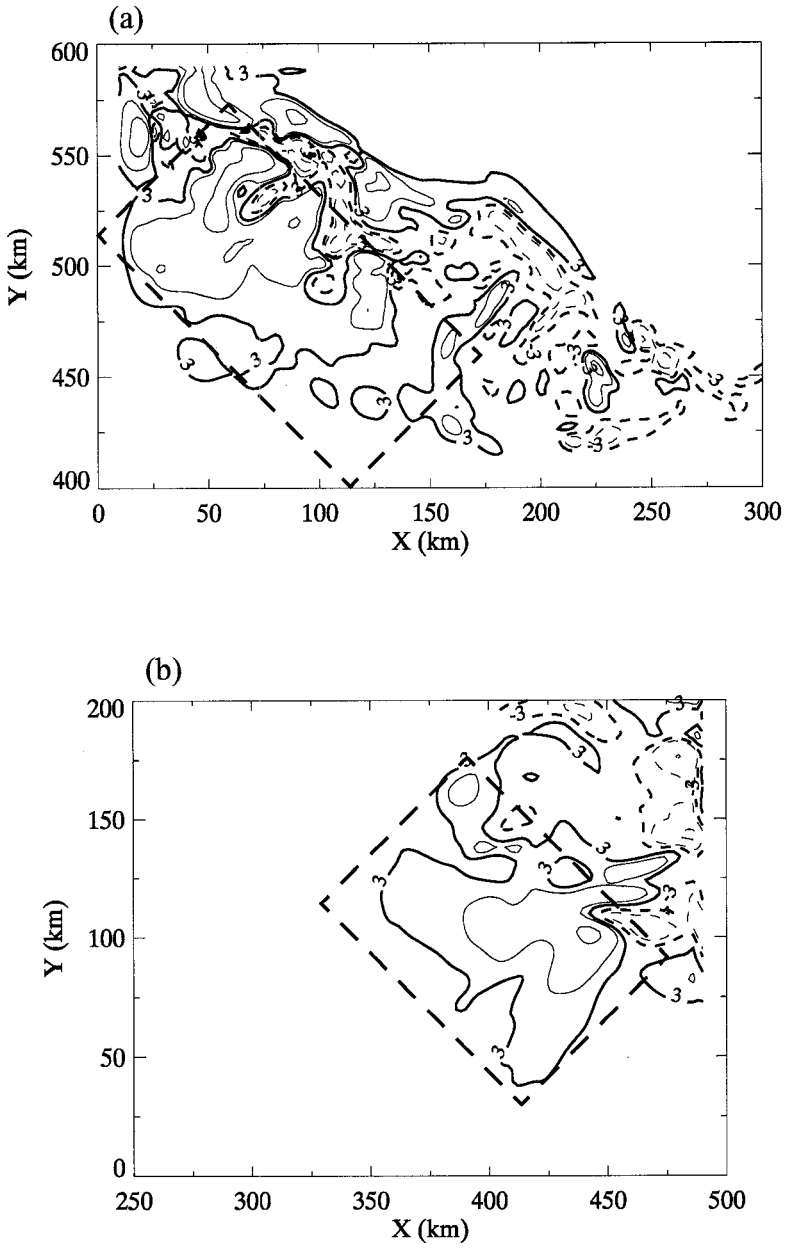


Figure 5.12. Horizontal cross section of the 30 minute time-mean (4.5-5 h) VAD momentum acceleration term taken at an altitude of 1 km for the 23-24 December 1992 simulation. (a) Northern subdomain. (b) Southern subdomain. Contour values and units are as in Fig. 5.7. The boxed region emphasizes organized downward transport of westerly momentum.

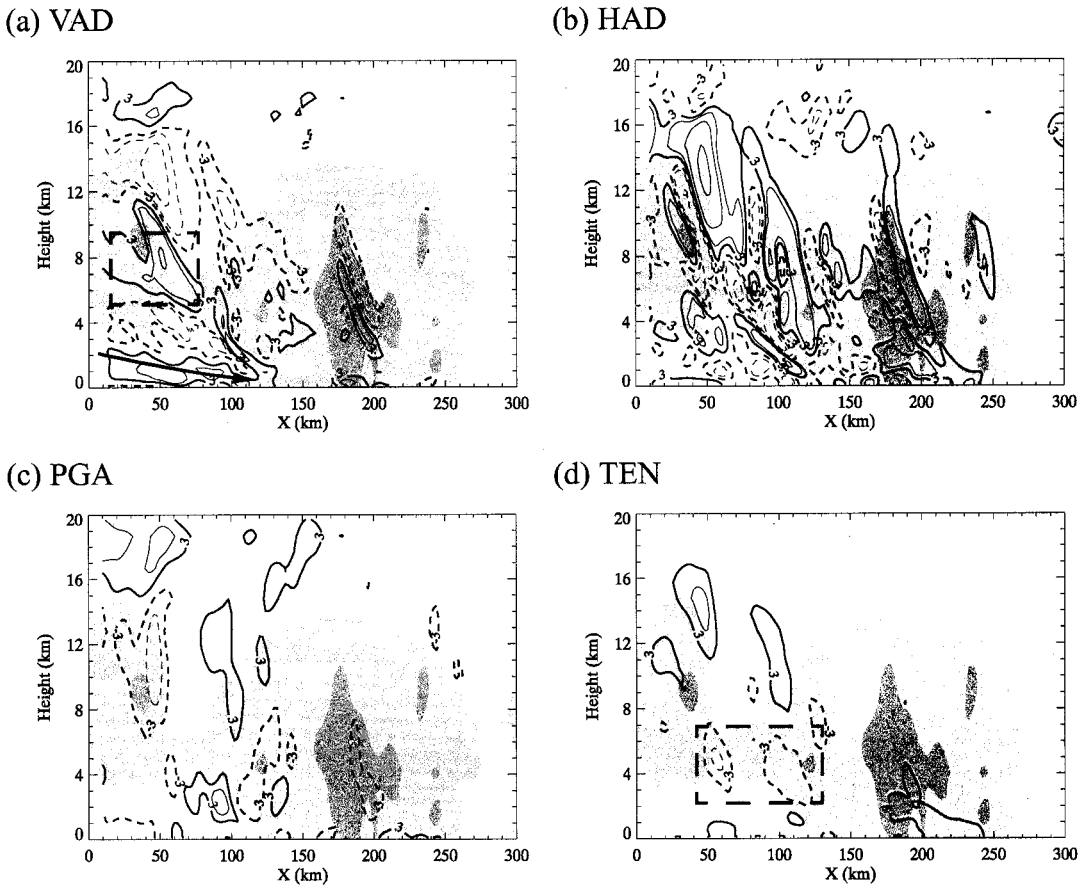


Figure 5.13. Vertical cross sections of 30 minute time-mean (4.5-5 h) momentum forcing terms for the 23-24 December 1992 simulation, averaged over a 50 km-wide strip centered at y = 500 km in the northern subdomain (Figure 5.10, top panels) overlaid on the total hydrometeor field ($10^{-5}$, $10^{-4}$, $10^{-3}$ kg kg$^{-1}$). (a) VAD; (b) HAD; (c) PGA; (d) TEN. Contour values and units are as in Figure 5.8. Boxed regions are alluded to in the text. An arrow indicating perturbation flow is superimposed over the VAD forcing.

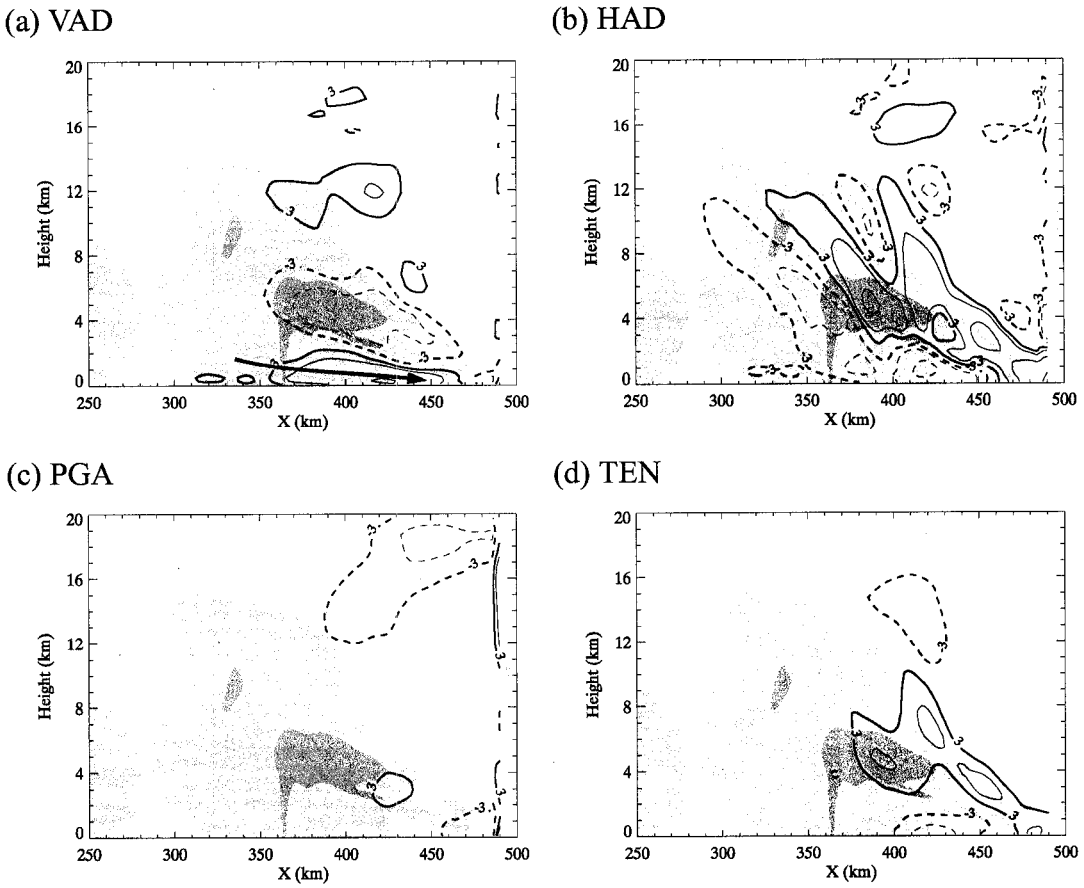


Figure 5.14. Vertical cross sections of 30 minute time-mean (4.5-5 h) momentum forcing terms for the 23-24 December 1992 simulation, averaged over a 50 km-wide strip centered at y = 100 km in the southern subdomain (Figure 5.11, top panels) overlaid on the total hydrometeor field ($10^{-5}$, $10^{-4}$, $10^{-3}$ kg kg$^{-1}$). (a) VAD; (b) HAD; (c) PGA; (d) TEN. Contour values and units are as in Figure 5.8. Boxed regions are alluded to in the text. An arrow indicating perturbation flow is superimposed over the VAD forcing.

(a) 14 Dec. 1992

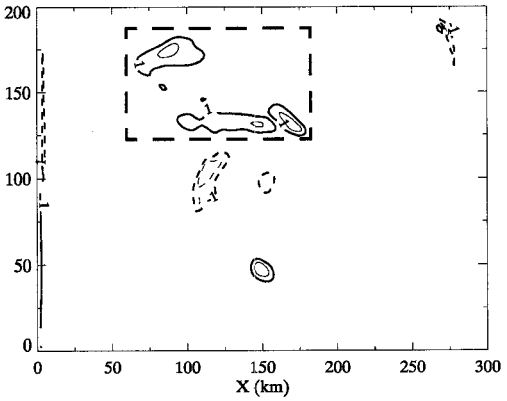


(b) 23-24 Dec. 1992 (Northern subdomain)

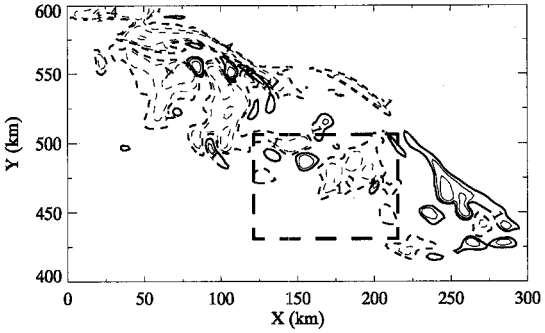


(c) 23-24 Dec. 1992 (Southern subdomain)

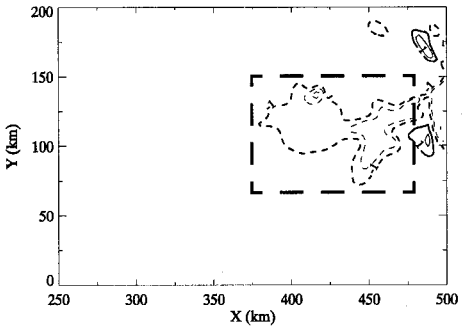


Figure 5.15. Horizontal cross sections of $w'u'$ at 5 h for both experiments. (a) 14 December 1992, taken at a height of 2.5 km. (b) and (c) 23-24 December 1992, over the northern and southern subdomains, at a height of 1 km. Contour values are [-16, -4, -2, -1, 1, 2, 4, 16 $m^2 s^{-2}$]. Boxes bound regions of $w'u'$, positive in (a) and negative in (b) and (c), thought characteristic for each flow regime.

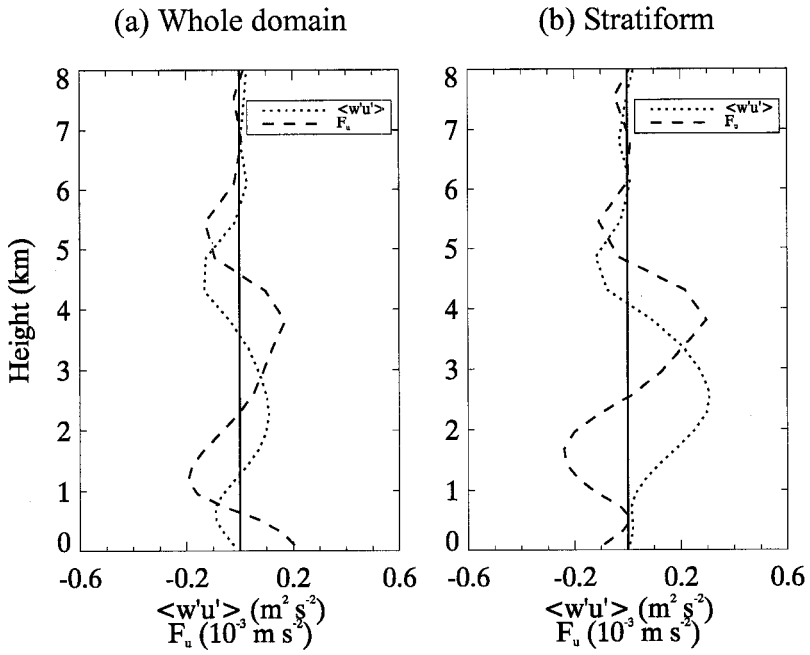


Figure 5.16. Vertical profiles of $\langle w'u' \rangle$ and $F_u = -\frac{\partial}{\partial z}\langle w'u' \rangle$ for the 14 December 1992 simulation at 5.5 h. Averages are taken over the indicated domains. (a) Entire model domain. (b) Stratiform region only. The stratiform region is similar to the region enclosed by the dashed box in Fig. 5.3h.

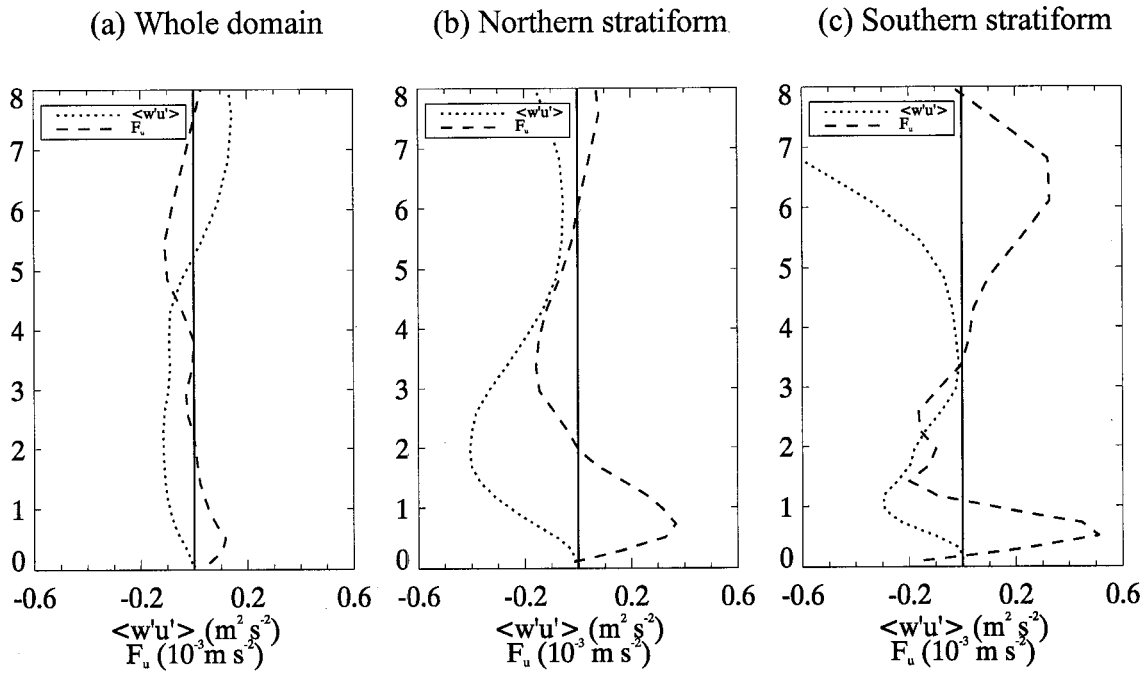


Figure 5.17. Vertical profiles of $\langle w'u' \rangle$ and $F_u = -\frac{\partial}{\partial z}\langle w'u' \rangle$ for the 23-24 December 1992 simulation at 5 h. Averages are taken over the indicated domains. (a) Entire model domain. (b) Stratiform region of the northern subdomain. (c) Stratiform region of the southern subdomain. The stratiform regions are denoted by the dashed boxes in Fig. 5.4f.

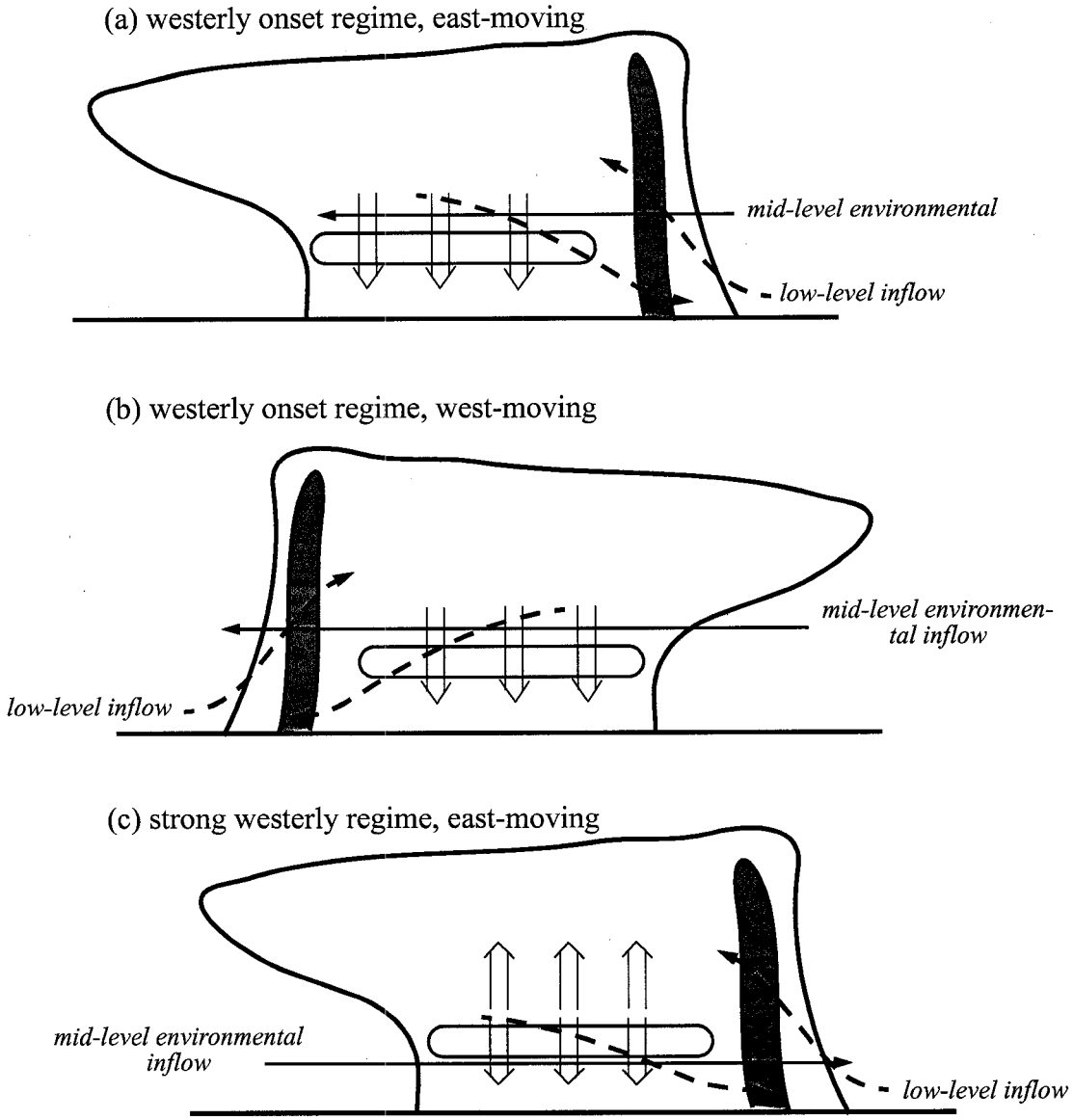


Figure 5.18. Conceptual cartoon for inflow momentum structure and generation. Darkly-shaded region represents active convection. Lightly-shaded region represents stratiform bright band. Horizontal arrow indicates mid-level environmental inflow, elevated easterlies over the westerly onset regime (a, b) and strong westerlies just off the surface in the strong westerly regime (c). Dashed lines are flows accelerated by system-generated pressure gradients. Broad arrows represent a broad region of mesoscale downdraft and updraft.

# Chapter 6

# Conclusions

## 6.1 Discussion

### 6.1.1 Nature of MCS inflow

Chapter 4 has shown that the frequently employed parcel model of tropical convection is not always applicable. Over the western Pacific warm pool, tropical oceanic convection frequently occurs in super clusters. Groups of very large mesoscale convective systems occur in the vicinity of each other and the inflow into one system may be influenced by the presence of one or more of its neighboring systems.

The parcel model envisages high $\theta_e$ air ascending from near the surface of the earth to great heights in entraining convective-scale bubbles or plumes. Air from just above the PBL, with lower $\theta_e$, mixes into convective downdrafts and sinks. The crossover zone (Zipser 1977) embodies this concept in the dynamics of an individual mesoscale system. This pure parcel view of convection does not always agree with Doppler radar data, which show that organized deep convective systems over the western tropical Pacific warm pool often have layers of ascending inflow ~0.5-4 km in depth (Kingsmill and Houze 1999a, b).

Trajectory analysis of the cloud model output gives insight into when and where parcel and layer lifting occurs in convection characteristic of that occurring over the western Pacific warm pool. The model simulation of a convective system occurring in an environment containing numerous preceding, pre-existing, and concurrently developing mesoscale convective systems (TOGA COARE 23 December case with unmodified environment) shows moistened air flowing into the mesoscale updraft in a pronounced layer-lifting configuration. In our control run (TOGA COARE 14 December case with unmodified environment), parcel convection prevails in the strong updrafts, and crossover-zone-like mixing occurs. Only the air in the lower part of the inflow actually rises in the deep convective updrafts of the mesoscale convective system. Model trajectory statistics for this experiment (TOGA COARE 14 December case with moistened environment) indicate

that a significant amount of air from the upper part of the inflow layer rises in the updraft along with air from just above the surface. That is, the layer-lifting theory better describes the convective updrafts.

The model calculations show that a moist midlevel region is associated with the layer-lifting mode of inflow. Mechanisms are proposed to explain how this moistening might occur in nature. In the first hypothesized mechanism, inflow air undergoes vertical mixing by moderate cumulus and cumulonimbus (Johnson et al. 1999) before entering the updraft of the system. This process would moisten the layer and furthermore render it approximately moist neutral, since the midlevel $\theta_e$ would be increased. In the second proposed mechanism, evaporation of pre-existing stratiform rain, acting in concert with stratiform subsidence, increases the humidity of the inflow layer without a major change in its dry static stability. This mechanism does not change the layer $\theta_e$. Radar data presented in this dissertation (Figs. 4.18 and 4.19) and the ubiquity of active phase convection in the satellite record provide evidence that this mechanism is a possible if not likely source of midlevel moistening. Regardless of the exact mechanism responsible for the moistening, the increased humidity and nearly moist adiabatic lapse rate imply that when the inflow layer meets the cold pool it quickly reaches saturation and the relevant static stability becomes the moist static stability. Then the inflow layer responds to the lifting by the leading edge of the cold pool as a nearly moist neutral layer and is easily lifted over it. Thus layer lifting is favored when the inflow layer has been moistened and has also attained uniform (and possibly elevated) $\theta_e$.

Results are consistent with the midlatitude MCS layer inflows investigated by Bryan and Fritsch (2000), who argue that regions of moist absolutely unstable layers (MAULs) are symptomatic of deep, layer-like inflows. MAULs in the present study are of similar spatial extent and temporal duration. Requiring a MAUL for layer inflow appears to be a rather strict condition, and our results indicate that a MAUL is a sufficient but not necessary condition to produce the layer mode — moist neutral conditions should also produce an organized layer pattern. The mechanism envisioned by Bryan and Fritsch to produce the layer mode is weak, organized mesoscale ascent experienced by the inflow

prior to reaching the convective region. Although their mechanism is different from the two suggested in this study, the final result, achieving a condition of saturation or near-saturation through a deep layer, is strikingly similar.

The simulations further suggest that the cold pool itself changes significantly when the inflow layer is moistened. The pressure perturbation pattern resulting from the formation of the cold pool of the mesoscale convective system has an influence on the nature of the inflow. The environmental moisture field affects the pressure perturbation field through the degree of hydrometeor evaporation and subsequent cold pool strength. Enhanced midlevel moisture results in a weaker cold pool and is associated with a weaker pressure gradient and weaker rear-to-front flow. In the control case (drier environment), evaporative cooling is stronger through a deeper layer, and the resulting rear-to-front velocities are strong over a deeper layer relative to the enhanced-moisture run, appearing to "block" the front-to-rear inflow and preventing the establishment of a sloping layer-type updraft.

Moistening the inflow layer (while retaining its dry static stability) affects both the cold pool itself and the ability of the inflow to respond to the cold pool. The moistened inflow leads to a weaker, shallower cold pool, less inclined to block the inflow. At the same time the higher humidity allows the air trying to rise over the cold pool to quickly saturate so that the reference lapse rate in the static stability changes to the moist adiabat, and the whole layer is more easily able to rise over the cold pool barrier.

Only portions of mesoscale convective systems occurring under specified thermodynamic and flow regimes have been investigated in this study, and the spatial and temporal domain of the simulated convection is only a subset of the domain of the entire mesoscale convective system. For the first proposed moistening mechanism, a robust region of stratiform precipitation along the inflow path is vital; for the second, moderate convection is required. Under the proposed mechanisms, not only is the concurrent presence of stratiform precipitation and active moderate convection important, so too is the temporal development of the ongoing convective population in the region. For moistening to occur, an initially dry inflow layer might pass through a region of precipitation from

older, decaying convection along its path into a newer, more vigorous system. It might also pass through moderate convection that is precursor to a future mesoscale system. The simulations and the observations both support the idea that, to support this moistening, the convection must both contain a significant region of stratiform precipitation in its own right but must also be at least a "second generation" system in that the presence of the decaying convection as well as developing convection is necessary to moisten the inflow. This implies a degree of organization, in both time and space, which is beyond the convective/stratiform structure of a single mesoscale cloud system. The response of the simulated convection to an increase in the midlevel relative humidity should be thought of as both a sensitivity to large-scale environmental conditions and a sensitivity to the degree of mesoscale organization. By moistening the midlevels, the importance of organized mesoscale flow has been implicitly acknowledged.

The nature of MCS inflow is portrayed in this paper as being either parcel/crossover or layer-like. These two seemingly dichotomous terms describe not the process of convective overturning but rather its physical manifestation. Between the two pure modes (crossover and layer) may exist a spectrum of possibilities. The stochastic nature of the conceptual model could account for an entire spectrum of solutions between the two modes discussed, the result of which is tied to ambient conditions and the degree of mesoscale organization. The fact that $w'\theta_e' > 0$, which marks a strong signal of overturning in the control case, is also evident in the enhanced moisture experiment indicates that a similar process may be occurring, even though the bulk behavior of the inflow air in the two cases is significantly different. In this context, the layer lifting mode might be considered as a logical extension of the stochastic aspect of the conceptual model (Zipser 1977), even though the physical manifestations of the overturning process differ.

### 6.1.2 Character of MCS momentum transport

Chapter 5 discusses the potential impact of simulated momentum transports on the large scale Kelvin-Rossby wave structure. In a simulation representing the westerly onset phase of the ISO, midlevel easterly momentum is brought downward by the stratiform region and acts to counter to the low level westerlies which the propagating wave pattern

is attempting to establish, and though the domain size is too small to be determined conclusively, it may be inferred that the resulting enhanced low level convergence triggers new cells on the side of the convection opposite its direction of propagation. The increase in low level westerlies effected by MCS vertical transports and pressure acceleration during the strong westerly simulation would act as a positive feedback on the KR wave pattern.

The mechanisms proposed to explain the large scale Kelvin-Rossby wave structure and the MJO generally rely on parameterizations to represent convection and hence do not explicitly resolve the organized tropical MCSs investigated in this study. The mechanisms in these theories are quite sensitive to the particular parameterization used. The behavior of warm pool convection is complex, with momentum transport signals which can be quite different from convective to stratiform region. When thinking about these studies, it is fitting to be curious about the effect on the character of the large scale wave pattern of treating the convection as a simple response to moisture convergence or as a series of entraining plumes. This study suggests that the momentum transport character of the convection is modulated by the degree of mesoscale organization attained, which implies that an entraining plume model (for example) might miss aspects of the convection related to its mesoscale organization.

The real atmosphere has complications not found in the idealized Gill (1980) model which likely arise from the nonstationarity of the wave pattern and the distribution of heating imposed by the convection on the large scale atmosphere. The pattern of latent heating is significantly dependent upon the degree of mesoscale organization, meaning horizontally extensive regions of significant stratiform precipitation and mesoscale circulations (Houze et al. 2000). Compared to widespread convective cells, a large MCS will have its maximum heating at higher levels, since the broad region of stratiform precipitation is characterized by a deep layer of cooling at lower levels. So too is the momentum transport dependent upon the degree of mesoscale organization. Organized convection is able to generate significant momentum which can then be transported, along with the

momentum of the large scale environment, downward by the expansive regions of mesoscale descent associated with the stratiform precipitation area.

## 6.2 Synthesis

This study should be thought of as exploratory rather than absolutely conclusive, and due caution must be taken so as not to draw overreaching conclusions from the numerical simulations. In the observed tropical atmosphere, midlevel environmental humidity is systematically correlated with breadth and depth of convection and to a certain extent its overall degree of mesoscale organization. Kingsmill and Houze (1999a, b) demonstrate this and the prevalence of the layer mode of inflow into organized convection. However, they do not provide definitive proof that the two (enhanced midlevel humidity and layer inflow) are linked. The mode of inflow in this study appears to be strongly correlated with midlevel environmental humidity. Increasing midlevel humidity so that it is more reflective of an environment supporting organized convection brings about the layer mode, and the simulation executed with a pre-moistened environment exhibits a strong layer mode signal.

This study shows that midlevel humidity is likely correlated with the nature of the inflow. A separate and prerequisite issue is how this moistening comes about, and two possible mechanisms are proposed in this study. The inflow might pass through a region of stratiform precipitation or through a region of moderate-depth cumulus. The first mechanism seems plausible, given the ubiquity of convection during the westerly onset and strong westerly phases. Indeed, looking at the satellite record, it would be difficult to deny that this occurs. Would this process be able to produce the systematic moistening present in the observations? This study cannot answer that question. Both proposed mechanisms moisten the midlevels, though only the cumulus increases the midlevel $\theta_e$ in a manner fully consistent with the observations.

As stated in Section 6.1.1, the terms "crossover" and "layer" are simply the physical manifestations of the overturning of the environment, but it is difficult to infer which is a more efficient means of overturning. The layer mode indicates a horizontal scale of

overturning larger than that of the crossover zone. The crossover zone is associated with convective scale updraft and downdraft couplets spaced some distance apart, while the overturning in the layer inflow occurs over a broad sheet of air and implies a substantial degree of mesoscale organization. The more *organized* overturning of the layer mode probably implies a more *extensive* overturning but not necessarily a more *efficient* one. If the second proposed mechanism is to be believed, the inflow has already experienced some degree of shallow overturning, leaving less to be accomplished by the deep convection. Perhaps that is one reason why the overturning in the layer mode is more gradual than the parcel/crossover mode, since it is characterized by less violent mixing between parcels of different $\theta_e$.

This dissertation has demonstrated that, in addition to actuating an organized mode of thermodynamic overturning, highly organized convection also has a significant effect on the momentum fields. The simulated MCSs develop extensive regions of weak, organized stratiform descent, which is able to transport midlevel momentum downward. In nature, the midlevel jets appear to undergo pressure gradient accelerations, which enhances the jet momentum and the resulting vertical transport. This enhancement effect is present in the simulated convection only to a limited degree. Large scale downward motion causes the momentum to descend in a manner analogous to the layer mode of the low level inflow. Certainly the midlevel inflow layer is not undergoing significant overturning as it descends, but the form of the descending structure can be best described as layer-like.

The low and midlevel inflows seem linked to the large scale environment differently. Low level layer inflow which ascends into the convective regions appears to be most closely associated with the thermodynamic overturning of the environment, a result that makes sense given the fact that the high $\theta_e$ air at low levels are the primary fuel (ignoring cloud top radiative cooling) for the convection. Midlevel inflow layers undergoing descent in regions of stratiform are tied to momentum redistribution of the environment. This is made possible to a significant degree by the collocation in height of peak MCS stratiform descent with the environmental jet maximum.

The momentum vertical transport signals demonstrated over the stratiform region seem reasonably robust for both Kelvin-Rossby flow regimes. Enough drawbacks are present in the methodology that the net MCS character cannot be determined from these simulations. Furthermore, since both easterly and westerly low level layer inflows have been shown to occur in nature, it is likely that the momentum transport will be dependent upon the direction of low level system-relative inflow. For example, the simulated 14 December 1992 system discussed in Chapter 5 had exhibited low level inflow from the east, while systems observed on that day had inflows from both the west and the east. In the best observed system, with inflow from the west, the easterly midlevel inflow appeared to experience an acceleration as it was descending, likely a response to system-generated pressure gradient. The simulated system, with its easterly inflow, experienced a westerly pressure acceleration, opposite to that observed but in agreement with MCS theory. The system-generated "rear" inflow was a different sign than the midlevel environmental inflow. The previous argument that the systems with westerly inflow tended to occur in the later, more organized stages of the MCS, seems to extend here to the possibility that a more mature MCS will have a less ambiguous momentum transport signal than a corresponding young piece of convection.

Applying the methodology used in this study to understand upscale feedbacks is predominantly a matter of inference. The inferences can be well reasoned, but they remain inferences and are limited because they are often inconclusive. The momentum transport portion of this work is subject to this criticism — that, while stratiform MCS transports are shown to be in significant agreement with observations, the experimental framework is unable to show conclusively the *net* MCS effects. It is likely that a methodology that encompasses a larger spatial domain would overcome this problem.

# References

Betts, A. K., 1976: The thermodynamic transformation of the tropical subcloud layer by precipitation and downdrafts. *J. Atmos. Sci.*, **33**, 1008-1020.

Biggerstaff, M. I., and R. A. Houze, Jr., 1991; Kinematic and precipitation structure of the 10-11 June 1985 squall line. *Mon. Wea. Rev.*, **119**, 3034-3065.

Biggerstaff, M. I., and R. A. Houze, Jr., 1993: Kinematics and microphysics of the transition zone of the 10-11 June 1985 squall line. *J. Atmos. Sci.*, **50**, 3091-3110.

Bougeault, P., P. Binder, A. Buzzi, R. Dirks, R. Houze, J. Kuettner, R. B. Smith, R. Steinacker, Hans Volkert, and all MAP scientists, 2000: The MAP Special Observing Period. *Bull. Amer. Meteor. Soc.*, **82**, 433-462.

Braun, S. A., and R. A. Houze, Jr., 1994: The transition zone and secondary maximum of radar reflectivity behind a midlatitude squall line: Results retrieved from Doppler radar data. *J. Atmos. Sci.*, **51**, 2733-2755.

Brown, R. G., 1994: A modeling and observational study of convective interaction with large-scale dynamics in the tropics. Ph. D. thesis, University of Washington, 193 pp.

Bryan, G. H., and J. M. Fritsch, 2000: Moist absolute instability: The sixth static stability state. *Bull. Amer. Meteor. Soc.*, **81**, 1207-1230.

Byers, H. R., and R. R. Braham, Jr., 1949: *The Thunderstorm*. U. S. Government Printing Office, Washington, D. C., 287 pp.

Carr, M. T. and C. S. Bretherton, 2001a: Convective momentum transport over the tropical Pacific: Budget estimates. *J. Atmos. Sci.*, **58**, 1673-1693.

Carr, M. T., and C. S. Bretherton, 2001b: Convective momentum transport over the tropical Pacific: Dual-Doppler. *J. Atmos. Sci.*, submitted.

Chen, S. S., R. A. Houze, Jr., and B. E. Mapes, 1996: Multiscale variability of deep convection in relation to large-scale circulation in TOGA COARE. *J. Atmos. Sci.*, **53**, 1380-1409.

Chen, S. S., 1997: Convectively active and suppressed periods in TOGA COARE. Preprints, *22nd Conference on Hurricanes and Tropical Meteorology*, Ft. Collins, CO, American Meteorological Society 583-586.

Davies, H., 1983: Limitations of some common lateral boundary schemes used in regional NWP models. *Mon. Weather Rev.*, **111**, 1002-1012.

Doty, K. G., and D. J. Perkey, 1993: Sensitivity of trajectory calculations to the temporal frequency of wind data. *Mon. Weather Rev.*, **121**, 387-401.

Emanuel, K. E., 1987: An air-sea interaction model of intraseasonal oscillations in the Tropics. *J. Atmos. Sci.*, **44**, 2324-2340.

Emanuel, K. E., 1994: *Atmospheric Convection*. Oxford Univ. Press., New York, 580 pp.

Fovell, R. G., and Y. Ogura, 1988: Numerical simulation of a midlatitude squall line in two dimensions. *J. Atmos. Sci.*, **45**, 3846-3879.

Gill, A., 1980: Some simple solutions for heat-induced tropical circulation. *Quart. J. Roy. Meteor. Soc.*, **106**, 447-462.

Godfrey, J. S., R. A. Houze, Jr., R. H. Johnson, R. Lukas, J.-L. Redelsperger, A. Sumi, and R. Weller, 1998: COARE: An interim report. *J. Geophys. Res.*, **103**, Vol. 7-Special TOGA issue, 14,395-14,450.

Grell, G., J. Dudhia, and D. R. Stauffer, 1994: *A description of the fifth-generation Penn State/ NCAR mesoscale model (MM5)*. NCAR Technical Notes, NCAR/TN-398+STR, 138 pp.

Harrison, D. E., and B. S. Giese, 1991: Episodes of surface westerly winds as observed from islands in the western tropical Pacific. *J. Geophys. Res.*, **96**, 3221-3237.

Houze, R. A., Jr., 1993: *Cloud dynamics*. Academic Press, San Diego, 573 pp.

Houze, R. A., Jr., 1997: Stratiform precipitation in regions of convection: A meteorological paradox? *Bull. Amer. Meteor. Soc.*, **78**, 2179-2196.

Houze, R. A., Jr., and C.-P. Cheng, 1977: Radar characteristics of tropical convection observed during GATE: mean properties and trends over the summer season. *Mon. Wea. Rev.*, **105**, 964-980.

Houze, R. A., Jr., and E. N. Rappaport, 1984: Air motions and precipitation structure of an early summer squall line over the eastern tropical Atlantic. *J. Atmos. Sci.*, **41**, 553-574.

Houze, R. A., Jr., S. S. Chen, D. E. Kingsmill, Y. Serra, and S. E. Yuter, 2000: Convection over the Pacific warm pool in relation to the atmospheric Kelvin-Rossby wave. *J. Atmos. Sci.*, **57**, 3058-3089.

Hu, Q., and D. A. Randall, 1994: Low-frequency oscillations in radiative-convective systems. *J. Atmos. Sci.*, **51**, 1089-1099.

Johnson, R. H., T. M. Rickenbach, S. A. Rutledge, P. E. Ciesielski, and W. H. Schubert, 1999: Trimodal characteristics of tropical convection. *J. Climate*, **12**, 2397-2418.

Jorgensen, D. P., M. A. LeMone, and B. J.-D., Jou, 1991: Precipitation and kinematic structure of an oceanic mesoscale convective system. Part I: Convective line structure. *Mon. Wea. Rev.*, **119**, 2608-2637.

Kingsmill, D. E., and R. A. Houze, Jr., 1999a: Kinematic characteristics of air flowing into and out of precipitating convection over the west Pacific warm pool. *Quart. J. Roy. Meteor. Soc.*, **125**, 1165-1207.

Kingsmill, D. E., and R. A. Houze, Jr., 1999b: Thermodynamic characteristics of air flowing into and out of precipitating convection over the west Pacific warm pool. *Quart. J. Roy. Meteor. Soc.*, **125**, 1209-1229.

Klemp, J. B., and R. B. Wilhelmson, 1978: The simulation of three-dimensional convective storm dynamics. *J. Atmos. Sci.*, **35**, 1070-1096.

Leary, C. A., and R. A. Houze, Jr., 1979: The structure and evolution of convection in a tropical cloud cluster. *J. Atmos. Sci.*, **36**, 437-457.

LeMone, M. A., 1983: Momentum transport by a line of cumulonimbus. *J. Atmos. Sci.*, **40**, 1815-1834.

LeMone, M. A., and M. W. Moncrieff, 1994: Momentum and mass transport by convective bands: Comparison of highly idealized dynamical models to observations. *J. Atmos. Sci.*, **51**, 281-305.

LeMone, M. A., G. M. Barnes, and E. J. Zipser, 1984: Momentum flux by lines of cumulonimbus over the tropical oceans. *J. Atmos. Sci.*, **41**, 1914-1932.

Lin, X., and R. H. Johnson, 1996: Kinematic and thermodynamic characteristics of flow over the western Pacific warm pool during TOGA COARE. *J. Atmos. Sci.*, **53**, 695-715.

Lin, Y.-L., R. D. Farley, and H. D. Orville, 1983: Bulk parameterization of the snow field in a cloud model. *J. Clim. Appl. Meteor.*, **22**, 1065-1092.

Lindzen, R. S., 1974: Wave-CISK in the Tropics. *J. Atmos. Sci.*, **31**, 156-179.

Locatelli, J. D., and P. V. Hobbs, 1974: Fall speeds and masses of solid precipitation particles. *J. Geophys. Res.*, **79**, 2185-2197.

López, R. E., 1976: Radar characteristics of the cloud populations of tropical disturbances in the northwest Atlantic. *Mon. Wea. Rev.*, **104**, 269-283.

López, R. E., 1977: The lognormal distribution and cumulus cloud populations. *Mon. Wea. Rev.*, **105**, 865-872.

Lucas, C. E., and E. J. Zipser, 2000: Environmental variability during TOGA COARE. *J. Atmos. Sci.*, **57**, 2333-2350.

Lucas, C., E. J. Zipser, and B. S. Ferrier, 2000: Sensitivity of tropical west Pacific oceanic squall lines to tropospheric wind and moisture profiles. *J. Atmos. Sci.*, **57**, 2351-2373.

Madden, R., and P. Julian, 1971: Detection of a 40-50 day oscillation in the zonal wind in the tropical Pacific. *J. Atmos. Sci.*, **28**, 702-708.

Madden, R., and P. Julian, 1972: Description of global scale circulation cells in the Tropics with a 40-50-day period. *J. Atmos. Sci.*, **29**, 1109-1123.

Maddox, R. A., 1980: Mesoscale convective complexes. *Bull. Amer. Meteor. Soc.*, **61**, 1374-1387.

Mapes, B. E., 2001: Water's two scale heights: the moist adiabat and the radiative tropopause. *Quart. J. Roy. Meteor. Soc.*, **127**, 2353-2366.

Mapes, B. E., and R. A. Houze, Jr., 1993: Cloud clusters and superclusters over the oceanic warm pool. *Mon. Weather Rev.*, **121**, 1398-1415.

Mapes, B. E., and X. Wu, 2001: Convective eddy momentum tendencies in long cloud-resolving model simulation. *J. Atmos. Sci.*, **58**, 517-526.

Matsuno, T., 1966: Quasi-geostrophic motions in the equatorial area. *J. Meteor. Soc. Japan*, **44**, 25-43.

McCumber, M., W.-K. Tao, J. Simpson, R. Penc, and S.-T. Soong, 1991: Comparison of ice-phase microphysical parameterization schemes using numerical simulations of tropical convection. *J. Appl. Meteor.*, **30**, 985-1004.

Mechem, D. B., R. A. Houze Jr., and S. S. Chen, 2001: Layer inflow into precipitating convection over the western tropical Pacific, *Quart. J. Roy. Meteor. Soc.*, **128**, 1997-2030.

Moncrieff, M. W., 1992: Organized convective systems: Archetypal dynamic models, mass and momentum flux theory, and parameterization. *Quart. J. Roy. Meteor. Soc.*, **118**, 819-850.

Moncrieff, M. W., and E. Klinker, 1997: Organized convective systems in the tropical western Pacific as a process in general circulation models: A TOGA COARE case study. *Quart. J. Roy. Meteor. Soc.*, **123**, 805-827.

Moskowitz, B. M., and C. S. Bretherton, 2000: An analysis of frictional feedback on a moist equatorial Kelvin mode. *J. Atmos. Sci.*, **57**, 2188-2206.

Nakazawa, T., 1988: Tropical super clusters within intraseasonal variations over the western Pacific. *J. Meteor. Soc. Japan*, **66**, 823-839.

Nesbitt, S. W., E. J. Zipser, and D. J. Cecil, 2000: A census of precipitation features in the tropics using TRMM: Radar, ice scattering, and lightning observations. *J. Climate*, **13**, 4087-4106.

Orlanski, I., 1975: A rational subdivision of scales for atmospheric processes. *Bull. Amer. Meteor. Soc.*, **56**, 527-530.

Potter, B. E., 1991: Improvements to a commonly used cloud microphysical bulk parameterization. *J. Appl. Meteor.*, **30**, 1040-1042.

Redelsperger, J.-L., and J.-P. Lafore, 1988: A three-dimensional simulation of a tropical squall line: Convective organization and thermodynamic vertical transport. *J. Atmos. Sci.*, **45**, 1334-1356.

Rotunno, R., J. B. Klemp, and M. L. Weisman, 1988: A theory for strong, long-lived squall lines. *J. Atmos. Sci.*, **45**, 463-485.

Rutledge, S. A., and P. V. Hobbs, 1984: The mesoscale and microscale structure and organization of clouds and precipitation in midlatitude cyclones. XII: A diagnostic modeling study of precipitation development in narrow, cold-frontal rainbands. *J. Atmos. Sci.*, **41**, 2949-2972.

Rutledge, S. A., and R. A. Houze, Jr., 1987: A diagnostic modeling study of the trailing stratiform region of a midlatitude squall line. *J. Atmos. Sci.*, **44**, 2640-2656.

Rutledge, S. A., R. A. Houze, Jr., M. I. Biggerstaff, and T. Matejka, 1988: The Oklahoma-Kansas mesoscale convective system of 10-11 June 1985: precipitation structure and single-Doppler radar analysis. *Mon. Weather Rev.*, **116**, 1409-1430.

Rutledge, S. A., 1986: A diagnostic modeling study of the stratiform region associated with a tropical squall line. *J. Atmos. Sci.*, **43**, 1356-1377.

Schneider, E. K., and R. S. Lindzen, 1976: A discussion of the parameterization of momentum exchange by cumulus convection. *J. Geophys. Res.*, **81**, 3158-3160.

Srivastava, R. C., 1985: A simple model of an evaporatively driven downdraft application to a microburst downdraft. *J. Atmos. Sci.*, **42**, 1004-1023.

Smull, B. F., and R. A. Houze, Jr., 1987: Rear inflow in squall lines with trailing stratiform precipitation. *Mon. Wea. Rev.*, **115**, 2869-2889.

Tao, W.-K., and J. Simpson, 1989: Modeling study of a tropical squall-type convective line. *J. Atmos. Sci.*, **46**, 177-202.

Thorpe, A. J., M. J. Miller, and M. W. Moncrieff, 1982: Two-dimensional convection in non-constant shear: A model of mid-latitude squall lines. *Quart. J. Roy. Meteor. Soc.*, **108**, 739-762.

Trier, S. B., M. A. LeMone, and W. C. Skamarock, 1998: Effect of three-dimensional structure on the stormwide horizontal accelerations and momentum budget of a simulated squall line. *Mon. Wea. Rev.*, **126**, 2580-2598.

Trier, S. B., W. C. Skamarock, M. A. LeMone, D. B. Parsons, and D. P. Jorgensen, 1996: Structure and evolution of the 22 February 1993 TOGA COARE squall line: Numerical simulations. *J. Atmos. Sci.*, **53**, 2861-2886.

Tung, W.-W., and M. Yanai, 2002: Convective momentum transport observed during the TOGA COARE IOP. Part II: Case studies. *J. Atmos. Sci.*, **59**, 2535-2549.

Wang, B., 1988: Dynamics of tropical low-frequency waves: An analysis of the moist Kelvin wave. *J. Atmos. Sci.*, **45**, 2051-2065.

Webster, P. J., 1994: The role of hydrological processes in ocean-atmosphere interactions. *Rev. of Geophys.*, **32**, 427-476.

Webster, P. J., and R. Lucas, 1992: TOGA COARE: The Coupled-Ocean-Atmosphere Response Experiment. *Bull. Amer. Meteor. Soc.*, **73**, 1377-1416.

Weisman, M. L., and J. B. Klemp, 1986: Characteristics of isolated convective storms. *Mesoscale Meteorology and Forecasting*, P. S. Ray, ed., American Meteorological Society, Boston, 793 pp.

Xue, M., K. K. Droegemeier, V. Wong, A. Shapiro, and K. Brewster, 1995: *ARPS Version 4.0 User's Guide*. Center for the Analysis and Prediction of Storms, 280 pp.

Yamasaki, M., 1969: Large-scale disturbances in a conditionally unstable atmosphere in low latitudes. *Pap. Meteor. Geophys.*, **20**, 289-336.

Yang, M.-J., and R. A. Houze, Jr., 1995: Multicell squall-line structure as a manifestation of vertically trapped gravity waves. *Mon. Weather Rev.*, **123**, 641-661.

Yang, M.-J., and R. A. Houze Jr., 1996: Momentum budget of a squall line with trailing stratiform precipitation: Calculations with a high-resolution numerical model. *J. Atmos. Sci.*, **53**, 3629-3652.

Young, G. S., Perugini, S. M., and C. W. Fairall, 1995: Convective wakes in the equatorial Pacific during TOGA. *Mon. Wea. Rev.*, **123**, 110-123.

Zhang, G. J., and X. Wu, 2002: Convective momentum transport and perturbation pressure field from a cloud-resolving model simulation. *J. Atmos. Sci.*, **60**, 1120-1139.

Zipser, E. J., 1969: The role of organized unsaturated convective downdrafts in the structure and rapid decay of an equatorial disturbance. *J. Appl. Meteor.*, **8**, 799-814.

Zipser, E. J., 1977: Mesoscale and convective-scale downdrafts as distinct components of squall-line circulation. *Mon. Weather Rev.*, **105**, 1568-1589.

Zipser, E. J., R. J. Meitin, and M. A. LeMone, 1981: Mesoscale motion fields associated with a slowly moving GATE convective band. *J. Atmos. Sci.*, **38**, 1725-1750.

# Appendix A

## Treatment of Ice-phase Microphysical Processes

This appendix will list the changes made to the standard LFO scheme. If reading this section in earnest, a reference copy of Lin et al. (1983) would be most helpful. The equation numbers listed refer to the Lin et al. (1983) paper.

As discussed in the body of the chapter, the density of snow and hail/graupel are replaced by the density of water, so the slope parameters, equations (5) and (6) in Lin et al. become

$$\lambda_s = \left(\frac{\pi \rho_s n_{os}}{\rho l_s}\right)^{0.25}$$

$$\lambda_g = \left(\frac{\pi \rho_s n_{os}}{\rho l_g}\right)^{0.25}.$$

The expressions for the terminal velocity of snow and graupel as a function of melted drop diameter are different, too. Omitting the density correction term for snow, equation (8) becomes

$$U_{DS} = cD_s^d,$$

and reformulating the hail/graupel term (equation 9) to obey a simple power relationship similar to the rain and snow fields gives

$$U_{DG} = eD_g^f\left(\frac{\rho_0}{\rho}\right)^{1/2}.$$

The mass-weighted mean terminal velocities of snow (equation 12) and hail/graupel (equation 13) become

$$U_S = \frac{c\Gamma(4+d)}{6\lambda_s^d}$$

$$U_G = \frac{e\Gamma(4+f)}{6\lambda_g^f}\left(\frac{\rho_0}{\rho}\right)^{1/2}$$

The following five expressions are hail/graupel source and sink terms which are changed as a consequence of the reformulation of the hail/graupel terminal velocity. These relations presented here replace equations 40, 41, 43, 46, and 47 in Lin et al. (1983):

$$P_{GACW} = \frac{\pi E_{GW} n_{0G} el_{cw} \Gamma(3+f)}{4\lambda_G^{3+f}}\left(\frac{\rho_0}{\rho}\right)^{1/2}$$

$$P_{GACW} = \frac{\pi E_{GI} n_{0G} el_{ci} \Gamma(3+f)}{4\lambda_G^{3+f}}\left(\frac{\rho_0}{\rho}\right)^{1/2}$$

$$P_{GWET} = \frac{2\pi n_{0G}(\rho L_v \psi \Delta r_s - K_a T_c)}{\rho(L_f + C_w T_c)}$$

$$\times\left[0.78\lambda_G^{-2} + 0.31 S_c^{1/3}\Gamma\left(\frac{f+5}{2}\right)e^{1/2}\left(\frac{\rho_0}{\rho}\right)^{1/2}\nu^{-1/2}\lambda_G^{-\frac{f+5}{2}}\right]$$

$$+ (P'_{GACI} + P'_{GACS})\left(1 - \frac{C_i T_c}{L_f + C_W T_C}\right)$$

$$P_{GSUB} = \frac{2\pi(S_i - 1)}{\rho(A'' + B'')}n_{0G}$$

$$\left[0.78\lambda_G^{-2} + 0.31 S_c^{1/3}\Gamma\left(\frac{f+5}{2}\right)e^{1/2}\left(\frac{\rho_0}{\rho}\right)^{1/4}\nu^{-1/2}\lambda_G^{-\frac{f+5}{2}}\right]$$

$$P_{GMLT} = -\frac{2\pi}{\rho L_f}(K_a T_c - L_v \psi \rho \Delta r_s) n_{0G}$$
$$\times \left[ 0.78\lambda_G^{-2} + 0.31 S_c^{1/3} \Gamma\left(\frac{f+5}{2}\right) e^{1/2} \left(\frac{\rho_0}{\rho}\right)^{1/4} \nu^{-1/2} \lambda_G^{-\frac{f+5}{2}} \right]$$

Table A.1 lists the parameters used for the three schemes discussed in the study.

Table A.1: Parameters used by the three ice phase microphysical parameterization schemes discussed in this study.

| Scheme | $N_{os}$ | $N_{og}$ | $\rho_s$ | $\rho_{h/g}$ | a | b | c | d | e | f |
|---|---|---|---|---|---|---|---|---|---|---|
| LFO | 0.03 | 0.0004 | 0.1 | 0.913 | 2115 | 0.8 | 152.93 | 0.25 | 1400 | 0.5 |
| Potter/ Yang | 0.03 | 0.04 | 1.0 | 1.0 | 2115 | 0.8 | 178.8 | 0.42 | 617.2 | 0.54 |

# Appendix B

# Trajectory Calculation Methodology

To diagnose the nature of inflow into the simulated convection, the method of Doty and Perkey (1993) is used to compute trajectories from the ARPS output. The calculation of each trajectory segment is performed in two stages, denoted below by subscripts 1 and 2. The superscript i is the time step number, $\Delta t$ is the trajectory integration timestep that was 6 seconds in this study. Stage 1 of the calculation estimates the new parcel positions:

$$\begin{aligned} x_1^{i+1} &= x^1 + u_1 \Delta t \\ y_1^{i+1} &= y^i + v_1 \Delta t \\ z_1^{i+1} &= z_1^i + w_1 \Delta t \end{aligned} .$$

The initial velocities are defined as

$$\begin{aligned} u_1 &= u_1(x^1, y^1, z^1) \\ v_1 &= v_1(x^1, y^1, z^1) \\ w_1 &= w_1(x^1, y^1, z^1) \end{aligned} .$$

Stage 2 estimates the wind components at the new parcel position calculated above,

$$\begin{aligned} u_2 &= u_2(x_1^{i+1}, y_1^{i+1}, z_1^{i+1}) \\ v_2 &= v_2(x_1^{i+1}, y_1^{i+1}, z_1^{i+1}) \\ w_2 &= w_2(x_1^{i+1}, y_1^{i+1}, z_1^{i+1}) \end{aligned} ,$$

and an average is computed from the old and new velocity component values,

$$\langle u \rangle = \frac{u_1 + u_2}{2}$$

$$\langle v \rangle = \frac{v_1 + v_2}{2} \,.$$

$$\langle w \rangle = \frac{w_1 + w_2}{2}$$

The final position is obtained by using these mean wind components:

$$x_2^{i+1} = x^1 + \langle u \rangle \Delta t$$

$$y_2^{i+1} = y^i + \langle v \rangle \Delta t \,.$$

$$z_2^{i+1} = z_1^i + \langle w \rangle \Delta t$$

Curriculum Vita

David B. Mechem
Cooperative Institute for Mesoscale Meteorological Studies
University of Oklahoma
Norman, Oklahoma 73019
dmechem@ou.edu (405) 325-6103

**Education**

| | |
|---|---|
| 1993 | B. S., summa cum laude, Meteorology with Mathematics minor<br>University of Oklahoma |
| 2003 | Ph. D., Atmospheric Sciences<br>University of Washington |

**Professional Experience**

| | |
|---|---|
| 11/2002 | Guest Lecturer, METR 5233 (Graduate cloud physics), University of Oklahoma |
| 1/2001-present | Research Associate, Cooperative Institute for Mesoscale Meteorological Studies, Norman, Oklahoma |
| 1/1999-12/2000 | Research Associate, Coastal Meteorology Research Program, Norman, Oklahoma |
| 9/1993-12/1998 | Research Assistant, University of Washington, Department of Atmospheric Sciences, Mesoscale Group, Seattle, Washington |
| 9/1994-12/1994 | Teaching Assistant, University of Washington, Department of Atmospheric Sciences, Seattle, Washington |
| 9/1989-8/1993 | Meteorological Aide/Technician, National Severe Storms Laboratory, Norman, Oklahoma |

**Formal Publications**

Mechem, D. B., R. A. Houze, Jr., and S. S. Chen, 2002: Layer inflow into precipitating convection over the western tropical Pacific. *Quart. J. Roy. Meteor. Soc.*, **128**, 1997-2030.

Mechem, D. B., R. A. Houze, Jr., and S. S. Chen, 2003: Momentum transport processes of organized mesoscale convection over the western pacific warm pool. In preparation for *Quart. J. Roy. Meteor. Soc.*

Mechem, D. B., and Y. L. Kogan, 2003: Simulating the transition from drizzling marine stratocumulus to boundary layer cumulus with a mesoscale model. *Mon. Wea. Rev.*, in press.

**Posters, Presentations, and Seminars**

| | |
|---|---|
| 11/1999 | AMS Conference on Coastal Atmospheric and Oceanic Prediction and Processes, New Orleans, LA |
| 4/2000 | FIRE-SHEBA, Boulder, CO |
| 6/2000 | International Conference on Clouds and Precipitation (ICCP), Reno, NV |

| | |
|---|---|
| 12/2000 | Naval Research Laboratory, Monterey, CA |
| 3/2001 | Atmospheric Radiation Measurement Program Science Team Meeting, Atlanta, GA |
| 11/2001 | AMS Conference on Coastal Atmospheric and Oceanic Prediction and Processes, St. Petersburg, FL |
| 3/2002 | DYCOMS-II data meeting, Boulder, CO |
| 4/2002 | Atmospheric Radiation Measurement Program Science Team Meeting, St. Petersburg, FL |
| 6/2002 | AMS Conference on Cloud Physics |
| 9/2002 | Naval Research Laboratory, Monterey, CA |
| 4/2003 | Atmospheric Radiation Measurement Program Science Team Meeting, Broomfield, CO |

**Field Project Participation**

| | |
|---|---|
| 12/1999 | COAST-II |
| 7/2001 | Dynamics and Chemistry of Marine Stratocumulus (DYCOMS-II) |

**Funded Proposals**

"Improvement of the Cloud Physics formulation in the U.S. Navy Coupled Ocean/Atmosphere Mesoscale Prediction System" [Co-PI, 2/2003-2008, Office of Naval Research]

**Professional Societies**

Member, American Meteorological Society